High resolution additive manufacturing using Electrohydrodynamic Jet Printing

Nhlakanipho Colin Mkhize

Wadham College

University of Oxford

A THESIS SUBMITTED FOR THE DEGREE OF

DOCTOR OF PHILOSOPHY

TRINITY TERM 2019

Dedication

In memory of my late grandfather

Sanboyi Simon Mkhize

1 July 1940 – 29 March 2018

"Yamukelani umoya wakhe niwethule koPhezukonke"

Acknowledgements

Ad majórem Dei glóriam

This thesis is the culmination of years of trials and triumphs. It has been a massive learning experience for me, for which I am very grateful. First of all, to thank my supervisor Professor Harish Bhaskaran for allowing me to pursue my work in an independent yet guided manner. This has made me a better researcher. Secondly, to Dr Benjamin Porter, for his guidance, friendship and amazing baking skills. This work would be poorer without you. A big vote of thanks to members of the Advanced Nanoscale Engineering group (past and present) for all the help in whatever form over the years. To my good friends and colleagues, Dr Syed Ghazi Sarwat and Dr Krishnan Murugappan, I owe a world of gratitude.

I would like to acknowledge the Rhodes Trust for their financial support, but not only that, but their constant presence over my studies in giving support to my well-being. Thank you! I thank the Oppenheimer Memorial Trust and the Wadham College Senior Scholarship for financial support in my final year.

Finally, I would like to thank most earnestly my friends and family – who have been a source of great joy and support for me over the past few years. My mom, who has been with me since the start and supported me in ways I never knew I needed; my grandmothers for their prayers, and my aunt for all her love. In a special way, my dear friend and sister, Nomfundo Ramalekana – ngiyabonga.

To the many individuals not named who have made this journey not only possible, but enjoyable, I thank you from the bottom from my heart. Enikwenzele mina nibenzele nabanye.

Abstract

Electrohydrodynamic jet printing (EHD) has emerged in recent years as one of the most competitive high resolution, non-contact additive manufacturing techniques. EHD has been used to achieve fine structures with high aspect ratios in fields ranging from micro and nano-electronics to biomedical engineering and more. However, in order to achieve consistent and reliable printing, it is crucial to have a solid fundamental understanding of the properties of the materials used, as well as the parameters implemented whilst printing. Owing to the hydrodynamic instabilities associated with liquid jets, EHD is particularly sensitive to the properties of the ink used, the substrate being printed on, the environmental conditions and the nozzle configuration. In this thesis, I explore all of the aforementioned parameters in relation to EHD printing and highlight their physical significance and implications.

Having achieved a comprehensive understanding of mechanisms relevant to EHD, I proceed to reduce the principles of EHD to practice by then building a printing system and characterizing its operation through various patterning and feature characterization experiments. Once satisfied that the system was operational, I proceed to answer three broad yet fundamental questions. Is it possible to achieve superior speed and resolution printing of functional inks? How does the electric field generated during EHD printing interact with agents used to control the wetting of surfaces on which printing is being done? Can EHD printing result in the improved performance of existing technologies, specifically looking at gas sensors?

In the process of addressing the above, I demonstrate the ability to print a high resolution molecular template of up to 300 nm in width for subsequent nanoparticle assembly which could enable the design of nanoparticle electronics. The printing of such templates overcomes the disadvantages associated with contact printing, including the inflexibility of the design process and subsequent layer damage.

I provide evidence of the deformational character of electric fields on the self-assembled monolayers used to modify surfaces. The integrity of the monolayers is crucial in the pursuit of high resolution EHD printing, but the influence of the electric field inherent with the process has not been characterized before. I use Kelvin Probe Microscopy to determine the work function imparted by self-assembled monolayers, both before and after an electric field is applied over the coated surface. Static contact angle measurements are used to measure the macroscopic effect of the field on the monolayers. Using computational modelling, the influence of the field is probed more finely. I find that the field does deform the conformation of the monolayers, and this degree of deformation is dependent on the magnitude of the monolayer molecule's dipole moment. Further, I demonstrate how the resolution of printing can be controlled on flexible substrates with a facile physical method. By inducing the formation of wrinkles on an elastomer via the deposition of a stiff thin film, anisotropic patterns are formed. The wavelength and amplitude of these wrinkles are governed by the thin film thickness. I find that coupling fast printing with wrinkles of high amplitude results in good resolution printing, compared to thinner films, or bare elastomer surfaces.

Finally, I demonstrate how the discrete printing of chemiresistors using EHD can lead to the enhancement of ammonia sensing compared to dropcast thin film sensors. I show a more efficient sensing geometry on a substrate with interdigitated electrodes using doped polyaniline as the active material. By optimizing the dopant acid for the polyaniline sensing material, sensitivity of up to 200 ppb is demonstrated, far below the safe exposure limit of 25 ppm. Further, I demonstrate the printing of the polyaniline based sensor onto flexible substrates, demonstrating the versatility of EHD printing.

Table of Contents

Table of Figures

List of Tables

Chapter 1

Additive manufacturing: prototyping for the future

1.1. Microfabrication and the advent of additive manufacturing

Following the invention of the silicon transistor in 1959, silicon based device manufacture led to the development of better subtractive lithographical techniques. While these made the task of fabrication easier, more efficient and more easily miniaturized, they were also very wasteful of starting material.[1–3] Techniques such as electron beam lithography (EBL) enabled much higher resolutions to be reached, and therefore a higher density of components on chips. The now outdated Moore's Law described, infamously, that the number of transistors on a computer chip doubles every 18 - 24 months, in order to keep up with the processing and data demands. As the capacity (and drive) to create smaller structures below a micron (10^{-6} m) in size grew, so did the cost. For instance, EBL (a cleanroom laboratory based process) is prohibitively expensive[1] to develop into an accessible commercial process, especially for small companies. Whilst it has outstanding nanoscale resolution, it is unable to compete with the more affordable photolithography. Photolithography is more affordable owing to a less complex operation mechanism, and has greater reproducibility and commercial success as exemplified by the fabrication of integrated circuits.[4] In the earlier years it faced challenges in achieving resolutions comparable to EBL owing to the diffraction limit for visible light.[5] Extensive work into developing extreme ultra-violet (EUV) lithography has been done in order to address this short-coming, and now features as small as 38 nm have been produced, using 193 nm wavelength light.[6] Using the EBL process as an example, **Figure 1.1** demonstrates the complexity of the fabrication process flow. Following the exposure of the resist to the electron beam, the desired (usually) metal layer is deposited. During lift-off in a solvent, the extraneous material is removed. This process is repeated numerous times until the desired structures are fully formed.

[1] The typical cost of a new electron beam lithography tool is in excess of $2 million.[337]

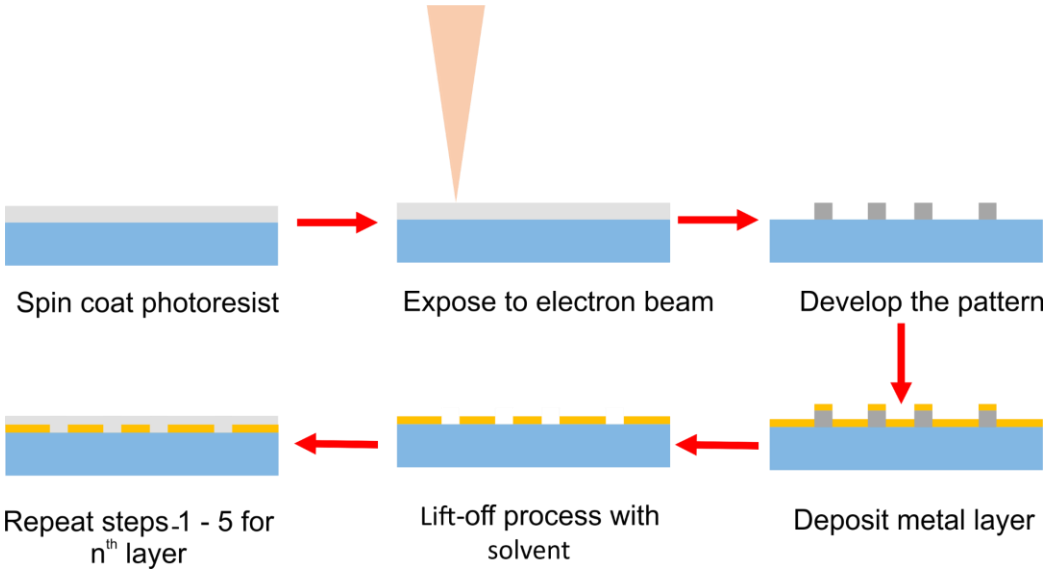

Figure 1.1. Schematic of electron beam lithography process. The process can increase in complexity and time depending on the final structure desired. Problems with the alignment of the electron beam, or with different writing steps can lead to significant delays in obtaining the desired product.

In a manufacturing process, the desired outcome is a product which is obtained quickly, economically and reproducibly every time. One such way to achieve this is to utilize additive manufacturing. Additive manufacturing (AM) refers to a group of bottom-up manufacturing techniques, which build up structures layer by layer rather than creating them from pre-existing bulk in a top-down approach.[7,8] AM has a host of advantages over traditional lithography, the most prominent of which are reduction in cost and material wastage, along with design flexibility (not restricted to limiting geometries).[9] The first instances of AM came in the form of stereolithography (SL) in 1987.[8] This rapid prototyping technique provided a means to quickly create devices for testing before more time was spent creating the final product. It is a commercialized process where a photosensitive liquid polymer is cured by a light source of sufficient energy to induce a photoreaction. The resultant product is a cross-linked polymer composite. The drawbacks of SL include its inability to achieve super fine structures (again due to the diffraction limit), as well as its incompatibility with many non-polymer materials. Over time, and as the need for more intricate or miniature designs grew, more rapid prototyping techniques emerged, making use of available technologies, including digital light processing (DLP), which stemmed from SL.[10] The advantages afforded included faster

printing times and finer structural printing (of up to 20 – 25 μm),[11] as well as greater material choice and the reduced volume of resin needed to form structures.[12] The most notable area where this technique has been used is in the development of biomaterials.[13] Engstrom *et al.* emphasize the point that AM does not (or at least should not) seek to replace existing resist-based manufacturing methods of integrated circuits, but rather add the functionalities that these techniques cannot.[4] Various reviews have successfully communicated the variety of additive manufacturing techniques in existence, as well as their shortcomings and future prospects.[4,6,8,9,14,15]

1.2. Current additive manufacturing techniques

Numerous AM techniques have been developed. The majority of these are used for large scale manufacturing, in industries ranging from aerospace to construction.[16] However, there also exist techniques which are used primarily on the micro and nanoscale. AM techniques can be assessed in two broad categories; extrusion (or direct writing/non-contact) and non-extrusion (contact) techniques.[17] The main difference, as the category names suggest, is that in extrusion, material is deposited from a certain distance away from the substrate, whereas in non-extrusion deposition, the layers are added by a contact process. Direct writing processes afford greater design flexibility as they do not require any physical masks or stamps. This makes direct writing a highly competitive and favourable method. Contact deposition processes offer higher structural fidelity (smoother features) owing to the exactness of the deposition geometry. The advantage that extrusion techniques have over their contact counterparts really, is the range of materials which can be deposited. It is for this reason that this thesis will examine a direct writing technique. **Table 1.1** is a summary of some of the advantages and disadvantages of the most commonly used AM techniques.

Table 1.1. Additive Manufacturing Techniques. A comparison of the advantages and disadvantages of some commonly used additive manufacturing processes on the microscale and nanoscale.

Technique	Advantages	Disadvantages	References
Inkjet printing	• Non-contact patterning technique thus safe to use for multi-layer processes • Variety of materials processable • Does not require vacuum • Requires no mask or template • High speed • Useful for micro and macroscale printing • Widely commercialized • Highly reproducible • Compatible with roll-to-roll processes	• Resolution limited by nozzle diameter • Unable to process materials with high viscosity • Prone to nozzle clogging • Mainly used for planar patterning • Poor drying leads to inhomogeneous films via the "coffee ring effect"	[18]
Spin coating	• Produces homogenous thin films • Applicable with wide variety of materials	• Slow process owing to only one substrate being prepared at a time • Material wastage • Large area coverage not possible • Challenging on highly flexible substrates • Requires prior or subsequent patterning to achieve final design	[19]
Microcontact printing	• Very high resolution • Rapid fabrication process • Does not require vacuum or high temperatures	• Contact mode patterning • Requires fabrication of template stamp using elastomer.	[15,20–23]

	• Allows for many materials to be patterned • Wide applicability • Compatible with flexible substrates	• Limited to planar 2D structures • New stamps required for different patterns	
Screen printing	• Used in mass production • Rapid process • Compatible with many substrates • Sub-micron resolution possible • Cost-effective	• Requires a template mask • Prone to material waste • Contact mode (thus can lead to damage of prior layers) • Heavily dependent on surface wetting behaviour	[15]
Shadow mask lithography	• Multi-layer fabrication is possible • High throughput • No solvents required • Compatible with rigid and polymer substrates	• Requires vacuum conditions • Requires mask fabrication • Resolution limited by mechanical stability of mask • Alignment is challenging • High material wastage	[24]
Dip-pen lithography	• Exceptional nanoscale resolution (15 nm) • Scalable with multi-tip arrays • No substrate modification required to achieve high resolution • Able to deposit sensitive biological matter • Does not require vacuum conditions • Unlimited pattern design	• Large printing tip arrays require complex fabrication • Mechanically fragile tips • Expensive equipment required • Limited material patterning	[4,25–28]
Evaporative printing (aerosol jet)	• No solvent required, therefore ideal for multi-layer patterning • Able to form high quality crystalline films • Able to deposit metal layers	• Sometimes requires vacuum conditions • Can require extremely high temperatures (for metals) • Fabrication of print heads is complex	[29–32]

	• Not prone to clogging due to gaseous nature of jet • No masks required • Versatile patterning possible	• Hot carrier gas management required • Difficult to maintain uniform deposition rate	
Fused deposition modelling	• Allows creation of intricate 3D structures • Low cost • Versatile range of structures • Safe to use in non-laboratory environments	• Only used with thermoplastic material • Many variables need to be controlled for optimal performance • Comparatively poor surface quality • Variable accuracy	[8,33–35]
Gravure Printing	• High throughput • High speed (1 $m.s^{-1}$) • Wide range of ink viscosity processable (10 – 200 cP) • Sub-10 µm resolution	• Suitable only for planar printing • Rigid substrates difficult to process • High initial setup cost	[17,36]
Electrohydrodynamic jet printing	• Resolution not limited by nozzle diameter • Scalable (nano to microscale printing) • 3D structures are able to be created • Wide variety of materials can be processed • Rigid and flexible substrate compliant • Low setup cost • Highly tunable process • Process hybridization possible • Multiple tips can be used in tandem	• Prone to nozzle clogging • Glass tips are easily broken • Only solutions/suspensions processable • Challenging to print on insulating substrates • Substrate damage possible if excess potential applied • Printing varies strongly with varying field strength • Crosstalk probable in multi-tip arrangements	[14,37–40]

The most widely used extrusion process is inkjet printing. Inkjet printing is a technique of ink deposition which makes use of a nozzle or an array of nozzles through which the desired material is passed by piezo actuation.[41] It is a multi-versatile technology which is renowned for its speed and ability to print across large areas. It has been used to print many different functional materials including biomaterials, polymer composites, nanoparticle dispersions, solution processable conductors, and liquid crystals amongst others.[42–48] The major constraint facing inkjet printing for nanotechnology is the printing resolution limit. It has been difficult to obtain printed features less than 5 μm. There are several limitations to this process. Since printing relies on piezo actuation, the jet formed during printing can never be smaller than the nozzle diameter.[49] The printed features will be at least 1.5 times bigger than nozzle.[50] Further pressure build-up can cause issues in the process, resulting in clogging or inconsistent printing quality. Several methods of overcoming these constraints have been employed to achieve commendable results. One such study by Burns *et al.* demonstrated a novel process for the manufacture of highly reliable thin-film transistors (TFT), with On/Off ratios of 10^3.[47] They modified the surface energy of the substrates using a hydrophobic self-assembled monolayer, onto which they printed PEDOT:PSS to fabricate source and drain electrodes of the TFTs. The monolayer split the printed droplet, thus forming the high resolution channel. With this treatment, they were able to produce TFTs with channel length of between 5 and 10 μm.

Another challenge arises in the drying of the printed ink on the surface. Termed the “coffee ring effect”, the migration of solutes to the droplet edges contributes to poor resolution.[51] This results in non-uniform films of material, which can be detrimental to the desired function of the printed structure. Methods to counteract this phenomenon have been explored, the simplest of which is printing on cooled substrates to slow down the Marangoni flow induced migration of solutes. Soltman and Subramanian performed this experiment by printing on substrates which were held four different temperatures, respectively. They found that the evaporation of the droplet at the edges was slower than in the centre for the cooler substrates, but this was

inverted at higher temperatures.[52] An alternative method was used by Fukuda *et al*. They increased the humidity of the environment around the substrate and this resulted in a reduction of the effect primarily due to slowing down the evaporation of solvent.[53] They showed that at very high humidity (90%), a convex drying pattern ensued, whereas at 35% (the lowest humidity tested), a concave pattern was obtained. Other ways include using very high viscosity solvents, or high boiling point systems. These, however, introduce the problem of prolonged drying times. A combination of humidity and substrate temperature control seem to be best method to ensure homogenous material deposition.

Inkjet, therefore, is at an impasse in terms of achieving high resolution. Electrohydrodynamic (EHD) jet printing is able to address this concern. EHD jet printing is a rapid prototyping methodology which has seen significant growth in recent years.[10,54–57] It is a derivative of electrohydrodynamic atomization, and is closely related to electrospraying and electrospinning. The major difference between each of these techniques is the viscosity of the ink used.[58,59] EHD printing has garnered much attention in the fabrication of micro and nanoscale active devices or passive patterns. It has demonstrated great promise in the development of micro and nanoscale architectures for use in electronics, sensory, photonic, biotechnological, biomedical, and display applications, amongst others.[14,15,60,61] The majority of work (in the micro and nanoscale regime) has shown applications in two dimensions,[62] with only a few papers reporting three dimensional printed structures.[10,39,63] The basic operation of the technique involves the printing of an ink onto a substrate from a small capillary nozzle by the application of an electric bias. This electrification of liquid surfaces to induce instabilities has been demonstrated in various experiments for over 100 years.[64,65] The resulting electric field induces an electrostatic force on the surface of the ink which then deforms the meniscus into a droplet. Once the sheer stress overcomes the surface tension, the droplet then stretches into a Taylor cone.[66] This external electric field can be tuned to obtain different modes of EHD printing such as described by Jaworek *et al.*[55] The mode of printing known as cone jet printing is the most desirable mode for the printing of high resolution structures as it ensures

constant, controlled direct writing of the ink onto a substrate. The printing resolution is controlled by a series of five procedures [67–70];

i) adjusting the distance between the printing nozzle and substrate,

ii) altering the speed of the printing,

iii) manipulating the electric field (shape or strength),

iv) changing the composition of the ink used, and

v) altering the surface chemistry of the substrate being printed on.

EHD has many advantages over conventional inkjet printing, but none greater than an enhanced printing resolution. Whilst inkjet printing has resolution limited by the capillary size, this limitation is overcome in EHD due to the electrostatic force used to overcome any adhesive forces the ink may have with the capillary. Moreover, the modification of capillaries with surface monolayers to enhance hydrophobicity on the tips, or the use of tip-enhancing needles can contribute greatly to the finer resolution of the EHD process.[71,72] Significant work has been accomplished by various groups in achieving high resolutions. Galliker *et al.* first reported the growth of nano antenna structures of about 50 nm resolution. This was further developed by Schneider *et al.* using the electrostatic autofocussing nanodroplet printing method to create highly ordered printed metal grids for application as touch sensors.[39,63] Jang *et al.* reported a similar concept using silver nanoparticles, but on a much larger scale (~10 μm).[73] What can be seen from these results is that nanotechnology is intrinsically important to the successful development of nanoscale manufacture.

One of the biggest issues that limits the attainment of high resolution in EHD printing is the clogging of fine capillaries either due to particle agglomeration at the tip, excessive viscosity or solvent capillary forces. This is generally not the case for large capillaries, although clogging can occur here too, but rather for the smaller dimension nozzles. In the pursuit of better resolution, it is crucial to be able to use tips as small as 100 nm in diameter.[14] This may warrant investigating different materials for the tips, as most tips are currently made using

glass. This makes them difficult to handle, almost impossible to reuse and very tricky to process. Being able to manipulate a wide variety of parameters in EHD printing truly makes it a superior technique to other fabrication methods. With a single system, there is potential to print biomolecules, polymers, ceramics, magnetic nanoparticles, 2D materials, human cells et cetera on any desired substrate. That said, there still exists gaps in the understanding of the process. **Table 1.2** lists some of the functional materials which have been printed using EHD printing. By definition, functional materials are those which, due to their native properties, are sensitive to external conditions.[74] These conditions include temperature, magnetic field, electric field, electromagnetic radiation, pH, gas molecules etc. For this reason, Table 1.2 highlights those materials which have been printed with EHD for functions other than purely conducting electricity or for understanding printing parameters. I have thus excluded all printed silver nanoparticles, silver pastes, copper nanoparticles and reactive inks. I have focused on organic molecules, polymers, and semiconducting materials. Further, this work focuses on micro/nanoscale printing.

Table 1.2. Printed functional materials and their resolution. This non-exhaustive table lists some of the functional materials which have been printed using electrohydrodynamic jet printing. The functionalities are wide-reaching and varied. The range of resolutions reported demonstrate the versatility of EHD printing in printing for different applications.

Material	**Functionality**	**Highest reported resolution**	**Reference**
MWCNT/PSS nano-composite in H_2O	OFET	89 µm	[75]
MWCNT/PSS nano-composite in H_2O	OFET		
Poly(3-hexylthiophene)	OFET	47 µm	[68]
Wax	3D microstructures	< 10 µm	[76]
Polycaprolactone	Tissue scaffold	< 10 µm	[77]

DNA ink	Diagnostics	580 μm	[78]
Protein inks	Cell attachment	5 μm	[79]
Colloidal gold ink	Transparent conducting electrode	80 nm	[39]
Quantum dot ink	QD LEDs	~ 3.9 μm	[80]
UV curable polymer NOA 74	Micro lenses	10 μm	[81]
UV curable polymer NOA 164	Optical waveguide multiplexer	7 μm	
UV curable polymer NOA 1375	Diffraction grating	25 μm	
3-(aminopropyl)triethoxysilane in triethylene glycol monomethyl ether	Electrostatic Assembly of gold nanoparticles	~ 300 nm	This work
Graphene ink	Metal ion sensor	~ 80 μm	[82]
PEDOT:PSS blends	Pressure and strain sensor	243 μm	[83]
Polyurethane	Lithography resist	240 ± 50 nm	[38]
Single crystal Si rods	Fluorophores	3 nm	[38]
Ferritin	Catalytic seeds for SWCNT growth	n/a	[38]
Polyaniline	Ammonia sensing	~ 200 μm	This work
DNA	Adenosine biosensor	< 100 nm	[71]
Tungsten disulphide	Bipolar memory	30 μm	[84]
Electro-adhesive gel	Electrically controllable adhesion	200 μm	[85]
Poly(ethylene glycol) micro particles	Drug delivery	n/a	[86]

PZT nanostructures	Piezoelectric	40 nm	[87]
Colloidal crystals	Structural colour	10.2 μm	[88]
Glucose oxidase	Glucose sensor	~ 5 μm	[89]

1.3. Opportunities in additive manufacturing

I have explored a few of the additive manufacturing techniques currently available. The techniques all come with their own advantages and drawbacks, but in all cases, they successfully manufacture devices which are comparable to those made using traditional subtractive methods. As AM continues to complement current manufacturing technologies by adding more functionality to devices, it is important to consider how much impact AM will have on the further development of flexible electronics – a current hot topic owing to the push for wearable functional devices. Further, with the Internet of Things becoming an ever present reality, AM has a big role to play in the production of smart materials and devices which will enable the full realization of the fourth industrial revolution.[90]

1.3.1. Flexible technologies

Traditional lithography techniques are confined to manufacturing on flat, rigid substrates such as silicon. Attempts to utilize them on flexible substrates (mainly polymer) have been unsuccessful in many cases.[91] Additive manufacturing techniques, such as those mentioned, provide a solution for this critical area of development. The fundamental aim of flexible technologies is to broaden the scope and application of electronic devices into traditionally inaccessible fields, such as wearable electronics.[92]

As the need for flexible electronics increases due to advances in health diagnostics, telecommunications and display technologies, better materials and means of patterning them

are required to make flexible electronics commercially viable. As previously stated, conventional forms of manufacturing have limited the types of substrates which can be used to flat and rigid ones. Also, the most common transparent conductive material used has been indium tin oxide (ITO), which has poor mechanical properties on non-planar media. In a recent study, Califórnia *et al.* tested the durability of silver microelectrodes printed in an array on PET via screen printing.[93] The line widths they obtained were quite large (hundreds of microns). They further printed an array of PEDOT:PSS on top of the electrodes to act as an electrochromic layer and as possible protective layer to prevent electrochemical degradation to the silver lines. After optical and electric characterization, the group found that they could obtain electrochromic switching of the PEDOT:PSS in as short as 4.5 s using a 1.5 V sweep through positive to negative, with one hundred cycles before degradation occurred. This technology is therefore most suited to disposable electronics. In all, they showcased a cheap and easy manner to develop an electrochromic device.

Ahn *et al.* contest the use of screen printing to create structures, as this limits the directionality which can be afforded.[7] In their work, they showcase printing via air-assisted inkjet printing. They synthesized their own highly loaded silver nanoparticle ink which was then used to print lines of up to 2 μm resolution on a silicon wafer. To test the flexibility of their microelectrodes, they printed onto polyimide substrate which they then wrapped around a cylindrical object (**Figure 1.2**). Electrical testing, as a function of bending radius showed a remarkable robustness of the electrodes (750 bend cycles). Not only do electrodes have to withstand bending, but also stretching of substrates. The group also demonstrated the ability to create out-of-plane silver arches over a prestrained spring. Upon spring relaxation (and post annealing), the electrodes then form arches as they are constrained – but still maintain their integrity and performance.

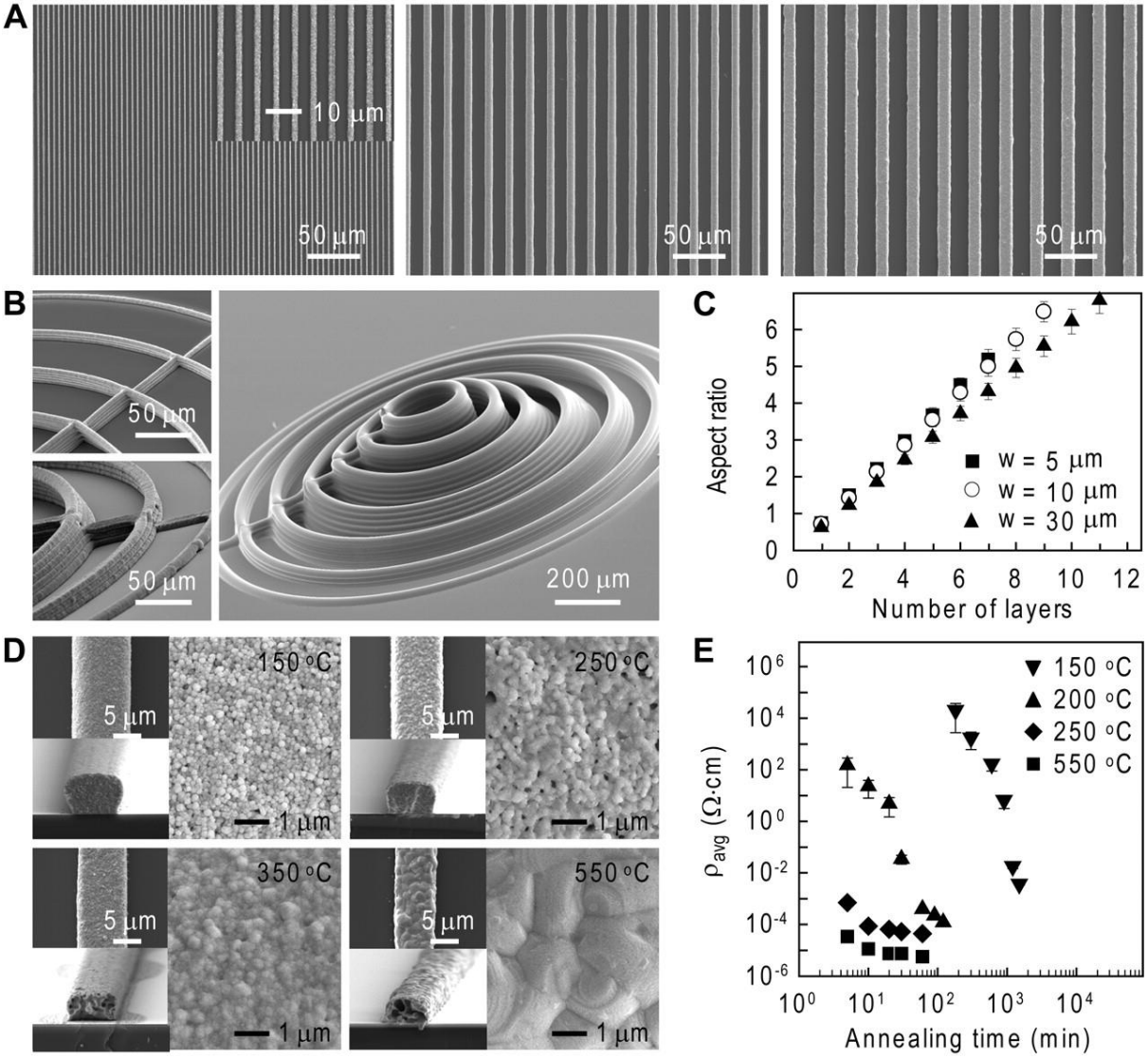

Figure 1.2.(A) SEM images of planar arrays of silver microelectrodes patterned with 1- (left), 5- (centre), and 10-mm (right) nozzles. (B) SEM images of multilayer silver microelectrodes patterned with 5- (top left), 10- (bottom left), and 30-mm (right) nozzles. (C) Aspect ratio as a function of number of printed layers for the silver microelectrodes shown in A. (D) SEM images of silver microelectrodes patterned with a 15-mm nozzle as a function of annealing temperature. (E) Electrical resistivity of silver microelectrodes as a function of annealing temperature and time. Error bars indicate the SD measured from three electrodes. From Ahn, B. Y. et al (2009). Reprinted with permission from AAAS.

Rogers *et al.* highlight two methodologies which have been used to achieve flexible devices: either creating stretchable structures or utilizing stretchable materials.[94] Examples include printing thin films in wavy forms on elastomeric substrates, which when stretched,

elongate without any strain. An example of a stretchable material is a mixture known as Bucky gel. It is a substance made by grinding single walled carbon nanotubes in an ionic liquid and mixing this with a fluorinated copolymer. After printing on PDMS, this material exhibits remarkable ability to retain its high conductive network even under strain. Additive manufacturing, and especially EHD printing can be used to produce such devices.

The integration of different elements to create flexible technologies is made more challenging by the individual physical characteristics of each. As a manner of appreciating the challenges, Rogers *et al*. compare the modulus, thermal coefficient and conductivity of silicon and a typical elastomer; each of the values differing by orders of magnitude. Coupled with this, it is important to consider issues such as the physics of heat transport, and the interactions which occur at interfaces in order to assess the mechanical reliability of the heterogeneous devices. Thus, manufacturing methods need to address the issue of materials compliance.

As more and more manufacturing is done on flexible substrates, new challenges arise. Sugimoto *et al.* offer an example of how changing to flexible substrates may impose new challenges not encountered on rigid surfaces.[92] In the development of OLEDs, the organic material, once deposited, must be encapsulated in order to prevent moisture and oxygen contamination which would reduce the performance of the device. On rigid surfaces, this usually involves a metal or a glass (ITO, aluminium etc) which are impermeable. However, once deposition of the materials is on plastics, there is a risk of contamination due to the permeability of the plastic substrates. Therefore, new passivation layers need to be introduced which fulfil the criteria of high levels of impermeability, optical transparency, have low temperatures of deposition (as OLEDs are temperature sensitive) and lastly, lack high film stress as this could cause the organic layers to peel off, thus destroying the device. Additive manufacturing has the ability to address these concerns.

Electrohydrodynamic jet printing, then, is an ideal candidate to segue from traditional manufacturing methods into this dynamic world of flexible technology. It addresses the major

concerns for fabrication on flexible substrates, and allows for ever more creative applications to be achieved. It allows the rapid manufacturing of devices at a fraction of the cost of lithographic techniques. The technique is highly accessible and simple to utilize. Having compared EHD to a host of other AM methods, it has the greatest potential to create not only high resolution structures, but to impart functionality which is not possible with other techniques. In the next chapter, I will highlight the operational parameters of EHD which affect these two motivations.

1.4. Final remarks

I have shown that additive nanomanufacturing offers many exciting and important possibilities in a variety of fields. Having highlighted the techniques in use, as well as their challenges and opportunities, I have demonstrated the massive potential for additive manufacturing; especially that of EHD jet printing. This technique will be the focus of my thesis. In addressing reproducibility, throughput and the functionality of materials, EHD possesses the greatest means to achieve current manufacturing goals[2] by utilizing a variety of different materials. The challenges that have been faced before are not impossible. Substrate surface enhancement via chemical means is an area where much work still needs to be done. A significant portion of the work I do will be based on optimizing this. Hybridization of various techniques is easily achieved with ANM; this is one of its greatest strengths, and I will exploit it to form novel structures. With a move towards flexible electronics and 3D ANM, it is anticipated that more work will being done with EHD, and I aim to contribute significantly to its development.

[2] Goals including a fully integrated Internet of Things, artificial intelligence, wearable electronics, and environmentally sustainable production.

1.5. Thesis Goals

The aim of this thesis is to further the understanding and development of high resolution electrohydrodynamic jet printing. After placing this technique in context of other additive manufacturing methods in the first chapter, the rest of the thesis seeks to:

- Highlight the benefits of electrohydrodynamic printing, after providing a clear theoretical background. (Chapter 2)
- Explain how an EHD setup is put together, and how initial calibration experiments are useful in understanding the technique. (Chapter 3)
- Demonstrate high resolution sub-micron printing with a novel ink material. (Chapter 4)
- Provide further understanding into how best to control resolution on surfaces using chemical and physical means. (Chapter 5)
- Demonstrate the use of electrohydrodynamic jet printing in achieving superior functional device manufacturing, specifically looking at a printed gas sensor. (Chapter 6)

The final chapter summarises the conclusions reached and highlights further work that could be pursued.

Chapter 2

Electrohydrodynamic jet printing
Concepts and considerations

2.1. Electrohydrodynamic Jet Printing

Electrohydrodynamic (EHD) jet printing is a non-contact printing technique which has gained much attention in recent years.[14,38,95] It works by applying an electric field to induce ink ejection from a conductive nozzle onto a grounded collector. EHD is a specific application of the well-studied electrohydrodynamic atomization (EHDA).[62] For these methods, the electrostatic force resulting from the normal component of the electric field is sufficient to overcome the surface tension of the ink in **Figure 2.1a**.[96] The full sum of forces is represented. **Figure 2.1b** demonstrates the magnitude of the electric potential around a nozzle.[97]

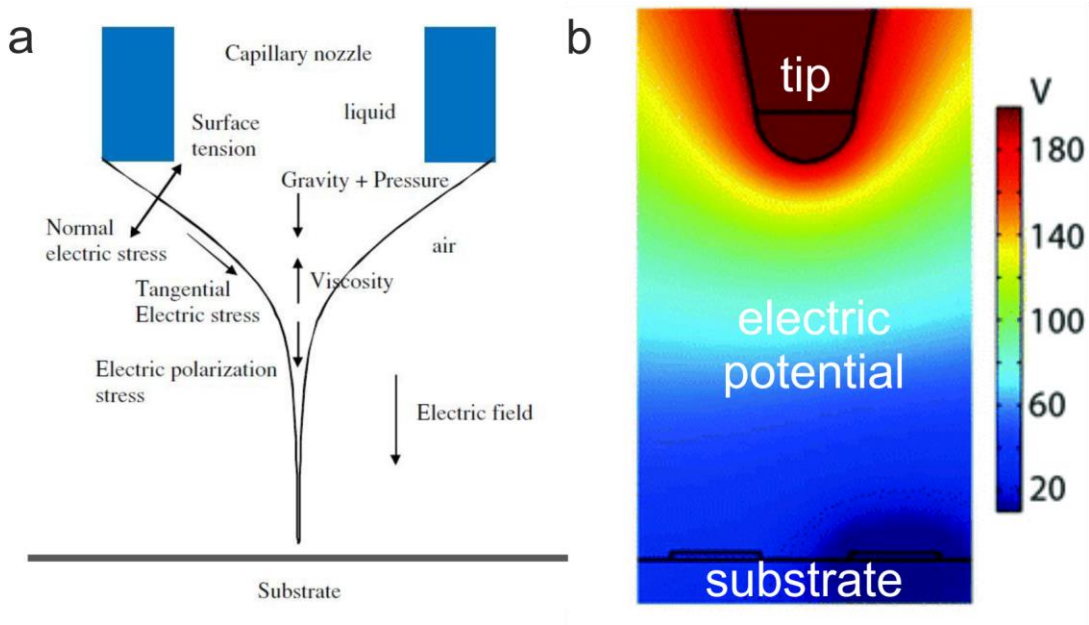

Figure 2.1. Physics of electrohydrodynamic jet printing. (a) Summary of forces acting at capillary tip during EHD printing using the cone-jet mode (Reproduced with permission from [96]). (b) The model shows the spatial distribution of the electric potential during EHD operation around the tip, with the scale bar indicating field strength. (Adapted with permission from [97])

When a liquid is in a capillary, as shown in **Figure 2.1a**, and is unperturbed, it will not flow until a force is applied which will overcome the surface tension by which it is held stationary, as well as the capillary forces. The only forces pushing down on it are a weak gravitational force and any pressure which exists within the system. When an electric potential is applied to the system, charge will migrate to the meniscus surface of the liquid, depending on whether it has mobile charge carriers or not. The conductivity of the liquid depends on the number of charge

carriers per unit volume and their drift velocity.[98] When sufficient charge has built up on the liquid interface, an electrostatic potential will exist between the meniscus and the grounded substrate. The electrical stress now present will have a normal and tangential component, as the inks are generally not perfect conductors.[99] The normal stress destabilizes the meniscus and the tangential component supports the formation of the meniscus into a cone (termed a Taylor cone [100]) which results in printing. This works best for liquids which are sufficiently dielectric, meaning that they can sustain the electric field.[101] [72] In their work, Subbotin and Semenov mathematically describe the stable conditions at which stationary cone-jet streaming occurs.[102] Early work by Hayati *et al.* on the mechanism of stable jet formation in electrohydrodynamic atomization demonstrates visually the effect of the electrical stresses on a fluid by showing the circulation patterns which can arise (**Figure 2.2 a,b**).[103]

The advantage of EHD printing comes from the fact that it relies on the formation of a characteristic Taylor cone (first described by Sir Geoffrey Taylor). The jet will be of smaller spatial dimensions than the nozzle used if the correct conditions are applied, unlike what is observed with conventional inkjet printing.[104] Taylor found that for an ideal conducting liquid, the angle at the cone apex is $2\theta_T = 98.6°$.[102] This size reduction in jet diameter is especially important in pursuits such as nanofabrication, where the size limits of devices and structures are currently restricted with existing extrusion technologies, such as inkjet printing.[14,105] With EHD, high aspect ratio printing of up to 50 nm lateral resolution has been demonstrated (**Figure 2.2c-g**).[63] The versatility of the process is further enhanced by the wide variety of materials which can be deposited, in any configuration, without the need for set templates or masks.[14,106] It is a true additive manufacturing technique as only the material required is deposited, thus eliminating waste.[107] This is one of the reasons why the technique is touted as being one of the most economical manufacturing techniques available.

The mathematics of the stable jet mode is beyond the scope of this work, but can be found in seminal work done by Hohman *et al*.[108] Other jet modes have been reported by Jaworek.[55]

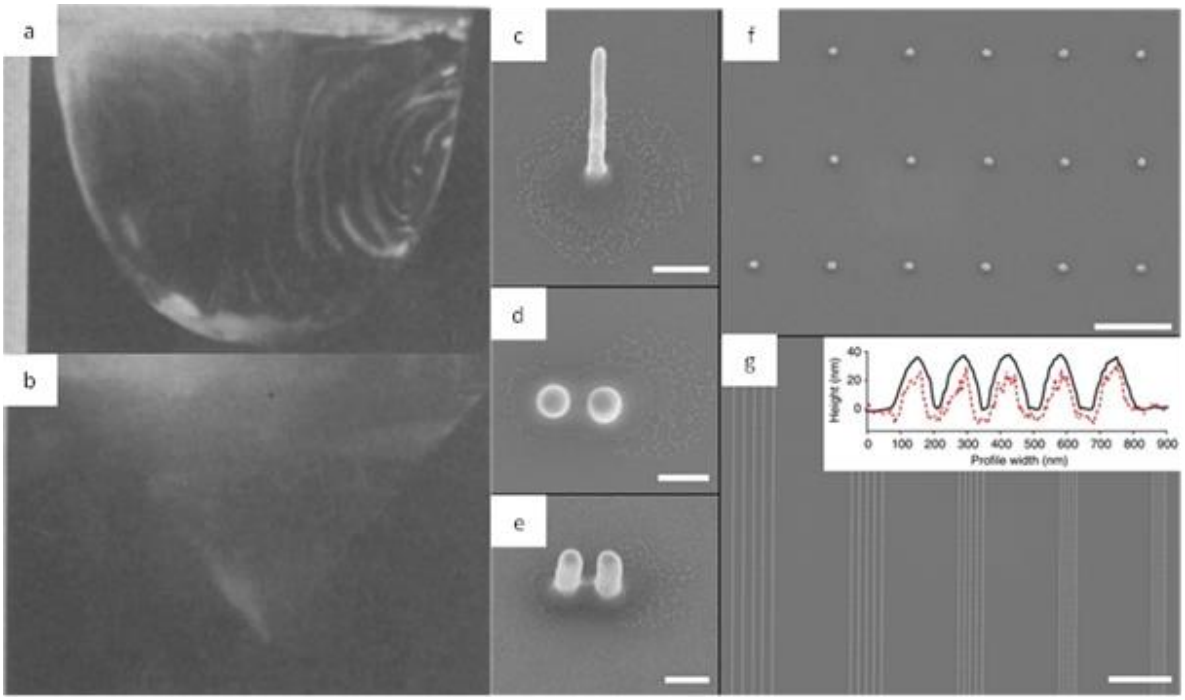

Figure 2.2. Meniscus dynamics and 3D capability. (a) Streak photograph of the circulation pattern within an oil drop suspended at the end of a metal rod in helium gas. (b) Streak photograph of the circulation pattern within the same drop as in (a), but suspended in air, where a jet is formed. Reprinted by permission from Springer Nature Customer Service Centre GmbH, Reference [103] (**c**) Gold nanopillar of diameter ~50 nm and aspect ratio of ~17 (Scale bar, 200 mm). (**d**) Top and (**e**) side view of nanopillars printed subsequently at 200 nm centre-to-centre distance (scale bar, 200 nm). (**f**) 80-nm wide dots printed into a 1-μm lattice constant array (1 μm scale bar). (**g**) Printed tracks with pitch sizes of 250, 200, 150, 100 and 75 nm (scale bar, 2 μm). The inset shows AFM (full black lines) and SEM (red dashed lines) profiles of 150-nm pitch size. The height of AFM profiles is given in nanometres. The SEM profiles are in arbitrary units. Tracks have reproducible heights of ~40 nm and are well separated. Reprinted by permission from Springer Nature Customer Service Centre GmbH, Reference [63].

In order to fully make the best of the benefits of this technology, the interplay between properties of materials used and system parameters must be understood.[76,109] Currently there exists a dearth of work discussing this intersection. The interaction of the electric field with the

chosen ink relies heavily on the system's parameters including applied potential, standoff height, nozzle diameter and operating environment (e.g. humidity, temperature, etc).[110] In addition, there are properties of the ink that require due consideration, namely surface tension, viscosity, conductivity and fluid nature. In the following sections, we look at each of these named variables in turn and relate them to the overall EHD process.[111,112] Several key studies looking at the interplay of only some of these variables have been reported.[112–114] Lee *et al.* and Choi *et al.* have done work in describing the majority of these parameters.[112,115]

The goal of this chapter is to enhance understanding of the EHD process and highlight the intricacies involved in order to achieve the best possible result and resolution, based on existing methodologies, as well as those which I describe here. For applications of EHD printing, several excellent reviews exist within the larger framework of additive manufacturing,[4,14,116] biological studies,[117–119] and electronics.[120]

2.2. Ink considerations

2.2.1. Surface tension

A free droplet, unencumbered by electrostatic, aerodynamic or gravitational forces will always assume a spherical shape. This is due to a sphere costing the least energy to form. This minimization of energy (and areal coverage) is due to the surface tension (γ) of the molecules. This property is a consequence of the fact that molecules at the free surface (liquid-air interface) have higher energy than within the bulk.[121] When we consider the droplet on a solid surface, there exists a force which is a result of the surface tension. This force acts in the plane of the free surface, perpendicular to a free edge in that surface. The force (F) is proportional to the length (L) of the edge.

$$F = \gamma L \qquad \text{(Equation 2.1)}$$

Surface tension is an important parameter to consider for the inks used in EHD printing. The electrical force actuated needs to be able to overcome the surface tensile force with which the

meniscus is held to the capillary.[122] It has been demonstrated by He *et al.* that if the surface tension is too low, the ink will form satellite droplets before a stable jet can be formed, owing to a longer pinch off time (the time it takes for a droplet to detach from the jet).[123] Studies also show that if the surface tension is too high, the electrostatic force applied will not be sufficient to cause the jetting of the material, [124] and only meniscus pulsing will be observed, resulting in no printing. I have noted several articles making reference to a specific range of surface tensions which are considered useful or optimal for EHD printing.[69,112] 'Islands of stability' have been demonstrated, taking into consideration other properties such as conductivity and viscosity, which I shall discuss shortly

In order to understand the influence of the surface tension EHD, let us first look at a very simplified mathematical treatment. A basic condition for jetting to occur is that the electrostatic force be sufficient to overcome the surface tension (**Equation 2.2**);

$$\boldsymbol{F_{\text{surface tension}} = F_{\text{electrostatic}}} \qquad \text{(Equation 2.2)}$$

If we treat the force between the capillary and the ground plane as being capacitive and the surface tensile force as being the product of the surface tension and the distance over which the force is applied, we obtain **Equation 2.3**

$$\boldsymbol{\gamma L = \frac{\varepsilon_0 A V^2}{2d^2}} \qquad \text{(Equation 2.3)}$$

where γ is the surface tension of the ink, in N/m, L is the distance over which surface tension (in m) applies (in this case circumference of the pipette), *A* is the area over which the electric field is experienced, *V* is the applied potential, and *d* is the standoff height. Rearranging for V, we obtain the following (**Equation 2.4**).

$$\boldsymbol{V = \sqrt{\frac{2\gamma L d^2}{\varepsilon_0 A}}} \qquad \text{(Equation 2.4)}$$

From this, we see that $V \propto \gamma^{0.5}$. The applied potential is directly proportional to the square root of the surface tension. Smith plotted this relationship for a series of common solvents and

found a linear trend (**Figure 2.3**).[57] The higher surface tension of some solvents is due to the strong intermolecular forces, such has hydrogen bonds. This relationship is notable, as it means that the applied voltage doesn't increase too rapidly over a range of surface tensions, which a single material could exhibit – especially under variable temperature conditions.

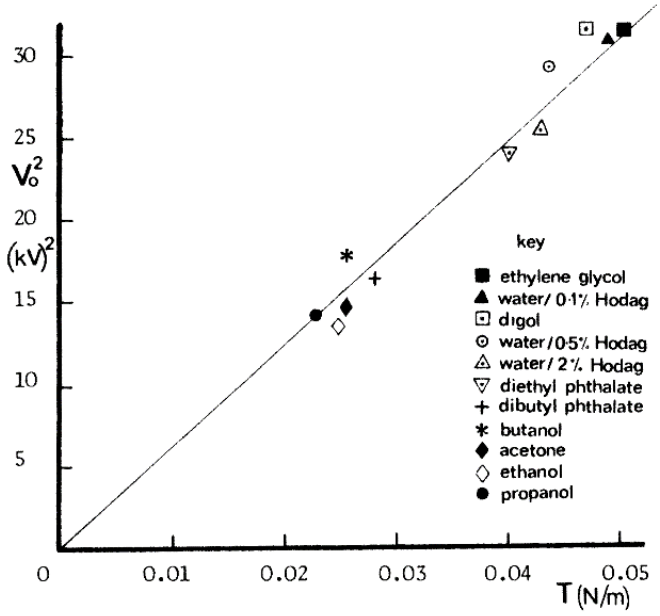

Figure 2.3. Effect of surface tension on applied voltage. © [1986] IEEE. Reprinted, with permission, from [57].

Using two different inks, Choi *et al.* [115] derived more involved scaling laws that enable us to understand better the relationship between the electric field strength and the jet pulsing frequency and diameter as the jet leaves the capillary tip. They performed EHD experiments using several capillary sizes and also compared existing literature. As a starting point, they describe the flow rate of the jet using the Poiseuille-type flow rate equation (**Equation 2.5**) first described by Chen *et al.* [125]

$$Q \approx \frac{\pi d_N^4}{128\mu L}\left(\Delta P + \frac{1}{2}\varepsilon_o E - \frac{4\gamma}{d_N}\right) \qquad \text{(Equation 2.5)}$$

Where Q is the flow rate, d_N is the diameter of the nozzle, μ is the viscosity of the ink, L is the nozzle length, ΔP is the change in pressure, ε_o is the permittivity of free space, E is the electric field strength and γ is the surface tension on the meniscus. Approximating the electric field E

is done by using a model of a semi-infinite wire perpendicular to an infinite planar electrode (**Equation 2.6**)

$$E = 4V_0 / \left[d_N \ln\left(\frac{8H}{d_N}\right)\right] \qquad \text{(Equation 2.6)}$$

Where V_0 is the applied potential difference and H is the distance between the tip and substrate. We shall refer to this distance from now on as the stand-off height. Through a series of derivations, which are not part of the scope of this work, Choi presents two scaling laws which can give the relative magnitudes of important parameters mentioned above. The jet diameter scales according to **Equation 2.7**,

$$d \propto \sqrt{\frac{\gamma}{\varepsilon_0}} \frac{\sqrt{d_N}}{E} \qquad \text{(Equation 2.7)}$$

Which means for an increase in electric field, there is a linear decrease in jetting diameter. The second scaling law describes the relation between the jet pulsing frequency and the E field, and is stated as (Equation 2.8):

$$f \propto \left(\frac{\varepsilon_0^3}{\rho^2 \gamma}\right)^{1/4} \frac{E^{3/2}}{d_N^{3/4}} \qquad \text{(Equation 2.8)}$$

Where ρ is the density of the ink used. Having described these laws, they found satisfactory agreement with the experiments they performed. Understanding these laws, and the deviations which occur from them (for different pressures or very low surface tension systems), is beneficial for the design of EHD systems. We note here that these are not the only scaling laws which have been developed, nor are they a completely rigorous description of EHD printing. They are merely a guideline which has been accepted by many research groups working in the field.

It is also important to note that surface tension is dependent on temperature.[126] Rowlinson and Widom state that the surface tension of a liquid in equilibrium with its own vapour pressure

decreases and becomes zero at the critical point[3] as temperature is increased.[127] Whilst this this highly unlikely to happen in EHD printing due to the tiny volumes used, it is noteworthy. Temperature effects are still non-trivial. The first major cause of temperature change would be the printing environment. It is ideal to keep conditions as constant as possible to ensure reasonable printing quality and reduce any inconsistencies.[128] When an electric field is applied, temperature can be significantly changed (increased) if arcing is allowed to occur, or if the electrical conductivity of the ink is so low that jetting is not possible. This could lead to a point where the surface tension of the material being printed is altered, thus throwing off the balance between the surface and electrostatic force (see **Figure 2.2a**).[129] The likely outcome of this would be a higher order jetting mode or excessive material being printed at any one time. This could be rectified with a feedback system which takes into consideration changes in jetting rate. If the jet flow changes to a value lower than expected, the feedback system could effectively alter the voltage, thus rectifying the issue. In fact, such a system has been demonstrated by Kien *et al.*[130] Alternatively, a cooling system could be used to maintain the stability of the surface tension of the material during printing. A cooling system for instance can be used to control the substrate temperature to limit wetting (as previously mentioned – see Inkjet printing discussion in chapter 1). This method has been employed to limit the 'coffee stain effect' observed in inkjet printing.[52] Short printing times could also mitigate the differential temperature issue.

Surface tension is one of the easiest properties to control in inks used in EHD printing. It has a significant effect on the magnitude of the potential required to induce printing. Surface tension also plays a large role in the consideration of the nozzle dimensions for a particular system. To mitigate any negative effects, it is essential to know what kind of surfactants can assist in controlling the surface tension to a desirable range.

[3] The critical point here refers to the phase diagram for materials between the solid, liquid and gas phase.

2.2.2. Surfactants

In developing functional inks, the addition of surfactants can alter the surface tension considerably.[38,51,124,131] Accurate characterization is crucial of the surface tension for all new ink blends before use, to be able to predict the conditions they will require for effective printing. The addition of surfactants, which disturb the intermolecular forces, can sometimes introduce new challenges to the processing of printed structures. Depending on the volume of surfactant added, the solvent evaporation temperature could be increased when trying to sinter or dry the printed feature. This is especially important where substrates on which the inks have been printed onto are not able to be heated very high (polymers, phase change materials etc.).[132–134] Excessive reduction of the surface tension must also be avoided, else over-delivery of the ink is possible. Li *et al*. demonstrate a secondary serendipitous effect of surfactant in inks. They show that surfactants can boost the electrical properties of multi-wall carbon nanotube inks.[135]

2.2.3. Colloids

When considering colloidal suspensions used as inks, not only is surface tension important, but also the colloid concentration. A study by Dong and Johnson showed how the surface tension of an aqueous suspension decreases significantly as the concentration of titanium oxide increased, until a critical point was reached (**Figure 2.4**). After this point, it is hypothesized that further increasing the concentration increases the surface tension due to inter-particle capillary forces dominating, until a plateau is reached.[136] This being the case, highly concentrated suspensions could lead to nozzle clogging due to particle aggregation, which increases the viscosity of the ink significantly.[137,138] Thus, dilute concentrations of colloidal suspensions tend to be used.[139,140]

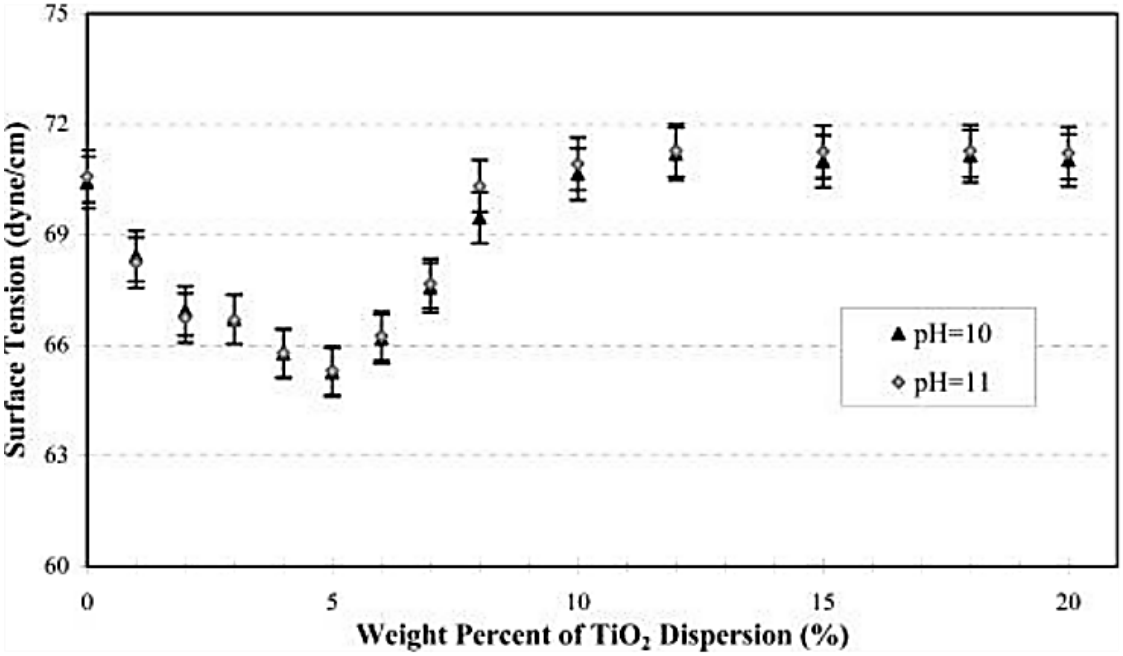

Figure 2.4. Surface tension responding to colloidal concentration. Plot of the surface tension versus weight percent of titania dispersions at pH 10 and pH 11. The plot shows that the surface tension of the dispersion decreases significantly from approximately 0% to 5% and then increases above the surface tension of pure water at 10% and higher weight percentages. Reprinted with permission from [136]. Copyright (2003) American Chemical Society.

2.2.4. Solutions

In an ideal scenario, a completely solubilized ink should be used for printing, to avoid any issues of aggregation-induced clogging. This is why reactive inks (mainly silver) have attracted much attention.[141,142] The precursor is a metal salt completely dissolved in a solvent, with appropriate additives used to control the ink properties. It is printed and then exposed either to UV light or mild heating in order to achieve the desired metallic patterns. It is assumed also that solutions are Newtonian fluids. This means that the flow expected during printing should be linear and proportional to the applied forces. However, in reality, other types of inks exist.

Viscoelastic fluids are mostly comprised of high molecular weight materials such as polymers, and exhibit counter-intuitive behaviour. Due to their macromolecular nature, they

exhibit elastic behaviour at times, but also exhibit viscous behaviour under certain conditions.[143] Newtonian fluids behave more predictably. They respond linearly to the strain exerted on them. In reality, all inks used are viscoelastic to some extent. This makes characterizing them more elaborate. Where once there were known relationships between viscosity, flow rate and the applied potential, viscoelastic liquids demand more complex treatment. For the purpose of this work, non-Newtonian fluids will not be discussed at length. They are dealt with in work done by Feng.[101]

Inks which are emulsions of immiscible liquids or liquids and particles with different properties pose the threat of phase segregation when exposed to non-uniform electric fields (as are observed in EHD printing).[144] Therefore, when using additives to alter solution properties, the quantities of the additives must be such that the possibility of phase segregation (especially for polymer solutions) is minimised. The problem that this separation could result in is the alteration of the desired properties of the printed structures. Where precipitation or aggregation is possible, a separation leads to a clogging of the printer nozzle. There exist numerous studies where melts are used as inks. Han *et al*. demonstrate the patterning of a wax ink to form micro-pillar arrays, and high aspect ratio thin walls. Owing to the rapid phase-change the wax exhibits once printed (liquid to solid), 3D structures are easily obtained. These can be used as scaffolds for further fabrication.[76] To achieve this, the authors had to modify their printer system to incorporate a heating element.[145] The same team also presents the printing of Field's Metal.[105] In order to get the metal to print (despite its extremely high surface tension), the nozzle had to be heated to 380 °F (193 °C) before jetting could occur. It is clear that the more complex the ink system, the more engineering work needs to go into the attainment of the required product.

2.2.5. Conductivity

Where electrostatic actuation is required, the conductivity (K) of the ink used is of critical importance. The intrinsic charge mobility affects parameters such as Taylor cone formation time, charge relaxation time and voltage required to cause flow (all these affected by viscosity

too). Various time constants exist which describe these relationships, and are discussed presently.[146]

A vast amount of work done in the field of EHD printing has been for drop-on-demand type work, however, more interesting is the application of this technique to continuous jet printing. Continuous jet printing is more favourable owing to its scalability and commercial viability. Completely insulating solvents, such as hexane for example, will not allow for conventional jet printing. Zhang *et al*. studied a family of dielectric silicone oils which vary in viscosity but have similar surface tension, conductivity and relative permittivity values.[147] Owing to their poor conductivity, these liquids are unable to exhibit cone jet behaviour, but do demonstrate unstable transient jetting. Other solvents which are more naturally conductive (such as ethanol) are better able to sustain EHD jet printing.[57]

Various studies have been conducted in EHD with solvents which are considered more dielectric ($K \leq 10^{-12}$ $S.m^{-1}$) than conductive.[112] By adding more charge carriers to solvents (by addition of salt solution or acid), one can increase the degree of conductivity, thus making the charge transfer process easier and facilitating EHD printing. The addition of dilute acid or salt solutions to inks has been demonstrated to increase the ionic concentration and thus improve the conductivity.[57,146,148,149] The addition of acid however, can alter the physical nature of the solution, especially where polymers are involved. For instance, gelation/swelling of polyvinyl alcohol (which can be used as a surfactant) has been observed in the presence of hydrochloric acid.[150] The precipitation of species is also a consequence of altering the pH of an ink by adding acid, as is demonstrated by Cao for polyaniline.[151]

2.2.6. Parameters influencing conductivity

Depending on the type of ink used (whether polymer based, salt, colloidal or organic), different charge carriers will exist. The simplest case is that of ionic salts. Here, the anions and cations carry the charge in the presence of the electric field. These typically are the most conductive types of inks, both for salt solutions and ionic liquids.[152] Metal nanoparticle based inks are

also very conductive, owing to the free flow of charge that can be achieved between individual particles. Whilst not as conductive as bulk metal, it is possible to obtain excellent conductivity levels with these inks. Conductive polymer inks behave slightly differently. The mechanism by which charge moves depends on the structure of the polymer chain or the additives introduced to the polymer to induce conductivity. In a book chapter, Dai describes four types of conducting polymers.[153] These four types are: conjugated conducting polymers, charge transfer polymers, ionically conducting polymers, and conductively filled polymers. We describe the first and fourth types briefly, as they are most commonly found in ink systems.

Conjugated conducting polymer inks are the most common (e.g. polythiophene, polyaniline, polyacetylene), and have been the subject of much investigation and optimization. They are intrinsically conductive due to the overlap of π-orbitals, which provides a pathway for charge carriers to move. To improve their conductivity, however, they are usually doped (different methods exist), as they do not have intrinsic charge carriers. Doping them also allows for increased solubility, especially in polar solvents such as dimethyl sulfoxide or water, thus allowing them to be used as inks. An example of this is reported by Cao *et al.* where they systematically dissolve doped polyaniline in various organic solvents and study the conductivity of the films formed from each solution.[151]

Conductively filled polymers comprise of insulating polymer scaffolds which have been filled either with conjugated conducting polymers or other conductive solids. Also, the solvents in which they are dissolved play a great role in ensuring their conductivity. For example, the majority of polymers used in electrospraying are insulating (e.g. polystyrene, poly(methyl methacrylate) etc.). By adding metal nanoparticles, co-dissolving with conducting polymers, or by using polar solvents, jetting can be achieved with these materials too. With this kind of modification, a great range of applications can be achieved.[154]

2.2.7. Relaxation Times

Lee *et al.* describe a set of dimensionless values which they use to optimize the experimental parameters of EHD printing regimes.[112] Looking specifically at conductivity, they define a parameter τ_q/τ_H, which takes into consideration the charge relaxation time (τ_q) and the hydrodynamic relaxation time (τ_H). Hydrodynamic relaxation time refers to the time it takes for the liquid to respond (equilibrate) under new conditions. In this case, how long it takes to respond to the presence of an electric field, and is given by **Equation 2.9**.

$$\boldsymbol{\tau_H = \frac{\eta r}{\gamma}} \qquad \text{(Equation 2.9)}$$

Where η and γ are the viscosity and surface tension of the liquid respectively, and r is the outer radius of the capillary used.[146]

Charge relaxation time is more related to the conductivity and not the viscosity, and is given by **Equation 2.10**

$$\boldsymbol{\tau_q = \frac{\varepsilon_o \varepsilon_r}{K}} \qquad \text{(Equation 2.10)}$$

Where *K* is the electrical conductivity (S/m), ε_r is relative electrical permittivity, ε_o is vacuum permittivity (8.8542 x 10^{12} F/m).[146] It defines the characteristic time of charge transport determined by the electrical properties of the material.[112]

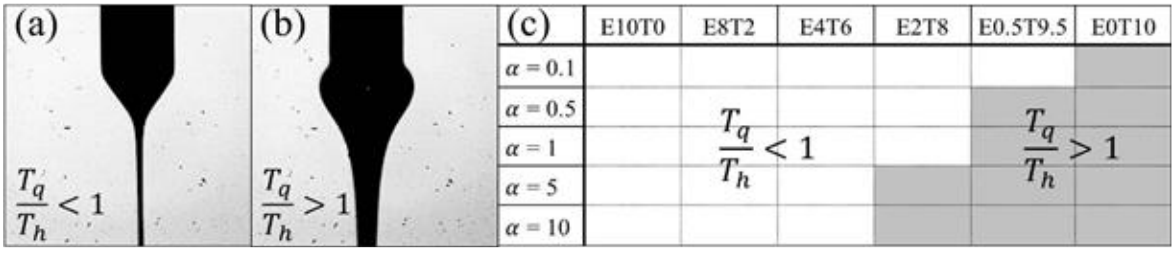

Figure 2.5. Influence of Relaxation times. Representative shape of (a) cone-jet (τq/τh < 1) and (b) ball-cone (τ_q/τ_H > 1). (c) Jetting window with respect to α for each fluid; the white region is for a classical EHD system and the gray region is for a forced jet system (E is ethanol and T is terpineol). Reprinted with permission from [112]. Copyright 2013 American Chemical Society.

If the ratio is less than 1, meaning that the fluid has a sufficient number of charge carriers and high enough electrical mobility and the fluid is flowing slowly as in a quasi-equilibrium state, then jetting can be expected. $\tau_q/\tau_H > 1$ is characteristic of dielectric liquids ($K \sim 1e^{-10}$ S/m) and does not exhibit classical jetting, but rather ball-cone jet (**Figure 2.5b**).[112] This is a mode where the flow of fluid is faster than the charge transport to the normal of the ink-air interface. This results in the electrical stress taking time to become apparent.[147] This is true for highly conductive, non-viscous solutions such as poly(3,4-ethylenedioxythiophene)-poly(styrenesulfonate) (PEDOT:PSS).[155]

In any particular experimental arrangement, there exists a system threshold. Suitable engineering and practical design can help relax these, but it really comes down to a fundamental operational understanding of the process to maximise the output and performance. This is highlighted in work by Hayati *et al.* where they demonstrate that there is an optimum conductivity where a jet is stable for a fixed operating conditions.[156] This stability can be achieved for other values of conductivity, if the system is adjusted accordingly.

Summarising the above, conductivity is dependent on the charge carrier density of the ink. It can be altered by adding ionic material such as acid or salt solutions, without changing the functionality of the ink significantly. Certain solvents can also enhance the conductivity, especially in polymer inks. If the ratio of τ_q/τ_H is favourable, good printing can be expected. If unfavourable, this will lead to difficulty in getting the process to work. A property which links up with the mobility of the conductive species is discussed next: viscosity.

2.2.8. Viscosity

Viscosity (η) is a measure of how resistive a liquid is to flow, due to intermolecular forces within the liquid. By definition, it is the ratio of the shear stress (τ) to the shear strain rate ($\dot{\gamma}$). If the viscosity is independent of the strain rate, the liquid is linear, or Newtonian. If is it dependant, it is non-Newtonian, and requires more complex analysis. In printing systems, the viscosity of

inks is commonly controlled by adjusting printhead temperature. This is due to the dependency of viscosity on temperature.

The Ohnesorge number has been used to relate the viscosity to the surface tension in the following relation (**Equation 2.11**).

$$\boldsymbol{O_h} = \frac{\boldsymbol{\eta}}{\sqrt{\boldsymbol{\rho \gamma L}}} \qquad \text{(Equation 2.11)}$$

where η is the ink's viscosity, ρ the density, γ the surface tension and L the droplet length (usually the drop diameter). A more useful parameter however is *Z*, the reciprocal Ohnesorge number. It has been found that if *Z* lies between 1 and 10, jetting can occur. If *Z* is below 1, viscous forces dominate and no droplets can form. When *Z* is greater than 10, the droplets could break into satellite droplets, thus reducing the printing quality considerably.[157] This parameter, along with the Weber number (*We*) and Reynolds number (*Re*), have been extensively used in determining ink printability and other properties for inkjet processes, but less so for EHD. Few studies which focus on EHD report these values, such as the work by Zhang *et al*.[147] These numbers provide a reliable framework from which experiments can be designed.

Viscous inks include polymers, ionic liquids, gels, oils, and organic solvents like glycerol. Higher viscosity inks have been demonstrated to form more stable jets during EHD printing, and hence more reliable resolution, so long as $Z < 10$, and the conductivity is sufficient.[158] Polymer material, such as polyvinylpyrrolidone (PVP) has been used to increase the viscosity of inks whose viscosity was too low.[159] With regards to response to electrostatic charge or potential bias, the hydrodynamic relaxation time is directly proportional to the viscosity (Equation 2.9).[146] In other words, higher viscosity translates to higher hydrodynamic relaxation time.

According to these Equations (2.9 and 2.10), droplet formation time increases with higher viscosity and decreases with higher surface tension or higher conductivity (i.e. either the droplet formation is driven by charge build up or by fluid flow). Thus, for successful EHD

printing, one needs to minimise the viscosity to ensure a short τ_q, whilst keeping the surface tension and conductivity relatively high for a fixed standoff height and nozzle width, but keeping in mind the formation of satellite droplets due to Rayleigh breakup.[121] Barrero reports that experiments have shown that a cone jet mode of EHD is only possible if $\tau_q < \tau_H$.[113] This is corroborated by Choi *et al.* and Edirisinghe *et al.* in their work.[160,161] Further, they report that for pulsed mode jetting, the pulse used should be greater than the hydrodynamic relaxation time and the Rayleigh time (that is, the minimum time required to form a stable jet) for stable jets to be produced.

2.2.9. Flow rate

A parameter which is rarely reported in the majority of work reporting EHD based printing, has been the flow rate. When analysing the force diagram of the EHD jetting phenomenon (Figure 2.1a), it is critical to remember that a back pressure is required to continuously supply fluid to the capillary tip for an equilibrium to be maintained. This pressure is maintained either by a static pressure, as in the work by Poellmann *et al.,* or a continuous flow of ink from a reservoir.[79] It has been reported that the hydrodynamic relaxation time is also related to flow rate by the following **Equation 2.12**,[161]

$$\boldsymbol{\tau_H = \frac{LD^2}{Q}} \qquad \text{(Equation 2.12)}$$

where *D* is the jet diameter, *Q* is the flow rate and *L* is the axial length of the jet.

Jet stability has been reported to increase (to a maximum value) as the flow rate increases for a given capillary diameter, conductivity and applied voltage, but this results in much larger droplet sizes forming, thus reducing the resolution of printing that can be obtained.[122,162] If the flow rate is increased to be much more than the jetting frequency, satellite droplets and large drops are likely (since $\tau_q/\tau_H > 1$). If the opposite is true, the printed features can either be discontinuous or vary significantly in width. Work by Scheideler and Chen on the scaling of Taylor cone jets introduces new understanding for high viscosity fluids. They propose that the minimum flow rate, *Q*, required to sustain a stable Taylor cone scales to the viscous diffusion

time as given by $Q_m \sim \gamma D^2/\eta$, where D is the nozzle outer diameter.[149] A similar relationship is observed if Equations 2.9 and 2.10 are combined and expressed in terms of Q. **Figure 2.6** illustrates the problem of poor jetting as a result of (a) insufficient flow rate, and (b) excessive flow rate, as reported by Yu *et al.*[69]

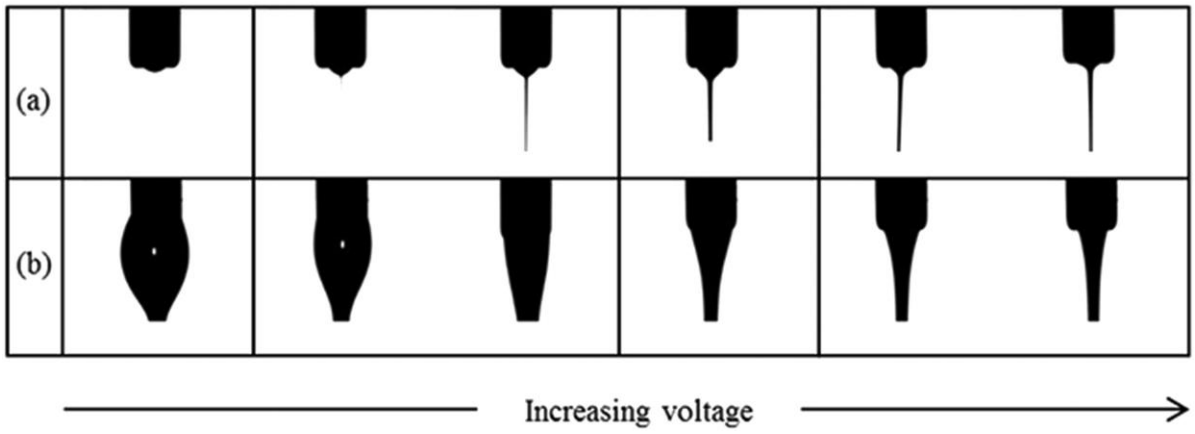

Figure 2.6. Evolution of cone jet of PEO (Mw = 1.0 × 10^6 g/mol, 0.38 wt.%) in Water/Glycerol mixture: (a) thin jet from the insufficient flow rate and (b) thick jet from the excessive flow rate. Reproduced from [69], Copyright 2016 with permission from Elsevier.

Similarly, for low viscosity liquids, with high conductivity, Barrero reports a minimum flow rate Q_{min} which scales as $Q_{min} \sim \frac{\varepsilon_r \gamma}{\rho K}$, where ε_r is the permittivity of the ink, γ the surface tension, K the conductivity and ρ the density.[114] Knowing which regime each ink is in can assist EHD users in understanding better the observed behaviour and how to achieve their desired outcome.

2.2.10. Ink development for EHD

Ionic liquids (IL) fulfil the criterion for a good ink. A significant drawback though of ILs is that they do not evaporate readily due to a negligible vapour pressure [163] and high viscosity.[164] This would severely limit the application of these as ink solvents in conventional applications, but potentially open new avenues of research as has been shown in their application in biomaterial delivery.[164,165]

Small organic molecules which fluorescence can be printed as ink when dissolved in the right solvent. They can also be mixed with a variety of other materials and can be utilized as an imaging tool in the printing process. The quest to achieve ever higher resolutions will also require that better metrology of printed features be performed. Scanning electron and confocal fluorescence microscopy are tools which could be utilized extensively to measure accurately the printing sizes achieved. Work incorporating fluorescent molecules as markers has not been fully developed. Sutanto *et al.* [166] demonstrate its capability. However, they have been investigated for use as organic light emitting diodes.

Liquid crystals (LC) are a type of mesophase material in that they possess the anisotropic properties of solids, and the fluid character of isotropic liquids. This makes them very sensitive to external field perturbations (electric, mechanical, magnetic and thermal). They have been shown to be good hosts for nanomaterials such as nanoparticles, quantum dots, bio nanostructures etc. With this in mind, high resolution printing of these hybrid structures could lead to very interesting applications in opto-electronics.[167] Currently, LCs have been aligned for applications using several contact and non-contact methods including the rubbed polymer technique, nanoimprint lithography, photo-alignment and ion beam alignment.[168]

LCs, owing to their unique properties, are likely to be able to act as good inks in the field of EHD, but no literature has successfully demonstrated this explicitly. Byun *et al.* used EHD (multi-mode printing) to deposit polyimide onto a substrate for LC alignment, but did not print the LC itself.[169] This presents a great opportunity to build up this body of knowledge from a high resolution printing perspective.

2.3. System parameters

2.3.1. Nozzle diameter, geometry and arrangement

The influence of the nozzle diameter on a variety of parameters or outcomes can be significant.[59] The final resolution obtained with EHD printing can be determined in the most part by this. Park *et al.* are the first to state that the nozzle diameter is a massive limitation.[38]

Schneider's pioneering work on the formation of out of plane nanopillars by nanodroplet autofocussing could not have been possible without the use of very small capillary nozzles (ca. 500 nm).[63] In addition to size, it has been demonstrated that the coating of the outside of conductive nozzle with a hydrophobic self-assembled monolayer reduces the meniscus size, thus promoting finer jets.[79] Work done by Stachewicz has demonstrated the massive difference in jetting when a capillary with no monolayer is used.[170] By using pristine nozzles (i.e. no surface energy modification agent), the droplet formed on the nozzle can be effectively bigger than the nozzle as it climbs up the outer surface by capillary action, akin to the ball-cone jet. This, in turn, makes the jet diameter larger than what it would have been if the meniscus had been limited to the true nozzle diameter. Looking at an example found in an inkjet printing study, He *et al.* study the influence of wettability within the capillary itself (**Figure 2.7 a,b**).[123] By increasing the hydrophobicity of the inner wall, they observe that droplet breakup occurs at a later point than that observed for a hydrophilic wall. This leads to a longer filament being formed, thus increasing the probability of stray satellite droplets forming. A hydrophilic inner wall, however, exhibits stronger adhesion to the ink, thus promoting shorter filament lengths, and quicker droplet breakup – giving better printing quality overall for the studied ink. Morad *et al.* discuss using extender caps on capillaries to enhance the Taylor cone stability (**Figure 2.7 c,d**).[122] They attach a hemispherical cap to the end of a stainless steel capillary, which can be wet by the ink being investigated. With this modification, they demonstrate a larger island of Taylor cone stability, thus allowing for a wider range of applied potentials as a function of the flow rate used (**Figure 2.7 e-g**).

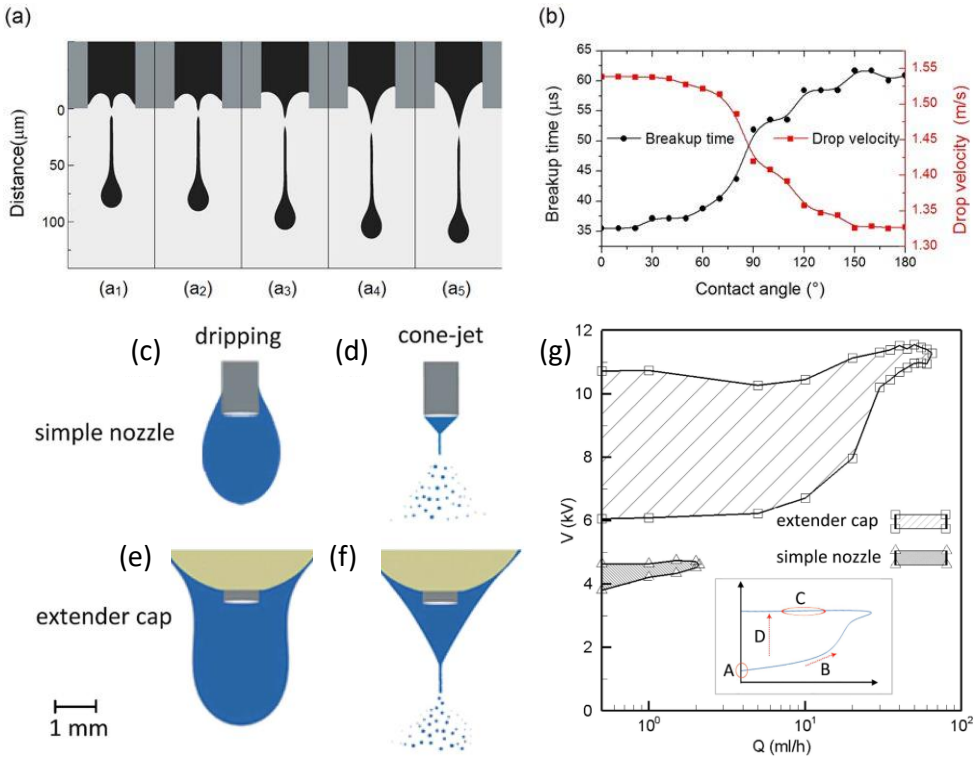

Figure 2.7. The nozzle wettability influences. (a) The ink droplet image at the moment of breakup. The contact angles of the nozzle inner wall and the breakup times are (a_1) θ = 30°, 37.14 μs; (a_2) θ = 60°, 38.78 μs; (a_3) θ = 90°, 51.89 μs; (a_4) θ = 120°, 58.45 μs; (a_5) θ = 150°, 61.73 μs. (b) The breakup time and droplet velocity changing with the wettability of the nozzle inner wall. The liquid rises the wettable nozzle outer wall in the dripping mode. Reproduced from [123] (c). After installation of the extender cap, the recess was small enough for rising droplet to reach the extender cap and adhere to its bottom surface (d). When the electric field is intensified the cone is formed with its base connected to the extender cap (f), instead of the nozzle tip itself (e). (g) The shaded regions show stability islands corresponding to the two nozzles. The inset shows a typical stability island with the corresponding zones. Reproduced from [122].

Coaxial needle geometries have also been explored, especially for biomedical applications, the formation of core-shell particles[171–173] or fibres[174] and hollow nanofibers[175]. The inner nozzle is used to extrude a different material to that which flows through the outer nozzle. Ahmad *et al.* reported a tri-needle coaxial arrangement which they used to form nanocapsules, layered bubbles and porous encapsulated threads, with the intention of eventually developing capsules for multistage drug delivery (**Figure 2.8 a-c**).[176] Several reviews exist which

summarize specifically this kind of work.[177,178] Multi-nozzle geometries have also been developed. Traditionally, nozzles used in EHD are needle shaped. This is owing to their availability and ease of use. Sutanto *et al.* produced an industrial system which consisted of multiunit print heads.[166] They also demonstrate a three nozzle system which they use to print micro-optical devices.[81] A multi-nozzle arrangement helps to improve the relatively low throughput seen in EHD printing. There can be, however, issues of interference between each nozzle in the electric field, leading to poorer printing quality and misalignment of structures. To overcome this challenge, Lee *et al.* designed and fabricated a multi-nozzle planar device from a silicon wafer. The spacing of the wafers, and their design, contributed successfully to producing individually controlled stable jets which showed no signs of distortion in the electric field. By designing their system as a microfluidic device, they were also able to control effectively the flow rate such that the jetting voltage could be kept constant (**Figure 2.8 d,e**). A wetting control was also used (Teflon) to prevent excessively large pendant drops from forming.[179]

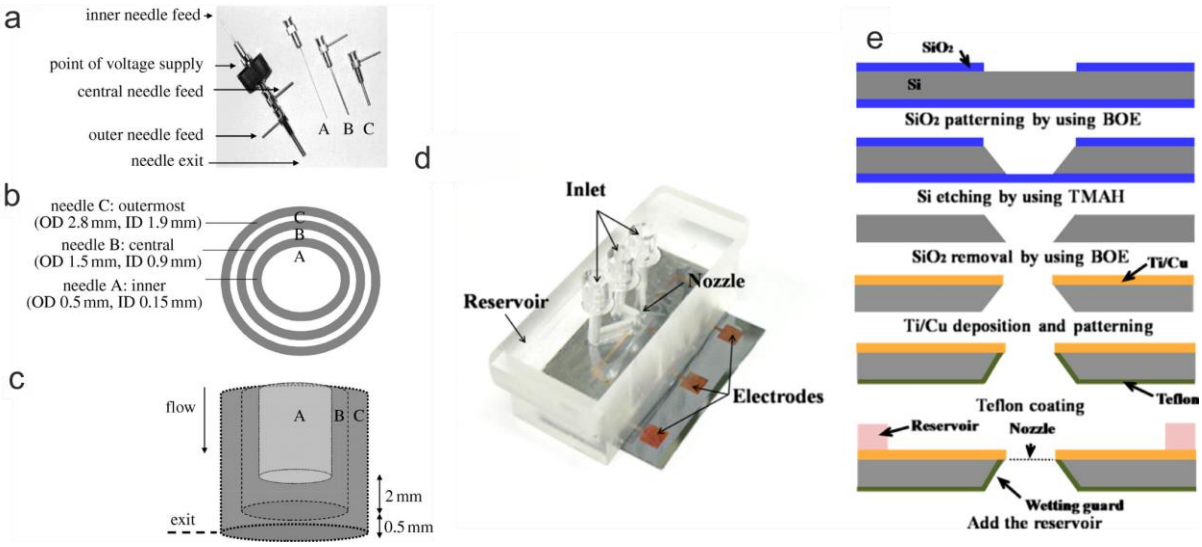

Figure 2.8. Details of three-needle coaxial device: (a) needle assembly, (b) needle dimensions and (c) relative placement of needles in device. ID and OD represent internal and outer diameters, respectively. Republished with permission of Royal Society, from [176]. (d) Fabricated multi-nozzle and (e) fabrication flow chart of the multi-nozzle. Reprinted from [179], with the permission of AIP Publishing

Concluding, the enhancement of the resolution obtained in EHD printing can be promoted by customizing the nozzle size or geometry and by using common surface modification methods. Depending on how fast the process is intended to be, introducing multi-nozzle heads can increase the throughput significantly.

2.3.2. Applied potential, tip-substrate separation and operating conditions

The applied potential and standoff height essentially control the magnitude of the electric field generated, directly and indirectly respectively. The standoff height needs to be large enough to allow for the formation of a jet, whilst being small enough to not allow droplet pinching over time as the jet starts to disintegrate if the stable cone jet is the mode desired, and for a constant potential. It has been demonstrated too that a standoff height that is too high can facilitate increased wetting as a result of splashing.[105] Laurila *et al.* demonstrate more uniform droplets using a smaller standoff height for a fixed applied voltage.[128]

As already mentioned, there exist several modes of stable EHD printing. Continuous jet printing, as the name suggests, involves a continuous flow of material from the nozzle onto the substrate.[180] The applied potential is kept constant such that the ink continues to eject uninterrupted until the desired pattern is achieved (**Figure 2.9 a-d**).[181] This mode is most commonly achieved with a DC voltage. The balance between flow rate and applied bias must be kept in order for regular printing to be achieved. A discrepancy in this balance can lead to broken patterns, bulging or a splurge of material which no longer resembles printing. The speed of the translational stage on which the substrate sits can aid in achieving high quality continuous printing. This has been studied in-depth by Phung *et al*. [182–184]

Drop-on-demand (DOD) printing is a mode where drops are deposited in precise positions by the application of a jetting pulse (**Figure 2.9e**).[185] This mode is generally achieved by using superimposing AC bias over a constant DC bias, but can also be achieved using DC voltage alone in an unsteady mode. If the inter-droplet distance is small, coalescence of the droplets is observed and a continuous print pattern can also be achieved.[51] Generally however, drop-on-demand EHD is used to generate patterns where discrete points are advantageous. Park *et al*. demonstrated DNA-directed nanoparticle assembly and DNA-aptamer bio-sensing based on DOD printed patterns.[71] Zhang and co-workers presented 3D printed nanostructures with aspect ratio over 35 printed using DOD EHD.[139]

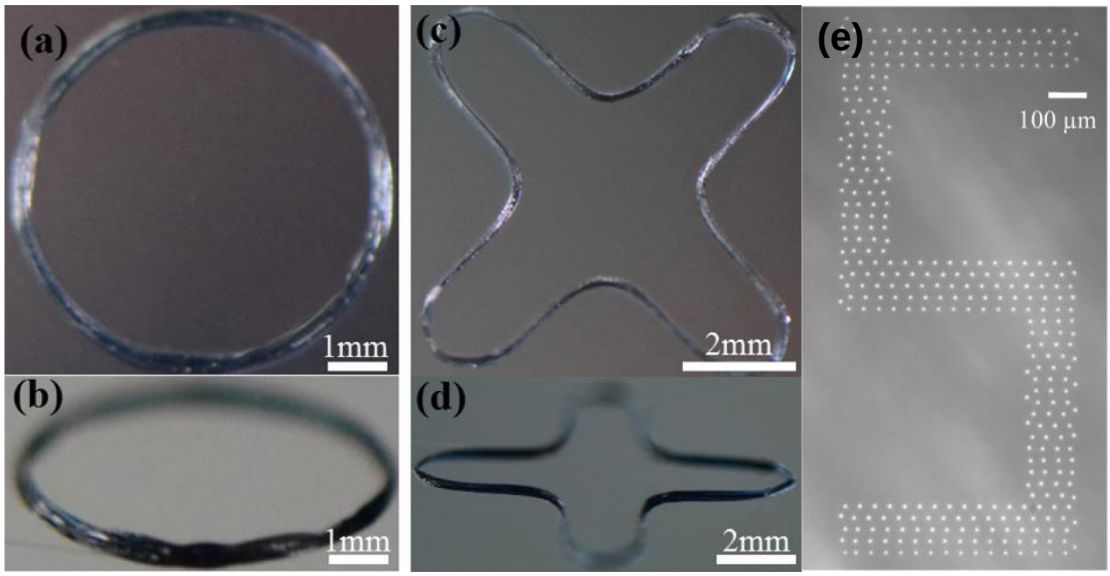

Figure 2.9. EHD printing of multilayer curved PEDOT:PSS-PEO features. (a,b) Optical photos of circular features with a layer number of 200. (c,d) Optical photos of 300-layer curved features. (Reprinted adapted with permission from [181]. Copyright 2018. American Chemical Society.) (e) Drop-on-demand printed "S" on glass slides with printing speed and droplet dimension controlled by the parameter of the AC-pulse voltage. © IOP Publishing. Reproduced with permission. All rights reserved

As previously mentioned, the applied potential needs to supply enough electric stress to overcome the surface tension whilst not providing excessive charge, which would lead to multiple jets being formed.[122] The variety of jetting modes which can arise due to different applied potential conditions has been extensively documented.[55] The majority of EHD studies utilize DC voltage to induce printing. If performed onto insulating surfaces, this can lead to

poor resolution as the ink droplets would be highly charged, and therefore repel each other. Wei *et al.* introduce an AC-modulated EHD process which can achieve good printing, by overcoming the above limitation.[185,186] Using high dielectric constant inks also increases the risk of charge build-up and breakdown. To prevent this, more sensitive inks are printed in vacuum or inert gases such as nitrogen or argon. This kind of printing requires more resources than what is conventional for EHD, and so comes with a slightly higher cost.

Sammons *et al.* present one of the first investigations into how humidity and environmental temperature affect the EHD process.[110] By assessing the quality of the printed adhesives they studied in different conditions, they concluded that humidity had a minor effect on the overall printing behaviour. However, temperature had a more pronounced influence, resulting in printed droplet diameter increasing as temperature increased. They also noted that at higher ambient temperature, the initial jetting voltage decreased, as did the jetting frequency. This correlates with the discussion earlier in this work regarding surface tension and temperature. Ongoing investigations into all these factors will inform better quality printing.

2.4. Substrate considerations

2.4.1. Chemical control

Control of printing resolution does not only depend on the actuation method, but also on the chemistry of the surface being printed on. The chemistry of the surface determines surface energy. High energy surfaces ($\theta_C \leq 5°$) are highly wettable. This means that any printed material will spread extensively in order to minimise the potential energy. The main method of controlling the surface energy of substrates is by the use of self-assembly monolayers, which impart hydrophobicity or hydrophilicity depending on their terminal chemistry. A detailed look through published reports reveals that the main molecules used are thiol based, silane based or halogenated moieties. Jeong *et al* [68] investigate two such monolayers, as well as polymer thin film coatings to assess the effect on the printing morphology and resolution. They utilized Si wafers with a 300 nm SiO_2 layer which had been cleaned in hot piranha solution. This

hydroxylated the surface and prepared it for further modification. The monolayers assessed were 1H,1H,2H,2H-perfluorooctyltriethoxysilane (F-SAM) and octadecyltrichlorosilane (ODTS) in toluene. The polymers (poly(4-vinylphenol) and ethylene-norborene cyclic olefin copolymer) are commonly used as coatings for electronic devices due to their thermal stability. They reported the smallest print widths were obtained with F-SAM (due to the polarity of the fluoro groups), but they observed periodic bulging in the printed lines (**Figure 2.10**). They attributed this not to surface chemistry, but rather to an over delivery of ink to the tip (excessive flow rate). This was overcome by speeding the substrate stage up during printing in order to allow for less ink accumulation on a particular spot. In essence, what they found was that as the surface energy decreased, the width of the printed lines also decreased compared to lines printed on a bare substrate. Interestingly, when they performed electric characterization of the printed lines, they found that the lines printed on the ODTS surface performed better every time due to a higher order of crystallinity imparted by the ODTS on the ink, poly(3-hexylthiophene) (P3HT).

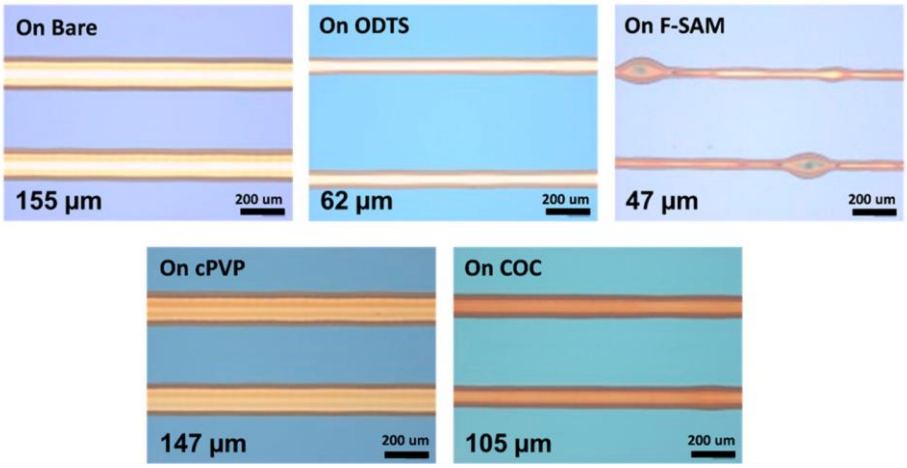

Figure 2.10. Optical images of the P3HT lines on differently modified surfaces. Reprinted with permission from [68].Copyright (2014) American Chemical Society.

In a similar study, Kwon and his co-workers showed just how much the surface energy has a role to play in the wetting behaviour of solvents used (**Figure 2.11**).[67] They compare a low viscosity silver ink with a silver paste on several surfaces including glass, polyvinylpyrrolidone

(PVP) coated glass, polyethylene terephthalate (PET) and polyethylene naphthalate (PEN). They utilized an AC voltage (which aided in overcoming the bulging issue observed by Jeong *et al* [68]) to achieve printing from relatively large nozzles (25 µm for low viscosity; 50 and 100 µm for paste). By printing on a plasma cleaned bare glass surface (very high energy), poor resolution and adhesion were obtained for both inks. This is also due to the unwanted hydrophilicity imparted by the plasma cleaning. The PVP glass displayed better adhesion and thus better resolution. The printing on the plastic films also corroborated the idea of low surface energy leading to better resolution, as the PEN surface was better than that of the PET.

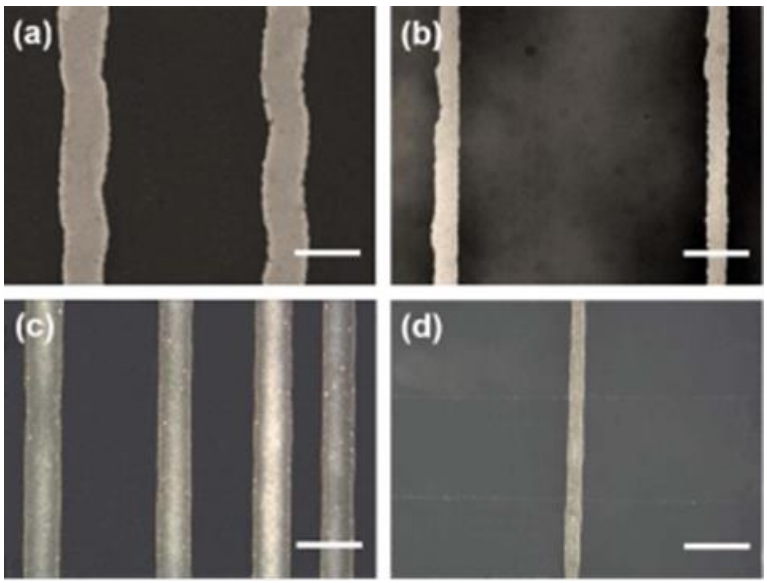

Figure 2.11. Optical images of printed Ag lines. Printed Ag nanoink on (a) PET film and (b) PEN film. Printed Ag nanopaste on (c) PET film and (d) PEN film. Scale bars are 100 µm. Quality of printing appears better on PEN than on the PET. Reprinted with permission from [67]

The adhesion of ink to a surface must be considered. As shown in nature, it is possible to have hydrophobic surfaces which have good adhesion and those which have poor adhesion. This is demonstrated by Bao *et al.* in their development of superhydrophobic yet highly adhesive surfaces.[187] A commonly used test for adhesion is the Scotch ® tape test, where a piece of Scotch ® tape is placed over a feature and pulled off. If the feature stays on the substrate, it is well adhered.[188]

Any future work done in this area must ensure that these facets are carefully considered in the choice of surface modification performed, and the type of surface preparation utilized. Functionality versus the resolution is a trade-off that must be considered critically.

2.4.2. Physical control

Wettability is also a function of the microscale roughness of a surface.[189] For instances where more long term hydrophobicity is desired, the use of physical features can be beneficial. These features can either be lithographically patterned, or introduced additively. Wang *et al.* demonstrate how the surface structure determines the wettability that can be obtained.[190] They lithographically patterned micro-pillars into silicon wafers, keeping height (h) fixed and varying the length (a) and width (b) (**Figure 2.12**). They define the roughness as $[(a + b)^2 + 4ah]/(a + b)^2$. Having patterned these features (smaller than those previously reported), they then performed wetting experiments using three different solutions with similar surface tensions and different viscosities, and compared the results to wetting on flat substrates.

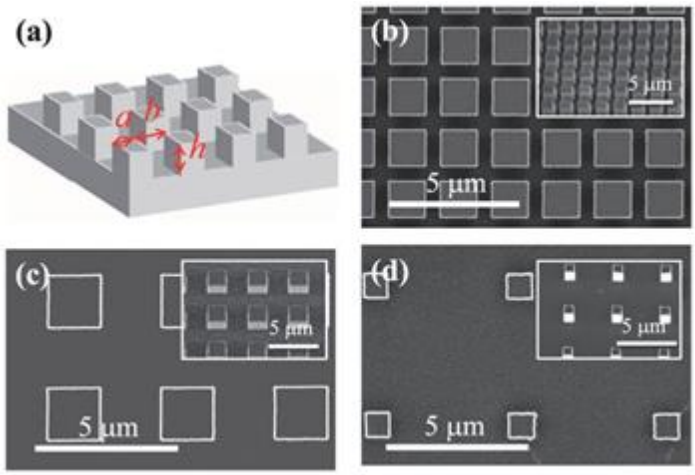

Figure 2.12. Surface features for wetting control. (a) Schematic showing terminology for pillar width a, separation b and height h. (b–d) Scanning electron microscopy images of representative micro-structured surfaces for (b) b/a= 1/3, (c) b/a = 1, and (d) b/a = 4. Reproduced with permission from [190].

They found that the surface structure geometry greatly influences the dynamic wetting. They suggested then, that it is possible to control the non-equilibrium wetting behaviour by appropriate surface engineering.

Other means of inducing surface roughness for wetting control have been demonstrated, including the use of dense nanoparticle arrays,[191] laser ablation treatment,[192] polymer wrinkling,[193] mechanical abrasion, vapour deposition, creating bio-surface, electrochemical deposition and others.[194] The substrate being used would determine which process would be most appropriate to induce the roughness desired.

2.4.3. Electrical control

The electrical properties of the surface being printed on are the final intrinsic consideration. Whilst they do not directly contribute to the resolution of printing obtained, they can contribute to the quality of features achieved. For instance, Bu *et al.* looked at the EHD process when considering an insulating, dielectric and conductive substrate. They found that the substrate type plays no role in the jetting voltage, however the jet character is influenced.[195] **Figure 2.13** shows how the evolution of the jet differs for substrates of varying electrical characteristics.

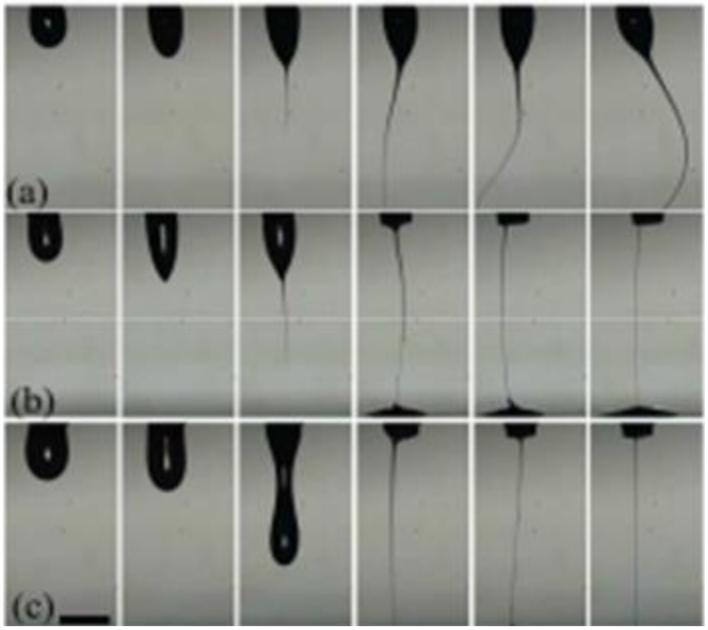

Figure 2.13. The formation process of the jet over the different substrates. The nozzle-to-substrate distance H is fixed at 2 mm, the flow rate is Q=50 nL/min, and the substrate is still. (a) PET. (b) Silicon. (c) Steel. Republished with permission [195].

Their work carries on to state that when the charge relaxation time of the substrate is lower than the jet lifetime, the deposited material will form uniform straight lines. However, when the substrate charge does not dissipate before the jet lifetime, whipping instabilities occur leading to disordered printing, most commonly observed for polymer near-field electrospinning. This was observed in my own work when I attempted to print poly(methyl methacrylate) (PMMA) **(Figure 2.14**). This work supports the earlier stated reasoning for using AC voltage on insulating substrates, to prevent charge build-up and allowing for printing to occur.[185]

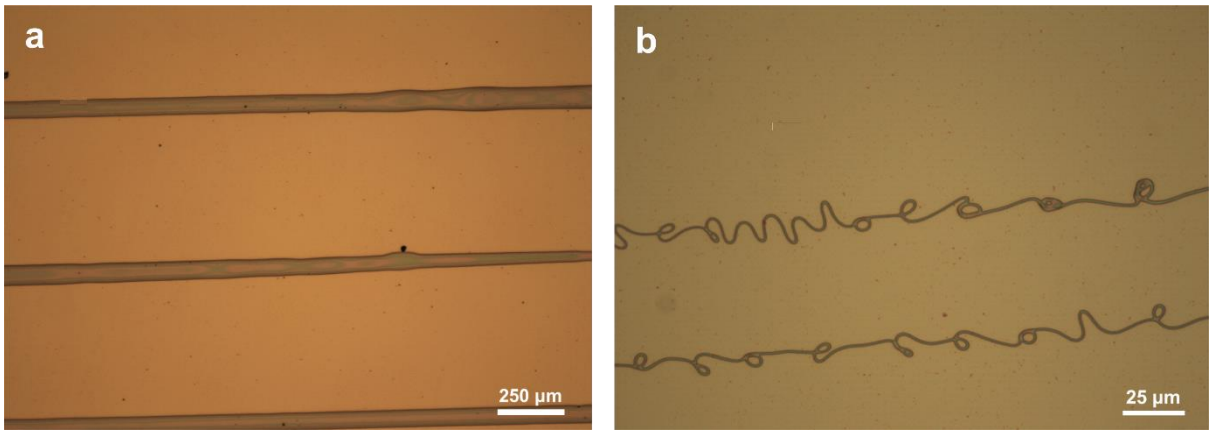

Figure 2.14. EHD printed PMMA. (a) Regular patterns with relatively large line width owing to sufficient discharge occurring before jet lands on substrate. (b) Nonlinear lines due to whipping instabilities introduced by excessive applied bias. [Unpublished work].

2.5. Chapter summary

Having examined each of these parameters in more detail, it is possible to see just how much consideration is required to achieve the desired EHD outcome. EHD printing is a complex process. It can be made simpler by using Newtonian fluids with known properties including conductivity, surface tension, and viscosity. Knowing how these can affect the desired stable cone jet better informs the programming and selection of system parameters including flow rate, printing voltage, nozzle size, standoff height. Other factors such as ink dielectric strength, and environmental factors such as humidity and temperature can also affect the final outcome, and so need to be controlled for reliable results. Certain ratios, such as τ_q/τ_H can be very helpful

in determining whether printing can occur or not, and thus inform the choice of inks. Raje *et al.* recommend that a library of printing conditions be compiled for commercially available inks so that future EHD users may not have to spend excessive amounts of time optimizing printing conditions.[56]

As the scope of additive nanomanufacturing grows, the role of electrohydrodynamic jet printing will become ever more important, owing mostly to the wide range of fields it can be used in (biological, biomedical, materials processing, electronics, etc). In the following chapter, I demonstrate the practicalities of setting up a custom system, and the associated preliminary experiments and calibrations.

Chapter 3

Experimental methods & Technique development

3.1. Introduction

In this chapter, I introduce how the electrohydrodynamic jet printer used in this thesis was set up. I also explain the motivation behind the initial experiments performed, and describe the metrology used. Many manufacturing techniques which aim to achieve high resolution are used within the confines of cleanrooms or environment controlled glove-boxes. In order to make rapid prototyping more accessible, the systems used to achieve it need to be able to operate in less controlled spaces. For this reason, there is no humidity or temperature control on the system described below, neither is there a high resolution CCD camera. The microscope used to look at the tip during printing is of sufficient resolution as it is not the scope of this work to study the droplet formation or jetting.

Figure 3.1a is a schematic which demonstrates how the different components of the EHD printer work together.

3.2. Equipment

The printing experiments presented in this work were done on a home-built system with components I list below. Using various literature sources as a guide, the setup (**Figure 3.1b**) was constructed.[4,14,63,196] The components of the system include the following:

- Physik Instrumente L-511 High Precision Linear Stage (for X-Y movement) (**Figure 3.1c**)
- Non-isolated DC-DC Converter dc Input, 0 – 10 kV output, 500 μA (**Figure 3.1d**)
- Tektronix PWS4205 Programmable DC Power Supply (0 – 20V, 5A) (**Figure 3.1e**)
- Aladdin NE-1002X microfluidic pump (**Figure 3.1f**)
- Z825B 25 mm Travel, DC actuator (for Z-axis movement)
- DinoLite AM4113TL Microscope
- Laptop installed with Physike Instrumente custom software to control stage movement.

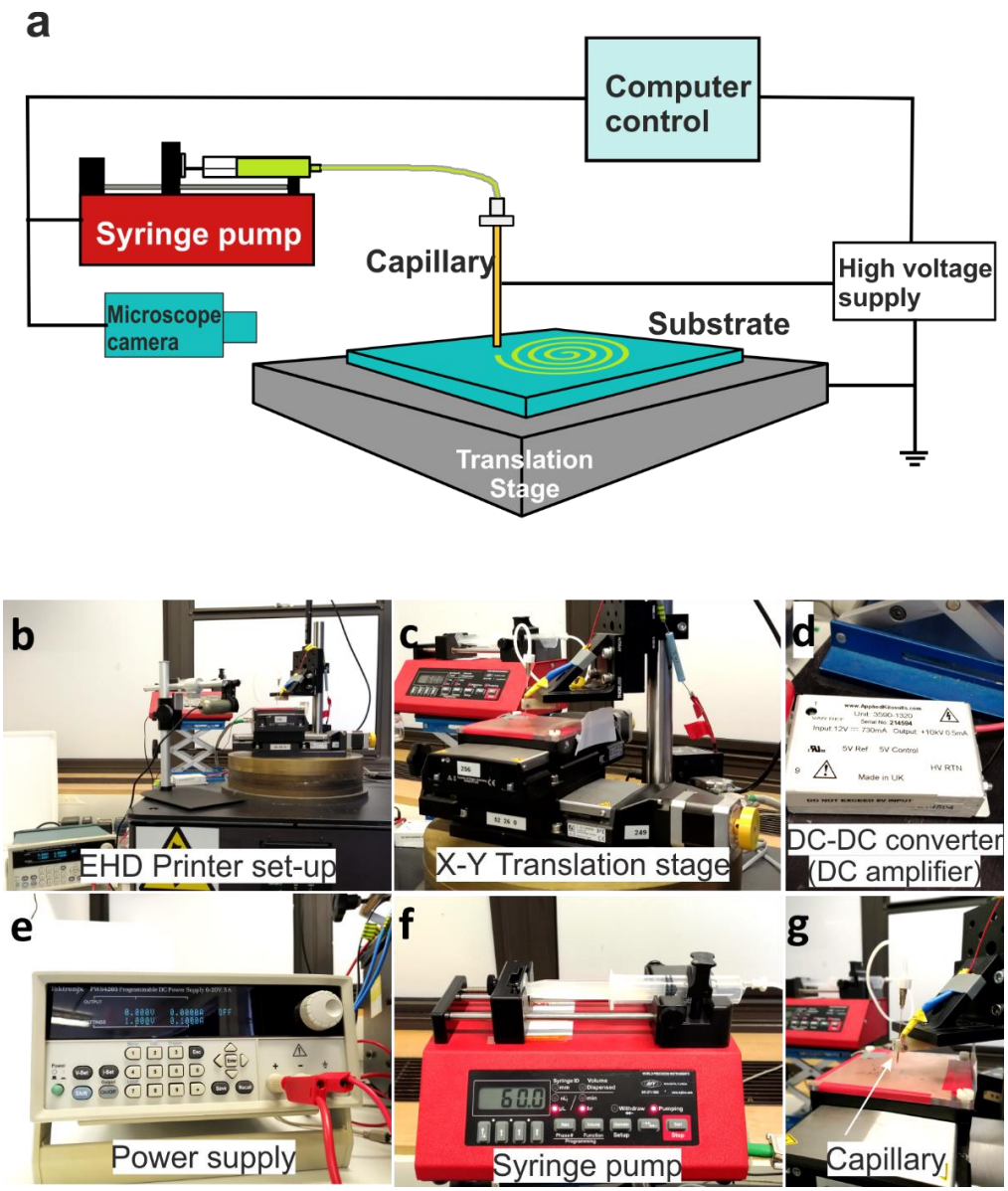

Figure 3.1. EHD printing schematic and setup**.** a) A cartoon schematic showing the essential components of an EHD printer. b) A wide view of the printing setup custom built for the work presented in this thesis, with a close up of c) x,y stages, d) DC amplifier, e) DC power supply, f) syringe pump, and g) gold coated printing capillary.

3.3. Preparation of glass pipettes

3.3.1. Metal coating

Luer head glass pipettes of various tip diameters were purchased from World Precision Instruments (**Figure 3.2a**). In order to use them for EHD printing, they were coated with 50

nm of indium tin oxide (ITO), a transparent conductive material, using a Nordiko RF sputtering system. It was found, however, that the ITO being deposition was not consistently conductive, therefore an Edwards thermal evaporator was employed. The tips were coated with 10 nm chromium (adhesion layer) and 50 – 80 nm gold. The high conductivity of the tip made it possible to apply the electric potential required for the printing.

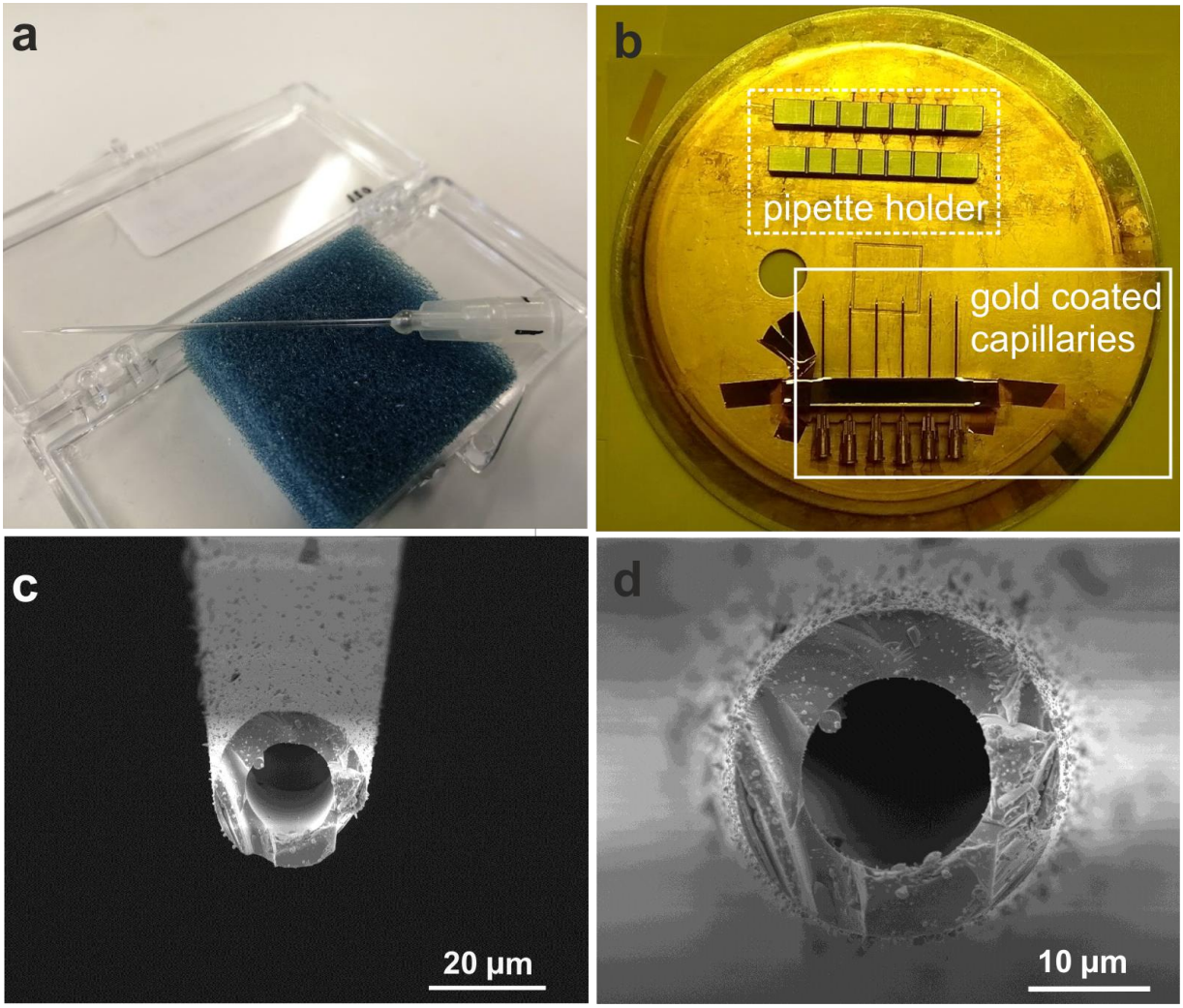

Figure 3.2. Pipette preparation. a) Glass pipettes are bought from a supplier uncoated. b) Using a custom made holder, the pipettes are thermally evaporated with chromium and gold to make them conductive. c) SEM imaging can then be used to observed the tips and ensure that they retain their diameter. d) An example of a 15 µm pipette before being used.

A custom made aluminium holder was machined, that was able to accommodate up to six pipettes **(Figure 3.2b)**. Once the pipettes were secured and affixed to the evaporation plate,

the first round of evaporation was done, and then the pipettes turned over and evaporation completed. This process resulted in a uniform layer of gold on the capillary. In order to ensure that the integrity of the tip was preserved after evaporation runs, selected tips were often examined using SEM (**Figure 3.2 c,d**). This allowed me to examine whether the metallization process was safe to use, or whether too much damage was being done. Overall, a survival rate of 85% was obtained for the tips prepared in this way.

Before use, each pipette was chemically treated with *1H,1H,2H,2H*-perfluorodecanethiol (PFDET) in order to make the tip hydrophobic, and prevent meniscus broadening. Briefly, a solution of 10 mM PFDET was prepared in ethanol. The pipette was rinsed for 30 seconds in 50 mM HCl, then acetone and then immersed in the PFDET solution for a minimum of 12 hours. After this, it was gently rinsed in fresh ethanol, and then dried with a nitrogen gun. The imparted hydrophobicity prevented the formation of a large pendant droplet on the outside of the nozzle. This means that the meniscus was kept to a minimum, thus promoting higher resolution printing (**Figure 3.3**).

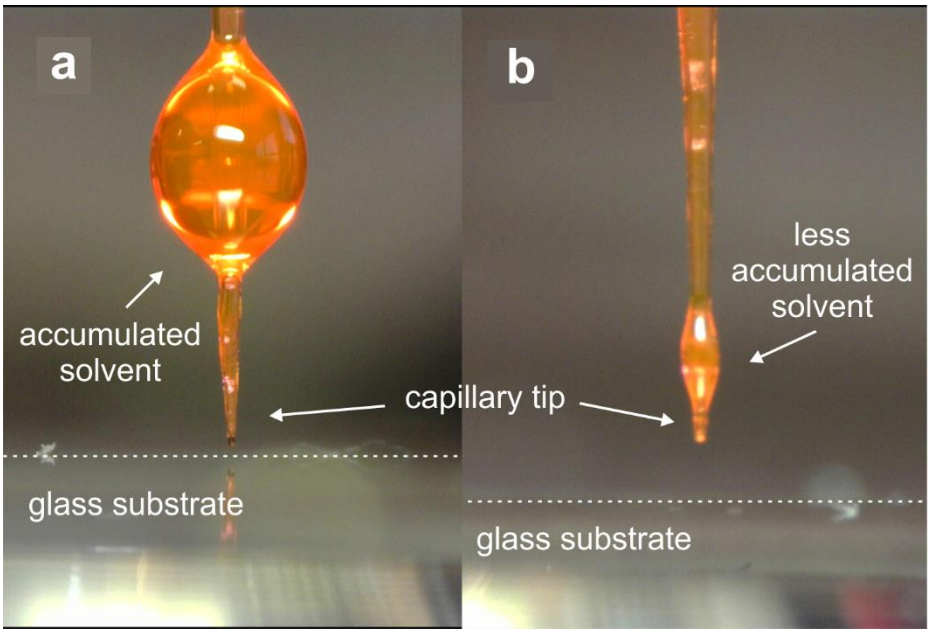

Figure 3.3. Images of micropipettes taken during printing. (a) The photograph shows a large solvent bubble accumulated on the surface of the pipette with no POTS whereas (b), is a POTS treated surface and shows a smaller solvent bubble. In both cases, the ink includes tetradecane, THF, silver nanoparticles and pyrromethene-597.

3.3.2. Ink loading

After several unsuccessful initial attempts to load ink into the glass capillaries with 5 or 10 mL syringes, an alternative method was found for doing so successfully. This involved using a micropipette loader to deliver ink to the very end of the pipette. This turned out to be very important, as the capillary forces in the pipette would prevent ink flow to the tip if a small gap was left, leading to the loss of many tips. A lack of sufficient ink flow leads to arcing of the printer (**Figure 3.4b**), as charge build up on the tip in the absence of a dissipating medium would result in enough potential for dielectric breakdown of air (especially at near-field lengths). This also lead to interesting tip disconfigurations (**Figure 3.4 c,d**).

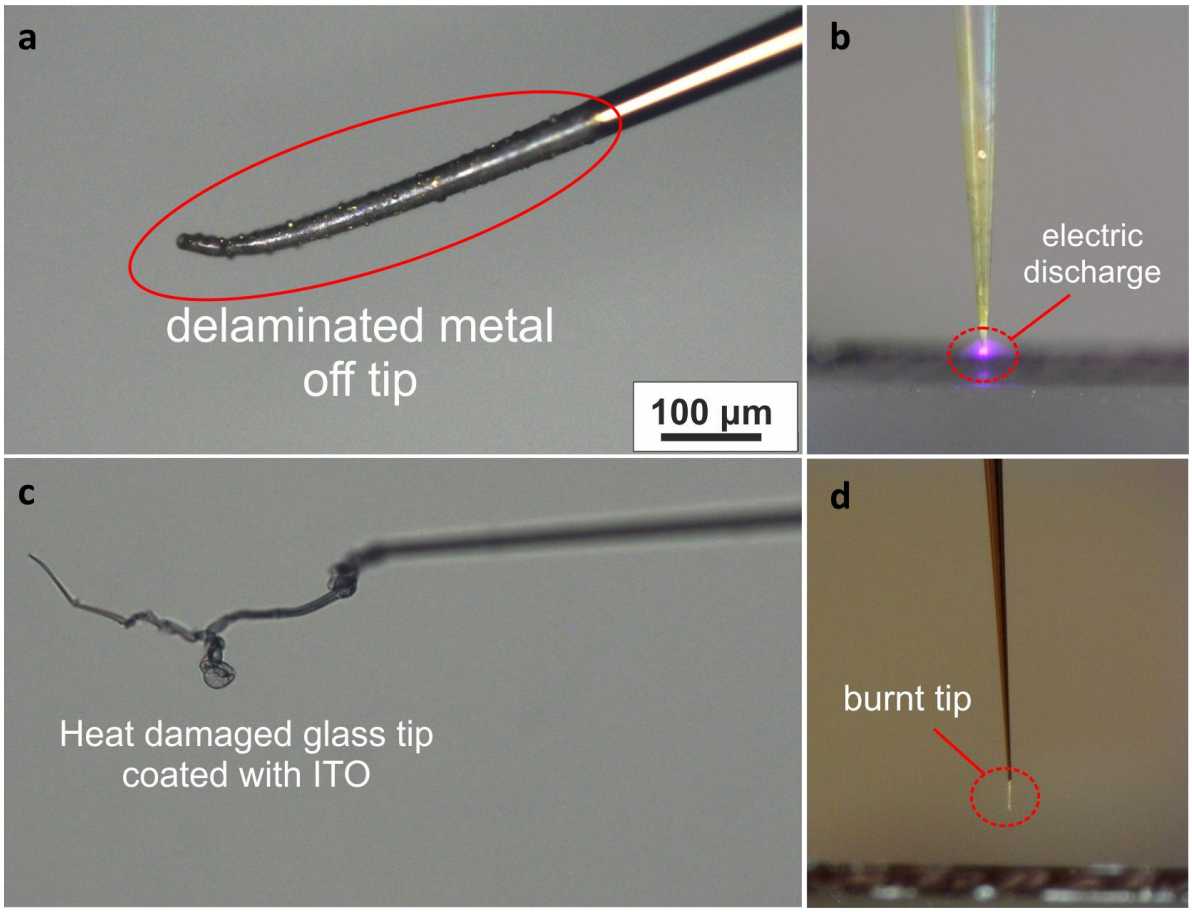

Figure 3.4. Damage to pipettes. a) Localized heating causes the tip to bend, due to b) an arcing event. When there is no ink at the tip, interesting damage as that seen in c) with very high voltage and d) is observed.

3.3.3. Influence of capillary size

Over the course of this study, I have used tips of varying sizes, from 100 nm to 150 μm in diameter. It is considerably more challenging to use the smaller end tips owing to their propensity to damage, but also for their more frequent and pronounced clogging. Only low viscosity solvents or highly dilute solutions could be used with smaller diameter tips. However, with larger tip diameters (larger than 5 μm), more inks could be used, including concentrated colloidal suspensions, with the advantage of requiring lower jetting potentials. Ideally, metal tips, such as steel nozzles, should be used for EHD printing, as they would be reusable, and easier to connect to a printing setup. However, the use larger capillaries prevents the attainment of very fine structures on the nanometric scale. Further, a plot of **Equation 2.6** *(*$\mathrm{E} = 4\mathrm{V}_0 / \left[\mathrm{d}_\mathrm{N} \ln\left(\frac{8\mathrm{H}}{\mathrm{d}_\mathrm{N}}\right)\right]$) reveals that the tip diameter has a great influence on the magnitude of the electric field, meaning that for larger tips, less electrical stress is needed to induce printing (**Figure 3.5**). The stand-off height here has a smaller role to play.

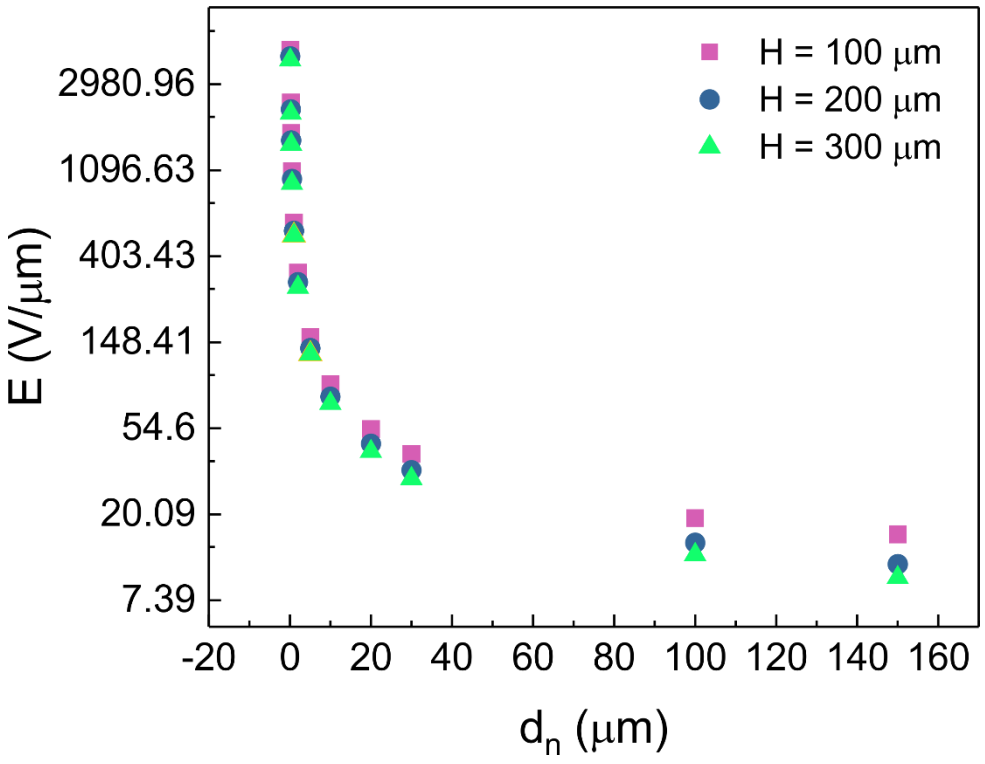

Figure 3.5. Electric field as function of nozzle diameter. Electric field strengths required generated from Equation 2.6 to determine the relationship between electric field strength and nozzle diameter. The relationship is logarithmic, with very little influence from the tip standoff height.

3.4. Substrate preparation

3.4.1. Wafer dicing

Wafer pieces were diced from large 4 inch substrates using the Loadpoint Microace Series3 dicing tool, with a diamond blade for cutting silicon wafers. Before use, all wafers were thoroughly rinsed in deionized water to remove any silica residue.

3.4.2. Piranha cleaning

Piranha acid was used to clean some of the substrates used in this work. It was only used whenever self-assembled monolayers were grown on the substrates.

A 4:1 ratio of sulfuric acid and hydrogen peroxide was slowly prepared dropwise with constant stirring. **CAUTION**: Rapid addition of the H_2O_2 to H_2SO_4 could result in an explosion. After the initial reaction cooled down, the acid solution was heated to 100 °C and the wafers cleaned

for 30 minutes, under constant supervision. Once cooled, the wafers were removed from the acid and rinsed in hot deionised water, followed by a second rinse in fresh water before finally being used or stored in beaker of sealed, clean, distilled water.

3.4.3. Oxygen plasma cleaning

Further cleaning of the wafers used in this work (or hydroxylation) was done using oxygen plasma treatment (Diener Electronics Zepto model). The wafers being treated were loaded onto a ceramic crucible and exposed to a DC plasma of 60W for varying lengths of time. A quick assessment of the wetting properties of the substrates with a drop of water confirmed that the treatment had been successful. Fully hydroxylated surfaces wet completely with water (contact angle < 5°).

3.5. Metrology

Various forms of metrology have been employed in this work. Below, a list is given.

- Atomic force microscopy including Kelvin Probe microscopy, contact mode and scanning mode scans.
- Optical Microscopy
- Scanning Electron Microscopy
- Energy-dispersive X-ray spectroscopy
- X-ray photoelectron spectroscopy
- X-ray diffraction spectrometry
- Ultraviolet/visible spectroscopy
- Contact angle measurements using custom setup
- Bubble Tensiometer to determine surface tension of inks
- Thin film ellipsometry

3.6. Preliminary experiments/Setup Calibration

3.6.1. Initial printing trials

Preliminary experiments were conducted with the custom-built setup to ascertain whether all the components work (the microfluidic pump was only added after the initial experiments). The initial aim of this work was to be able to achieve sub-micron resolution with any printed material. In order to achieve the detection of this, it was thought to use a chromophore material to aid in visualization of printed structures with confocal microscopy. To that end, I used pyrromethene-597, a common material used in dye-lasers, which is soluble in most organic solvents, and added to it a silver nanoparticle tetradecane dispersion. I used 500 nm inner diameter indium tin oxide (ITO) coated capillaries for these first set of experiments, much to my disadvantage. The biggest challenge faced at this early point was getting ink to reach the very tip of the pipette. Any air trapped in the tip during ink loading led to occlusion, especially in tips with a smaller radius (**Figure 3.6a**). This led to several tips having to be broken gently to allow for easier ink flow (**Figure 3.6b**), and thus printing. **Figure 3.6 c,d** illustrates the printing that was obtained. Whilst the printing quality was poor, the idea of using PM-597 as a fluorescent aid to visualize the printing was successful, as has been shown mainly in biological studies.[197] However, it was not achieved at a sub-micron scale. Various factors contributed to the large printed features. The first of which was the lack of printer optimization at this early stage of the printing.

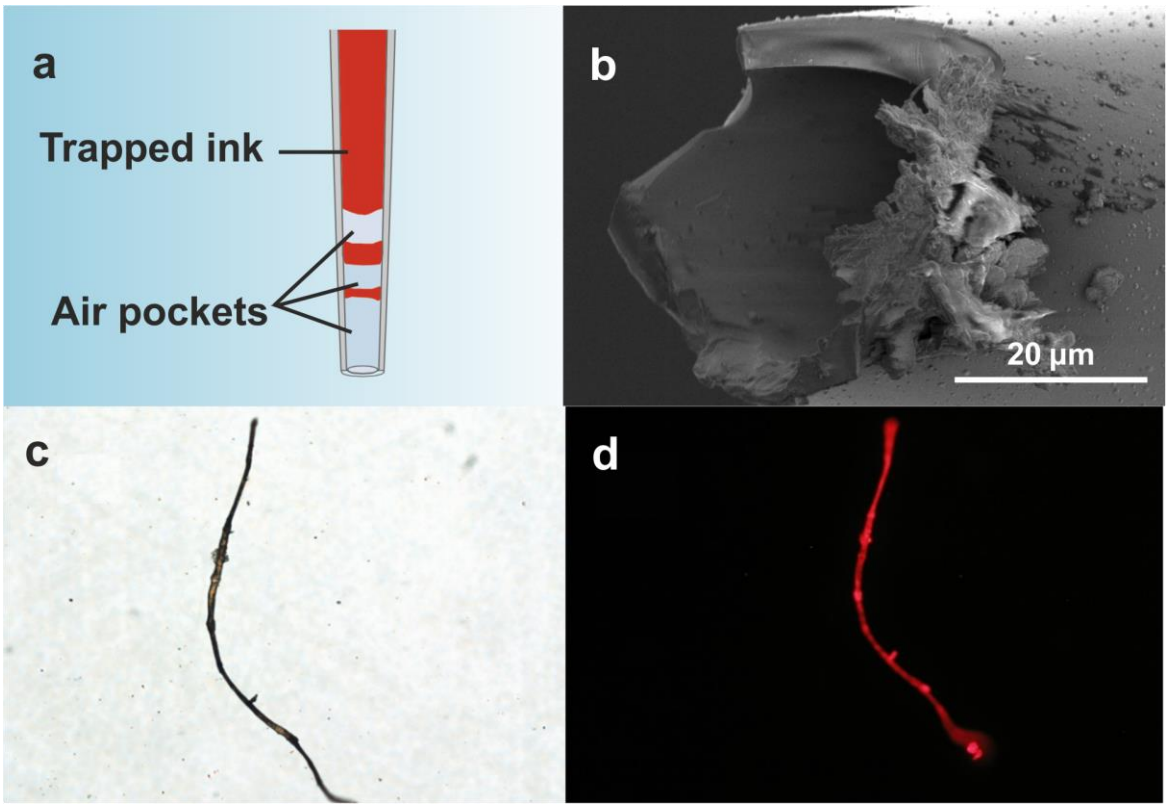

Figure 3.6. a) Drawing showing how poor ink loading to the tip of capillary leads to air pockets forming, which prevent printing from occurring. b) A tip broken in order to alleviate the blockage due to poor ink loading. Printed AgNP/PM-597 lines (c) under optical microscope, (d) under fluorescence microscope. The average width of the line is 13 µm.

Secondly, the substrate on which this printing was done was not prepared in any way apart from an acetone and isopropanol rinse. Whilst not successful in this trial, I learnt that using very small capillaries, whilst possibly the best way to achieve high resolution, was not the most efficient method. This led to the idea of experimenting with the different variables which EHD printing allows us to manipulate.

3.6.2. Testing of variables

Understanding the conditions which lead to each of the scenarios depicted in **Figure 3.7** are imperative for the successful application of EHD printing, and its adoption as a manufacturing method in industry. Much work has been done in elucidating how the jetting is affected by applied potential, flow rate, ink properties and substrate properties, amongst others.[60,160]

Whilst knowing this theoretically is important, a practical understanding of my own system was more crucial, and proved to be one of the more time-consuming and arduous aspects of the work presented in this thesis.

From literature, various jetting phenomena are possible during EHD printing. Over the course of the experiments performed in this thesis, this became quite apparent. Figure 3.7 illustrates some of the different jetting modes obtained. Each image is from a different experiment and is only placed in this figure for illustrative purposes. Figure 3.7a depicts regular, repeatable and continuous line printing. This is the ideal case of printing, where the jetting frequency and substrate translation speed are well aligned. This ensures equal deposition. Figure 3.7b is representative of a good jetting frequency, but slow substrate translational speed. This results in beads of ink forming owing to over-delivery of material in one spot. Whilst not ideal, this type of print does still allow us to use the printed ink as a conductive material (if that is the objective in that particular case). Figure 3.7c represents

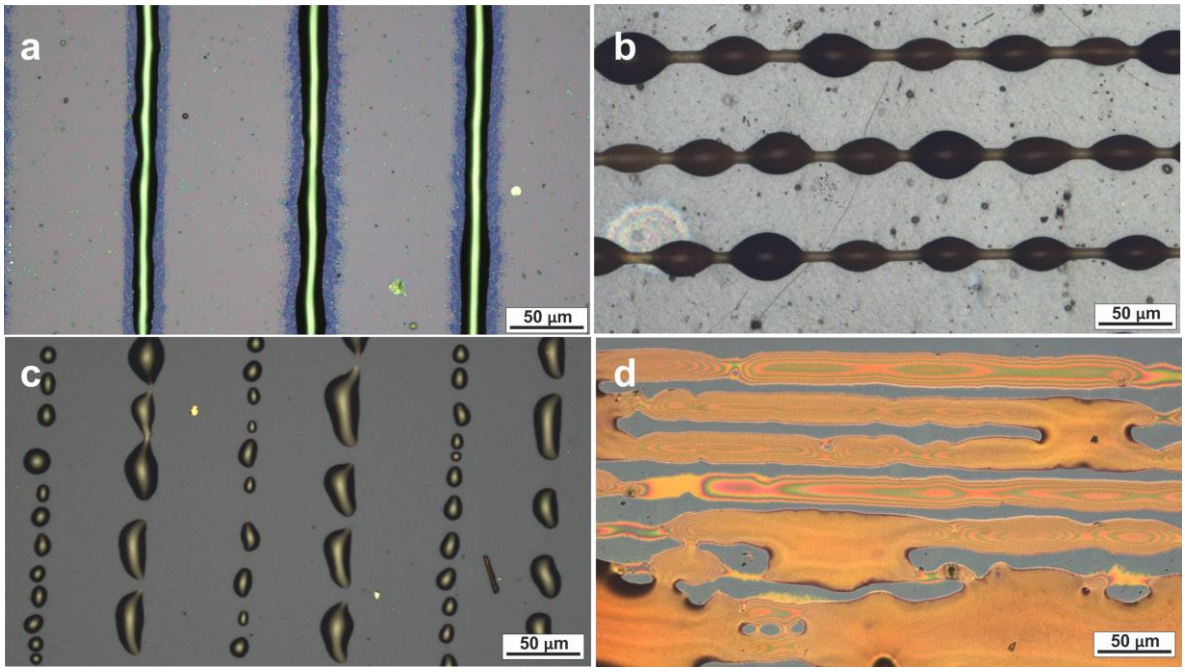

Figure 3.7. Printing types. Printing regimes obtained on silica substrate from various printing trials. Depending on how the printing potential is applied, the above pictured scenarios can occur. a) Continuous line printing, b) Beading/bulging, c) Discontinuous printing, and d) coalescence

undesirable drop by drop deposition[4]. There are various causes of this type of printing. Either the substrate is moving much faster than the ink being delivered; or there is a very high energy surface, causing discontinuities as a result of poor wetting. There could also be a problem of insufficient potential being applied, meaning that the droplet only falls after sufficient charge build-up has occurred. In any case, this is not a reliable mode of printing. Finally, Figure 3.7d represents a situation where excessive potential is applied or the flow rate is too great, resulting in a massive flow of ink being deposited. This is counterproductive to the goal of achieving high and consistent resolution.

A good test solvent for calibration of the EHD printing system is triethylene glycol monomethyl ether (TGME). It is a non-volatile, non-toxic solvent with a suitable viscosity, conductivity and surface tension for printing purposes. It is water soluble, and miscible with a whole host of other organic solvents. With this solvent, I performed a few tests to understand what happens to printing quality (printing results in **Figure 3.8a**) when you have;

i. Fixed speed and standoff height, varying potential (**Figure 3.8b**)
ii. Fixed standoff height and potential, varying speed (**Figure 3.8c**)
iii. Fixed speed and potential, varying standoff height (**Figure 3.8d**)

Caveat: this experiment is very much solvent specific. The results obtained help for the optimization of the process, depending on the ink being used. Each new ink has to be tested in the same way. There is, however, an easy way to circumvent this for similar inks, as I will demonstrate later in this chapter. This type of testing is commonly found in literature.[198] The printing was performed on 10 x 10 mm silicon wafers with 300 nm silicon dioxide. Five sets of surfaces were printed on; untreated surface, piranha acid treated, (3-aminopropyl)triethoxysilane (APTES) treated, POTS treated and trimethyloctadecylsilane (TMODS) treated. The monolayers were grown from 10 mM solution in toluene over a period of 24 hours.

[4] Distinguished from purposeful drop-on-demand deposition. This will be explained in another part of the thesis.

3.6.2.1. Fixed speed and height, varying potential

The result of these conditions is the variation of the deposition rate and volume. This results in a large variation of printing width, from coalescent printing to intermittent dotting. As the applied potential increases, I observed a widening of the printed line width (Figure 3.8b).

3.6.2.2. Fixed height and potential, varying speed

Having found a good height (~300 μm) which allows for the right electric field strength which promotes continuous jetting, I varied the speed of the substrate. This condition affects the deposition pattern. Too slow, and one could obtain bulging. Too fast, and I could observe disconnected patterns being printed. However, with an increase of speed, you also obtain a much decreased line width (**Figure 3.8c**). The trend is exhibited on all the surfaces tested.

3.6.2.3. Fixed speed and potential, varying height

This set of conditions mostly affects the jetting frequency and the jet diameter. As the electric field strength varies with increasing standoff height, the electric stress on the meniscus decreases, resulting in longer charge build-up time, which leads to the scenario depicted in **Figure 3.7c**. **Figure 3.8d** does not give an overall clear trend, but from the untreated surface, I find that as the height is increased, the line width decreases. This is primarily due to a reduced volume of ink being printed as the electric stresses applied become weaker.

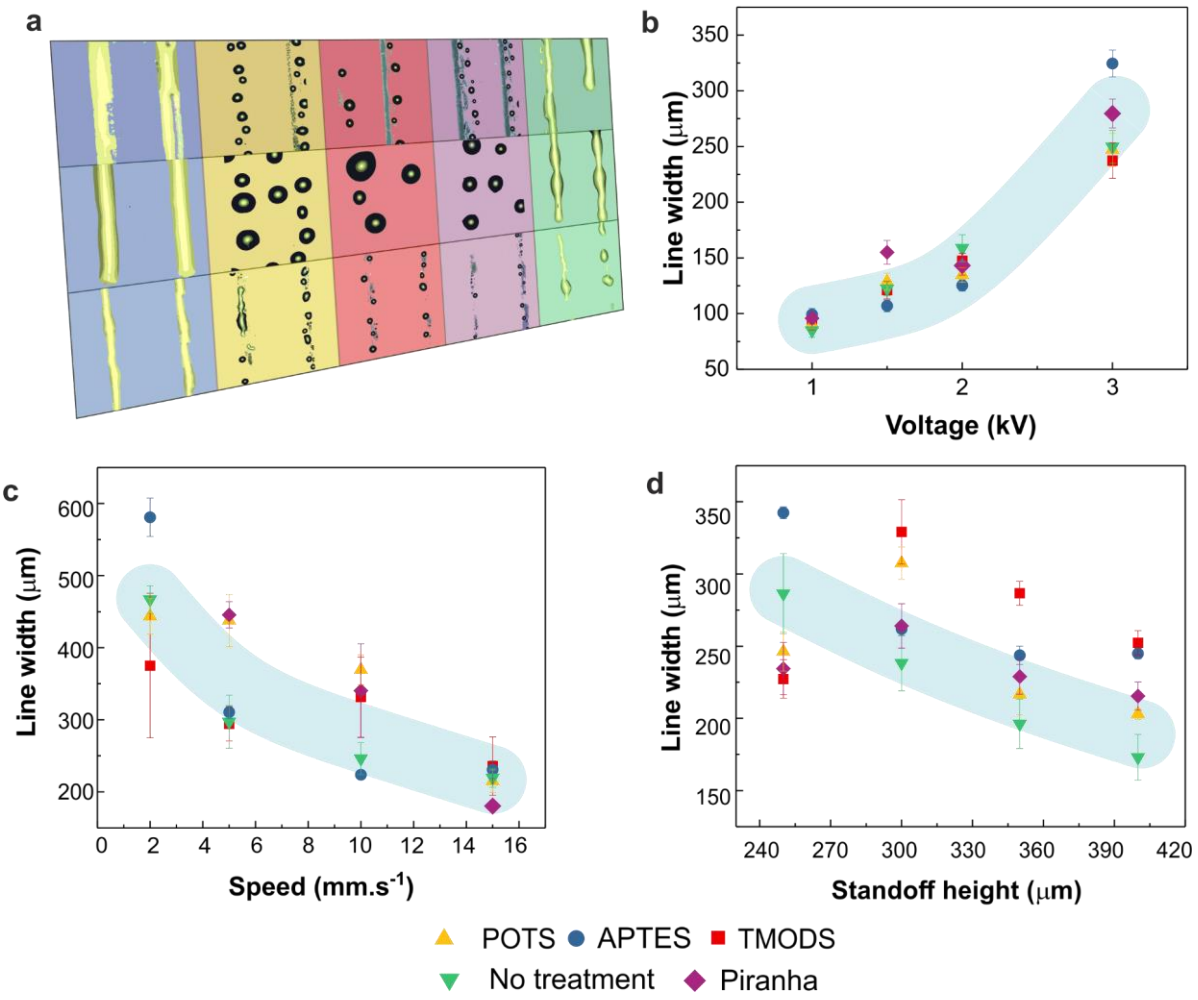

Figure 3.8. Variable tests on printing width. Plots of line width with a two variables fixed and one varied. a) Snapshots of the different patterns obtained during printing on the various treated surfaces with b) Fixed height and speed, varying voltage. c) Fixed height and voltage, varying speed. d) Fixed speed and voltage, varying height. The trends which emerge from these results allowed for better experimental design in this work.

From these results, a wealth of information is obtained. Firstly, the wettability of the surface printed on is of significant importance. Looking at Figure 3.8a, each coloured surface is representative of different surface treatments, as indicated by the figure key. The POTS and TMODS coated surfaces are hydrophobic, whereas the untreated, piranha acid cleaned and APTES treated surface are more hydrophilic. As TGME is a polar molecule due to the presence of the hydroxyl groups, it does not easily wet the hydrophobic surfaces, leading to significant discontinuities in the printing due to the high surface energy. On the hydrophilic surfaces however, better printing is obtained, irrespective of the controlled variable.

When the height and speed of printing are kept constant, but the voltage is increased, an increase in the line width of printed structures is obtained. This was determined to be linear for all surface treatments, except the APTES treated surface. It is unclear why the APTES surface exhibited this behaviour. However, the general trend of a line width increase is consistent with theory, in that with a greater electrical stress being applied, more material is deposited. Therefore, in order then to achieve high resolution, only the minimum voltage required must be applied during printing.

When the height and applied voltage are kept the same, with only speed increased, a decrease in the printed line width is observed. Care must be taken in the pursuit of high resolution, however, as if a threshold speed is reached, the continuous line printing will devolve into drop-by-drop deposition owing to excessive substrate speed. This is readily observed on the hydrophobic and piranha treated silica substrates used in this study. The line width decrease is a result of less material being deposited on a given area per time unit. This means that various line widths can be printed as desired by controlling the speed. From Figure 3.8c, looking at the APTES treated surface, a 7.5-fold increase in speed leads to an almost 3 times reduction in the line width.

Finally, when keeping the speed and voltage constant, whilst increasing stand-off height, only the untreated surface exhibits linearly decreasing line width. The other surfaces display quite mixed line width relationships. The biggest influence on this is that as the stand-off height changes, the electric field strength decreases quite sharply. With insufficient electrical stress, very weak jetting will occur, thus reducing the line width or causing the printing to be highly inconsistent.

Finite element modelling simulations provide invaluable insight into the physics at playing during the printing process. Here, I demonstrate with a model what happens to the electrostatic potential for a 500 nm tip held 1 μm above a conductive substrate (**Figure 3.9a**), and demonstrate how the field changes as the stand-off height increases (**Figure 3.9b**).

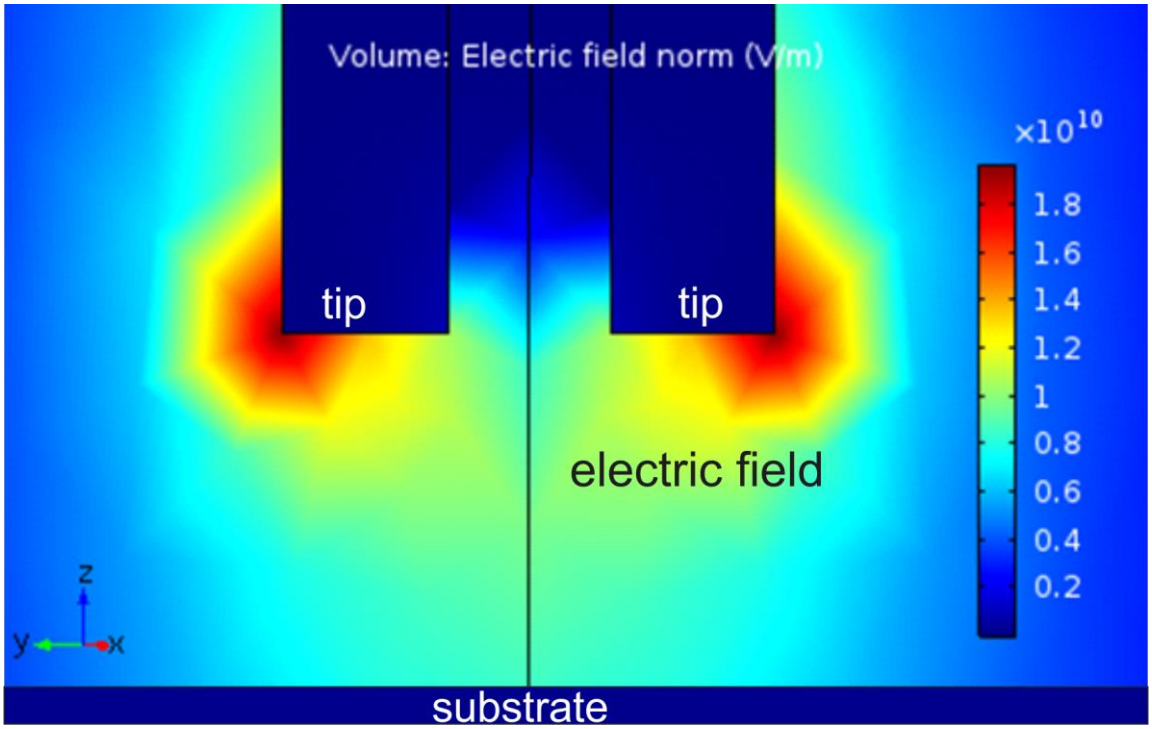

Figure 3.9. Model of conductive tip (with no ink). a) This model demonstrates the electric field distribution when a voltage of 10 kV is applied to a conductive tip held 1 µm above a grounded substrate. Numerical modelling allows for a global assessment of the field strength.

This model allows the understanding of several important points, which I explain below. Firstly, the electric field will be strongest concentrate on the tip edges (however small they are). Thus, any breakages of the tip (which are very common) would result in a redistribution of the electric field, skewing the jetting. Secondly, if a symmetric field did exist, it would be beneficial to have the meniscus of the liquid remain within the confines of the inner radius. Any spread of the meniscus would lead to even further reduction of the electric field, thus reducing the electrostatic force applied. This would lead to a higher applied voltage than necessary being used to induce EHD printing. Thirdly, referring to a point mentioned earlier, the massive potential difference between the tip and substrate is more than likely to cause dielectric breakdown (of the air) when no ink is flowing. Since, during tip metallization, the gold does not enter the tip, meaning that there is no electrical contact, charge would be forced to make its way to ground without causing any printing. These three points proved to be important inferences during the course of this work.

3.6.3. Mathematical treatment

It is prudent at this point to introduce some very simplistic equations which will guide the implementation of the EHD printing. Rigorous mathematical treatments for EHD have been reported in numerous articles and reviews[57], most notably in the initial paper by Taylor[100], as well as seminal paper by Jaworek *et al.*[55]

As mentioned in Chapter 2, the criterion for EHD printing to occur is that the surface tension be overcome by the electric stress. Simplistically, this can be explained with **Equation 3.1**.

$$F_\gamma \leq F_E \qquad \text{(Equation 3.1)}$$

The surface tension is a product of the surface tension coefficient, *γ* and the length over which it acts, *L*. For a circular tip, this length is ideally the inner circumference, 2*πr*. Also, if we treat the electrostatic force between the tip and ground as being capacitive, we obtain **Equation 3.2**:

$$2\gamma\pi r = \frac{\varepsilon_o A V^2}{2d^2} \qquad \text{(Equation 3.2)}$$

Where *γ* is the surface tension coefficient of the ink, in N/m, *L* is the distance over which surface tension applies (in this case circumference of the pipette), *A* is the area over which the tip exerts a force (treating it as a capacitor and assuming uniform electric field distribution), *V* is the applied potential, and *d* is the standoff height. Rearranging for *V*, and simplifying the argument, **Equation 3.3** emerges.

$$V = 2d\sqrt{\frac{\gamma}{\varepsilon_0 r}} \qquad \text{(Equation 3.3)}$$

Again, this treatment is a very unsophisticated one, meant to give an estimate of what kind of potential is needed for inks of a specific surface tension for a capillary of fixed radius, *r*. Using commercially available organic solvents and their surface tension values[199], for a capillary of fixed radius, the following is observed (**Figure 3.10**).

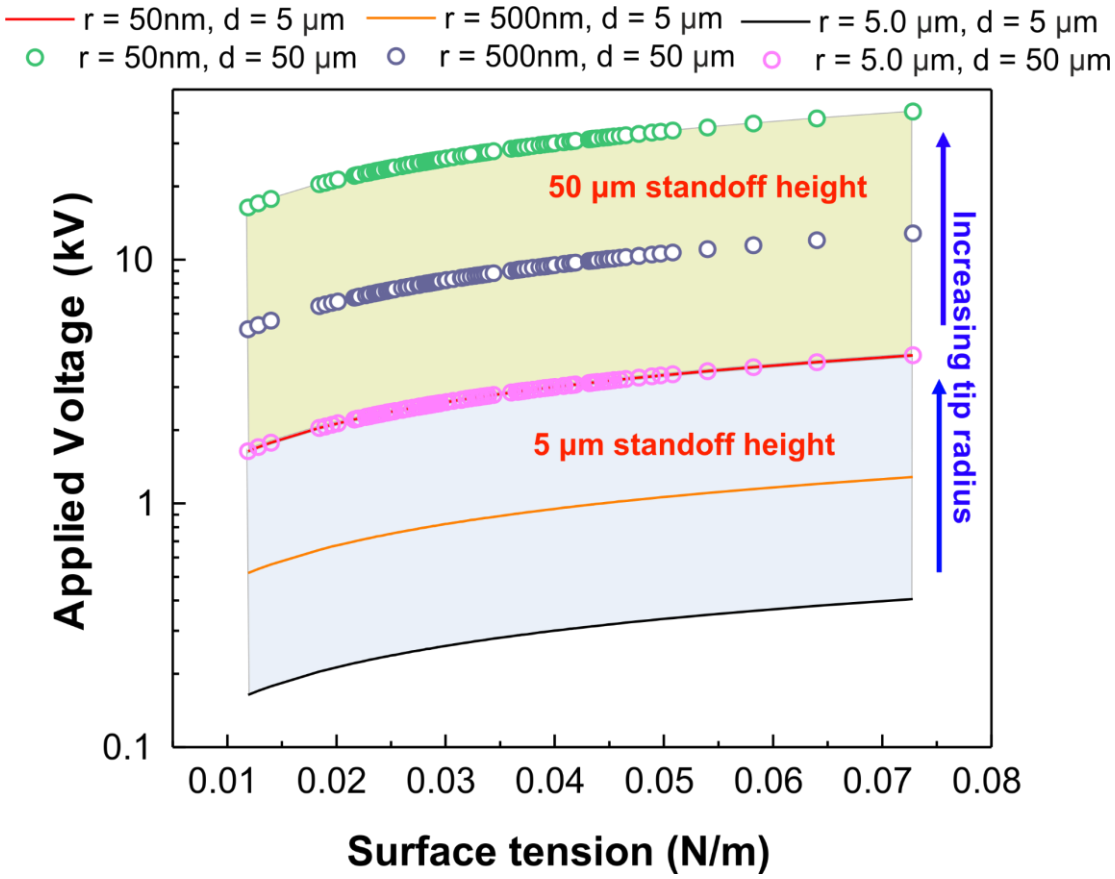

Figure 3.10. Potential required to induce EHD printing as function of surface tension. Using the surface tension of commercial solvents, and Equation 3.3, this figure illustrates the relationship between potential and surface tension, for 50 nm, 500 nm and 5 µm radius tips at standoff heights, *d*, of 5 (blue region) and 50 µm (olive region) respectively. The applied potential is increased by a factor of 10 between the 5 and 50 µm stand-off heights, for tips of the same size.

The applied potential increases nonlinearly as a function of the surface tension. The greater contributor to reducing the potential required is using a larger tip or a smaller stand-off height. This data further indicates that the initial printing I performed was hampered by the fact that my stand-off height was too large for the size of capillary I used at the time. The capability to predict what kind of applied potential is required gives more confidence to being able to print

successfully. When Equation 3.3 is used to determine the electric field required for printing, as function of tip radius (and fixed surface tension), as was done with Equation 2.6, a similar logarithmic relationship is observed. The actual values vary due to each equation being used to solve for different variable. The electric field is determined directly with Equation 2.6, whereas the applied potential determined in Equation 3.3 is then used to determine the electric field.

3.7. Conclusions

In this chapter, I have introduced the home-built EHD setup used in this thesis. I have shown some of the earlier printing attempts which were not successful, and provided an explanation as to why that was the case. Using better ink loading techniques such as micropipette loaders aided in reducing the number of unsuccessful printing trials. The coating of the tip nozzle with self-assembled monolayers contributes to minimizing the meniscus size, thus promoting printing at lower applied voltages. Using equations found in literature, I have shown how the electric field strength needed to induce printing is logarithmically related to the capillary size. This aids in the process of deciding what size tip to use, depending on the maximum field a system can generate. I have explained how changing different system parameters contributes to the printing quality, and named the four main observed printing regimes. Optimizing the printing speed, stand-off height and applied potential are crucial to achieve consistent, reliable printing. I further demonstrated this when coupled with substrates which have been treated in order to control their wetting. Depending on the polarity of the solvent used, an appropriate surface treatment must be used. Extremely hydrophobic surfaces cause polar solvents such as TGME to form inconsistent dots owing to the high surface energy they impart. The more hydrophilic APTES was surprisingly better able to contribute towards reliable printing. Finally, equations have been derived which aid in the streamlining of the optimization process. By knowing the surface tension and stand-off height and tip radius, it is possible to generate an estimate of what kind of applied potential is required to induce EHD printing.

The knowledge acquired and experience gained in this chapter is crucial in the following chapters. As I demonstrate in chapter 4, high resolution printing is achievable by adjust certain printing parameters. In chapter 5, I investigate the influence of the electric field on the self-assembled monolayers used to control surface wetting properties. Finally in chapter 6, I demonstrate a functional sensor printed with colloidal polyaniline.

3.8. Author contributions

The EHD printer used in this work was originally put together by Dr Daniel Engstrom (Loughborough University). It was modified by Dr Benjamin Porter and myself. All experiments performed to calibrate the instrument were performed by me. I thank Professor Steve Morris (Department of Engineering, Oxford) for the idea of using PM-597 in the early experiments. The coating of capillaries was done in the Department of Physics Denys Wilkes Building cleanroom.

Chapter 4

Self-assembled monolayer printing: Process, metrology and applications

Work presented in this chapter was published in:

Benjamin F. Porter, Nhlakanipho Mkhize and Harish Bhaskaran, "*Nanoparticle assembly enabled by EHD-printed monolayers*", Nature Microsystems and Nanoengineering 3, 17054 (2017), DOI: 10.1038/micronano.2017.54

4.1.1. Introduction

Many inks have been developed in the past few years in order to achieve specific applications, ranging from organic electronics to biological sensing. The most common inks found in the realm of EHD printing are nanoparticle based inks which allow for the printing of conductive elements or electrodes. This has relied on the direct printing afforded by EHD, and is followed quickly usually by sintering to achieve metallic contacts. Less observed, is the direct patterning of a template layer for further processing. In this chapter, I introduce this novel concept.

Whitesides *et al*. introduced in their work a novel way to achieve the functionalization of surfaces.[22,200] By developing micro-contact printing, they achieved the ability to pattern surfaces with self-assembled monolayers with great resolution. However, their methodology required the manufacturing of micro-moulds using polydimethylsiloxane (PDMS). This is time consuming, and wasteful as the PDMS can then not be melted down or recycled for any other purpose than that which it was moulded for. Direct printing of these molecular templates is the more versatile option due to the flexibility it affords, as is necessary to develop additive nanomanufacturing techniques. The high electric fields utilised in EHD enable it to overcome the strong capillary forces found in narrower printing nozzles that limit the resolution of more conventional ink-jet printing. EHD printing should also be capable of depositing inks of solvated monolayer compounds for the self-assembly of molecular monolayers, which would allow the integration of this additive manufacturing process with bottom-up assembly of nanoparticles (drop-cast method).

EHD jet printing affords the opportunity to pattern these SAM molecules precisely without the need for any templates or moulds. In this chapter, I specifically discuss the patterning of 3-(aminopropyl)triethoxysilane (APTES) for further functionalization with gold nanoparticles. The electrostatic interaction between the free nitrogen of the amino group and the gold nanoparticle allows this functionalization to be possible[201] (**Figure 4.1**).

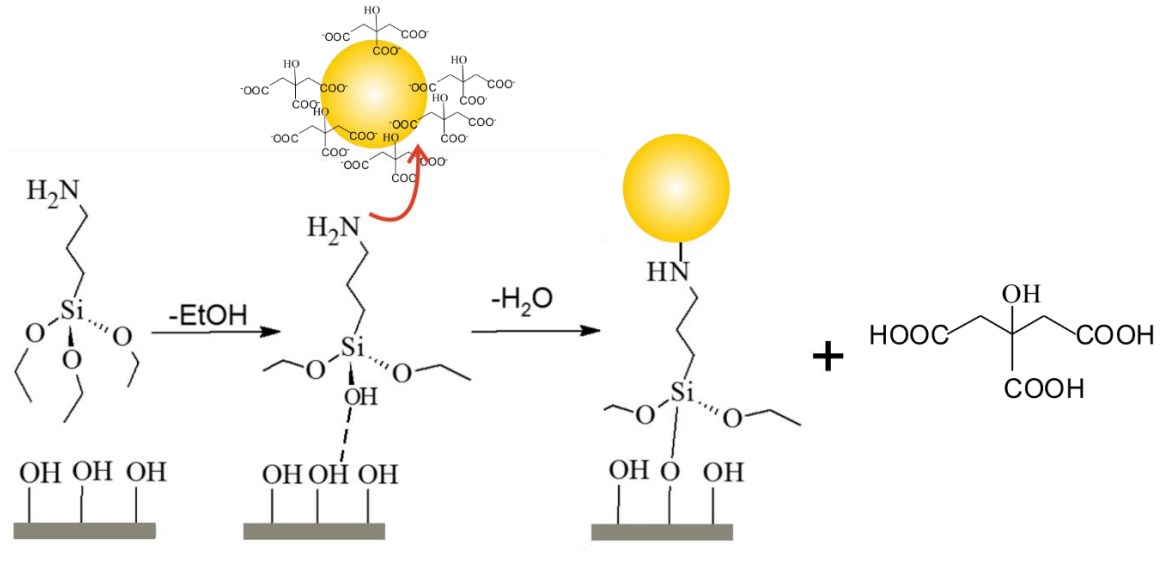

Figure 4.1: Schematic of citrate capped gold nanoparticle interaction with (3-aminopropyl)triethoxysilane. The electrostatic interaction between gold nanoparticle and the amino group drives this interaction.

4.1.2. Aims of chapter

- Demonstrate use of EHD printing as novel printing technique for self-assembled monolayers as templates for further functionalization
- A brief discussion on the achievable applications with this process

4.2. Method and Materials

4.2.1. EHD printing of APTES

Surfaces for printing were prepared on 100 nm thick, thermally grown SiO_2. These surfaces were prepared for adhesion of the monolayer by pre-cleaning in piranha solution (H_2SO_4:H_2O_2, 3:1). This was performed at 120 °C for 30 minutes to allow for full hydroxylation of the silica surface, followed by 10 minutes rinsing in hot deionised water and drying with a stream of N_2 gas. The inks were prepared by sonication for 15 minutes of APTES to allow full solvation into the given solvent of either water, ethanol, IPA or triethylene glycol monomethyl ether (TGME). EHD printing nozzles were prepared per the method described in Chapter 3. Nozzles were then immersed in a 5 mM solution of 1*H*,1*H*,2*H*,2*H*-perfluorodecanethiol to make the outer Au

surface hydrophobic. The ink was then injected into the pipette using micro-loading pipettes. The loaded capillary was then lowered to a 100 µm distance from the printing surface observed via a microscope. A voltage of 2 to 5 kV was applied between the capillary and the ground plate to induce the printing (**Figure 4.2**).

4.2.2. Nanoparticle assembly

A 500 µL droplet of 20 nm citrate capped gold nanoparticle colloid was deposited onto each chip. The spontaneous assembly was allowed to proceed for 8 minutes, with the chips protected with a glass petri dish.[202] After assembly, the chips were sequentially rinsed twice in fresh deionized water for 30 s each, and then in clean IPA. They were then dried using a N_2 gas stream, and stored appropriately.

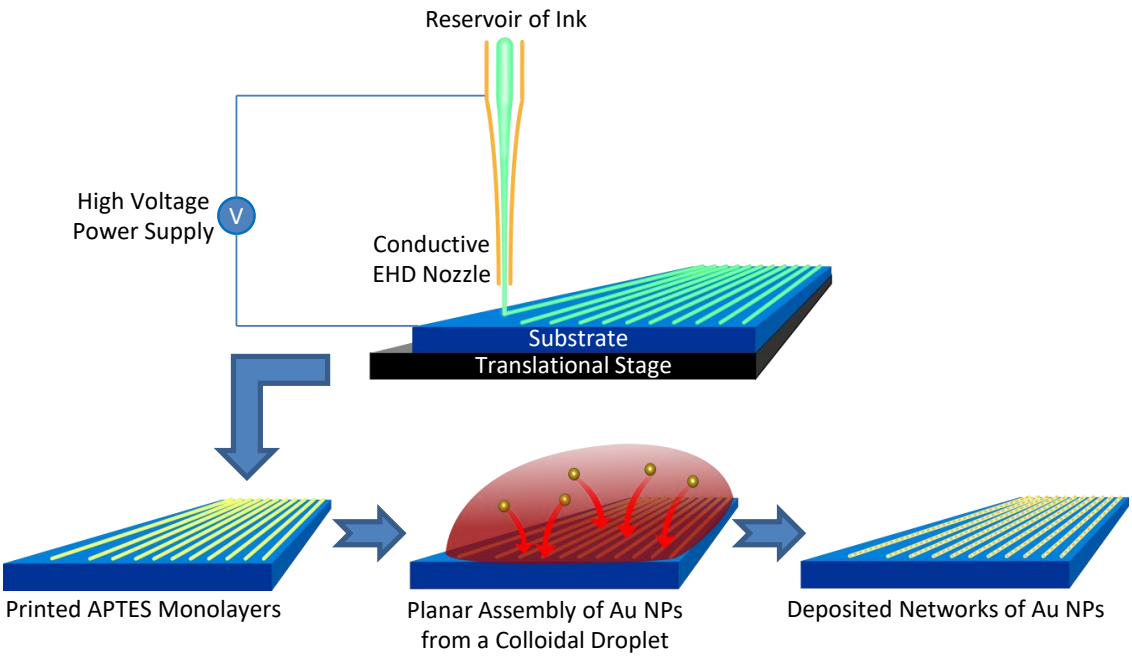

Figure 4.2. Schematic of monolayer printing. The conductive nozzle is held at a fixed standoff height above the grounded substrate and a potential is applied to induce printing. After printing the SAM ink, a solution of nanoparticles is drop-cast and assembly takes place spontaneously. The excess Au solution is rinsed off with water and IPA to give the final array.

4.3. Sample characterisation

AFM scans were performed using an Asylum MFP-3D AFM with 81.2 kHz silicon PPP-FMR Nanosensors AFM probes. Scanning Electron Microscopy was performed with a Jeol 6500F SEM at 10 kV.

4.4. Results

The inks for printing were prepared by diluting APTES, the compound for functionalization of the surface, with desired solvents by ultra-sonication for 15 minutes. With ethanol, propan-2-ol (IPA) or aqueous solvents, the results were mixed; jetting of the ink was not achievable with the more hydrophilic ethanol and aqueous inks. With IPA as the solvent, the results most closely corresponding to a monolayer were achieved with a solution printed from a 5 mM solution of APTES, at a 5 kV bias, a scanning speed of 0.5 mm/s and a capillary-surface distance of 100 µm. Once printed onto the surface, the surface was conditioned for 12 hours in a humid environment to allow the monolayer to grow more effectively across the surface, and then cleaned by sonication in IPA and a subsequent sonication in deionised water. An AFM scan of the results of this is presented in **Figure 4.3a**, showing this formed a very rough, porous surface of APTES with a thickness of up to 5.6 nm at the boundaries (**Figure 4.3c**).

The most effective solvent for EHD printing of APTES utilised in these experiments was triethylene glycol monomethyl ether (TGME). A solution of 100 mM APTES in TGME was printed at a 2 kV bias, a scanning speed of 0.5 mm/s and a capillary-surface distance of 50 µm. It must be noted here that a 100 mM solution is very concentrated. Normally, SAM assembly is performed with very dilute concentrations (< 10 mM). This is due to the propensity of SAM molecules to form bi- or multilayers when in greater concentration, and especially when there is moisture present. 15 minutes after printing the surface was rinsed by sonication in IPA and a subsequent sonication in deionised water. An AFM topography measurement of this print can be seen in Figure 4.3b, indicating that across an approximately 50 µm wide area, a thin film of APTES has formed on the surface. The spreading and drying of the droplet on the surface appears to have formed two separate areas of APTES of varying width at either

edge of the printed line. Optical observations of the surface indicated that this was a result of how the solvent spread on the printing surface, and is not an indication of poor dissolution of the APTES leading to Marangoni flow of dispersed particulates (the coffee ring effect). Paradoxically, SAMs are more commonly used to control the wetting of surfaces. In this instance, there is no surface modification to prevent solvent wetting, hence the spreading of the printed lines being so much more pronounced.

Table 4.2. Solvent properties. The solvent properties play an important role in the printability of the ink, as well as the SAM growth dynamics.

Solvent	**Electrical conductivity (S/m)[a]**	**Surface Tension at 22.3 °C (mN/m)**
Acetone	5.0×10^{-9}	22.1
Isopropanol (IPA)	6.0×10^{-8}	21.3
Triethylene glycol monomethyl ether (TGME)	1.0×10^{-8}	38.8
Ethanol	1.4×10^{-9}	22.3[b]

[a] Due to limited measuring range of my instrument, literature values used. [203]

[b] Value obtained from literature [203]

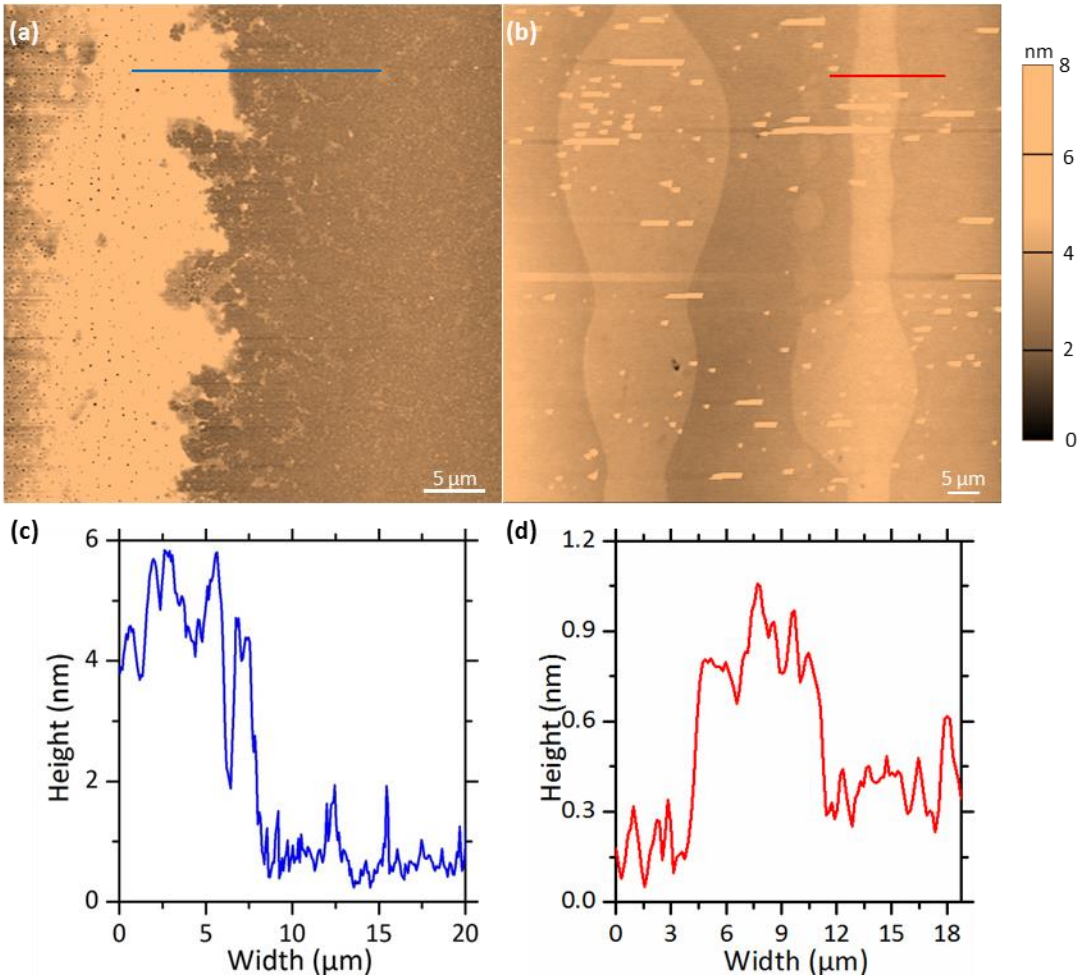

Figure 4.3. AFM measurements of EHD printed APTES films. Topography of films EHD printed with APTES from solvents of (a) IPA and (b) TGME. The features in (a) appear to have crystallised and formed relatively large agglomerates in comparison to the features in (b) which have formed smoother, semi-continuous films. (c, d) lines profiles of the topography corresponding to the blue lines in (a) and (b) respectively. This shows that an APTES coating was more consistent and more closely approached that of a monolayer for the TGME ink than for the IPA ink.

Once printed the functionality of the APTES surfaces was tested to see if electrostatic self-assembly of gold nanoparticles would still occur. After 8 minutes of assembly of 20 nm Au particles from a droplet deposited on the surface, the surfaces were imaged using scanning electron microscopy (SEM), the results of which are presented in **Figure 4.4**. With IPA ink (**Figure 4.4a, b**), it is apparent that the nanoparticles have assembled onto all surfaces across

the SiO_2, regardless of where the EHD printing appeared to have deposited the APTES-IPA ink. This may be due to the formation of a volatile gas phase of APTES that then spread to surrounding oxide surface, resulting in the assembly of nanoparticles onto these surfaces as well. The TGME-APTES ink on the other hand (**Figure 4.4 c, d**) produced excellent results. Au nanoparticles are clearly seen to assemble densely on the printed APTES surface and are largely repelled from the uncoated silica surface. The nanoparticles that are present on the repulsive surface may have resulted from random instability or a smaller degree of spreading of APTES in the gas phase as may have been the case with the IPA-APTES ink.[204] Such process variations are to be expected and further investigated to develop fully characterized nanomanufacturing processes.

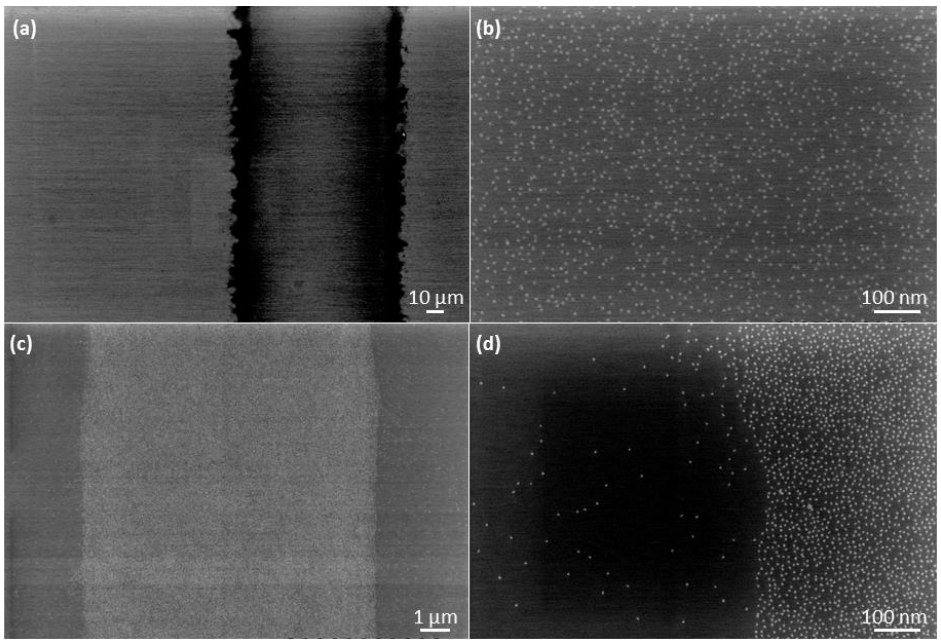

Figure 4.4. Au Nanoparticles assembled on EHD printed APTES**.** SEM images of 20 nm Au particles assembled onto EHD printed APTES surfaces, where APTES was solvated in(a, b) propan-2-ol and (c, d) TGME. (a) The propanol-APTES ink has formed a 100 µm wide band across the surface. (b) Au particles have been deposited across the surface, indicating that the ink may have spread during growth causing APTES to be deposited across the surface. (c) The TGME-APTES ink has formed a 10 µm wide band across the surface. In this case the Au nanoparticles have assembled densely onto the APTES-printed area, (d) with a few particles adhering to the repulsive silica surface.

To achieve a higher resolution, a velocity profile test was implemented at a constant tip-surface voltage of 7 kV. Once a jet had been established, the printing stage was moved with respect to the EHD-nozzle over a 75 µm distance which, based on the acceleration profile of the DC motor stage, would have achieved an upper velocity of 3.8 mm/s. One such printed profile is observed optically in **Figure 4.5c**, after nanoparticle assembly has occurred, with the narrowest section present at the centre of the printed line. At this speed, the EHD has produced a finer jet onto the surface; closer investigation with AFM (**Figure 4.5d**) confirms a width of ~ 300 nm. Although the stability of this printing resolution could not be maintained across a larger scale, it is clear from these results that EHD printing is capable of writing templates of functional APTES with nanoscale resolution. More stable printing results are likely to be achieved through controlled printing of droplets using pulsed deposition.[63,205]

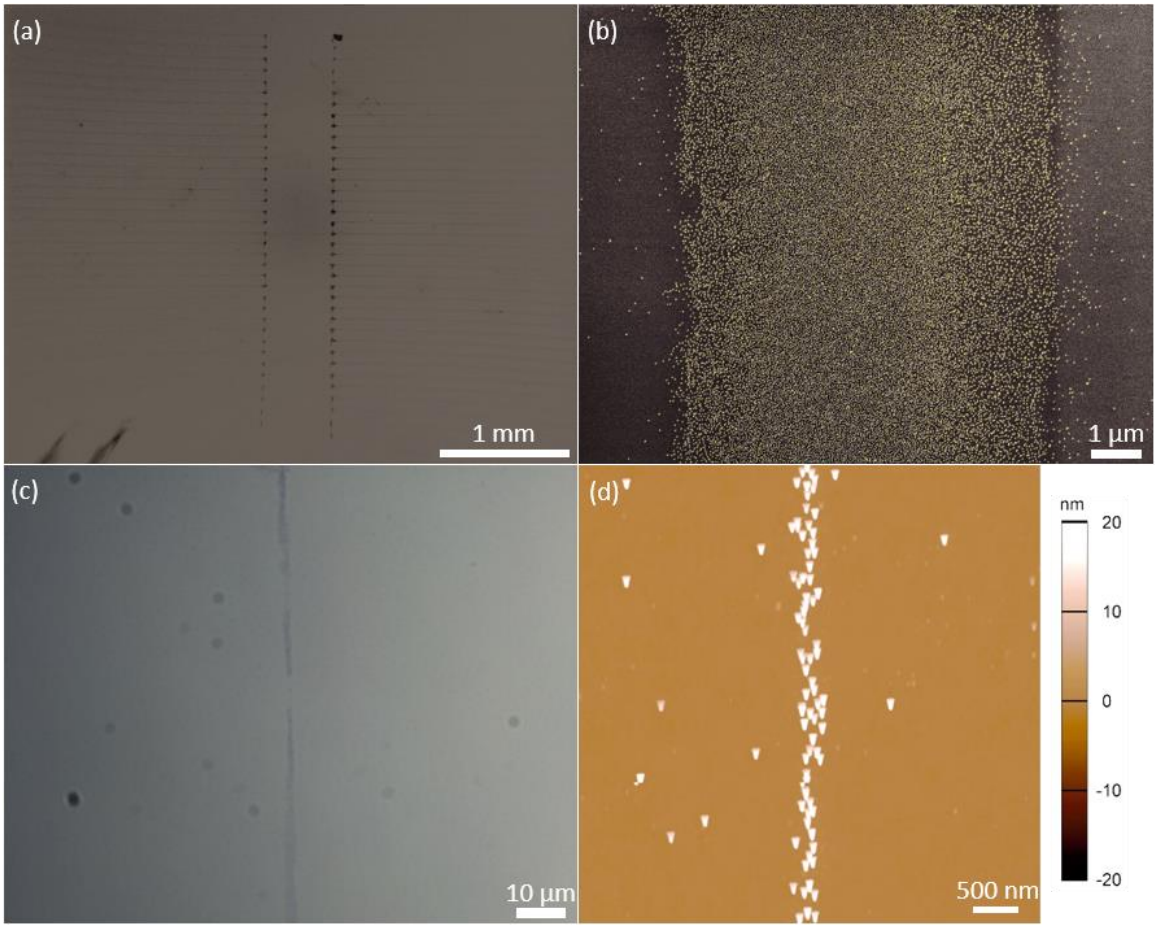

Figure 4.5. Au Nanoparticles assembled on electrohydrodynamic (EHD) printed (3-aminopropyl)triethoxysilane (APTES). (a and b) Scanning electron microscopic (SEM) images of 20 nm Au particles assembled onto EHD printed APTES arrays of monolayers. (a) Two large arrays of Au nanoparticles on APTES deposited during a raster scan with 75 µm pitch between each consecutive line. (b) A close-up image of one of the printed lines in a, showing nanoparticles assembled densely onto a 7 µm wide band of APTES. (c) An optical microscope image of nanoparticles assembled onto a band of APTES that was printed with a velocity gradient, with the narrowest region formed at the peak (3.8mm/s) at the centre. (d) An AFM topography image of the nanoparticles assembled onto the narrowest section in c, with nanoparticles assembled onto a ~300 nm wide band of APTES on the silica surface. No back-pressure was used in this printing.

To observe whether the assembly of the nanoparticles to APTES could be achieved in solution before printed was performed, a test solution was made. A dilute solution of APTES was added directly to a vial with dilute Au nanoparticle suspension. Within a matter of minutes, the solution change colour from red to almost blue (**Figure 4.6 a,b**). This change of colour can be explained by the fact that nanoparticles aggregate within the solution as the citrate capping layer is displaced. The UV/Vis spectra (**Figure 4.6c**) confirm the redshift and as a result of the aggregation. This demonstrates that it is better to perform nanoparticle assembly after the printing of the self-assembled monolayer.

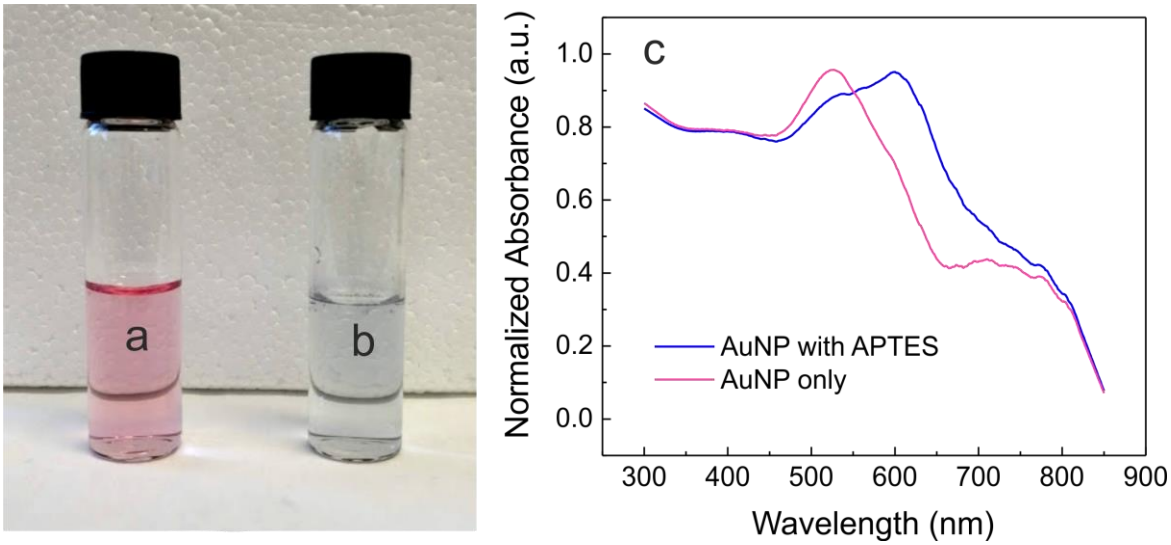

Figure 4.6. Photograph of AuNP suspensions. Well dispersed AuNPs, as in a) exhibit a reddish colour. With the addition of the destabilizing APTES in b), this colour changes immediately to a pale blue owing to aggregation of nanoparticles in the suspension. c) UV/Vis of the suspensions spectroscopically confirms the colour change. The red-shift observed with APTES in solution is indicative of larger particles forming.

4.5. Discussion and future work

The SiO_2 combined with direct EHD printing of the APTES monolayer is clearly effective at enabling the direct deposition of devices for nanoparticle assembly. Although this results in a planar geometry, it does enable the additive manufacture of the features in a single-step process, making it more desirable for development. Microscale EHD printing of APTES was

achieved reliably with rapid patterning, though the nanoscale patterning was more difficult to maintain over the larger areas, as EHD modes would revert to different modes of spraying at higher print speeds.[55] Developing a reliable nanoscale resolution printer for manufacturing may rely on the NanoDrip method of EHD, which has shown a limited printing velocity of 1 - 10 μm/s for 500 nm metal networks.[39] This would have a hugely detrimental impact on the patterning time, whereas the 3 - 4 mm/s demonstrated in this work compares favourably to the upper speeds of 10 mm/s utilized in electron-beam lithography.[206] The use of emerging methods of EHD printing, such as combinations with AFM-capillaries for closed-loop nanoscale nozzle-surface separation[207,208], would greatly improve the resolution I demonstrate here for continuous printing. This could be used to directly print far denser networks of nanoparticles, opening a route for the use of additive nanomanufacturing to create single electron device circuitry[209], sensors[210,211], catalysts[212] and nanoplasmonic devices.[213]

Nanoparticles can also be positioned through this process to enable the assembly of other components, such as the positioning of optoelectronic components.[214] All these capabilities could be integrated with existing devices through this additive fabrication method. Directly printing onto existing devices to add nanomaterial functionalities would be highly enabling to completely blend electrical, optical and biochemical components. For instance, printing sensors directly onto circuits, machinery or medical devices could greatly enhance their functionality. Further refinement of this manufacturing methodology would be able to achieve the sub-50 nm patterning of functional molecules EHD printing is capable of, but the goal of this work is to show that combined processes work just as well as established lithography, and thus need to be considered a serious alternative.

4.6. Chapter summary

I have provided a broad scope of the opportunities currently available to integrate high-resolution assembly of nanoparticles, using EHD to achieve rudimentary additive nanomanufacturing. Crucially I have demonstrated two key advances: firstly, printing molecular monolayers with EHD; and secondly such printed monolayers can afterward be used to self-assemble nanoparticles onto a surface. I achieve this through the use of a TGME-APTES ink and EHD printing. The printed monolayers were then able to electrostatically self-assemble Au nanoparticles onto these selectively printed surfaces. This approach to manufacturing has great potential to effectively integrate electrical, optical and biochemical components to produce devices with enhanced functionalities, which is in line with the goal of making rapid prototyping more accessible.

4.7. Author contributions

Dr Benjamin Porter performed SEM and AFM characterization. I performed the substrate and ink preparation, printing experiments and UV/Vis spectroscopy.

Chapter 5

Chemical and mechanical means of controlling surface wettability

5.1. Introduction

As I have demonstrated in chapter 3, and highlighted from literature, self-assembled monolayers (SAMs) are commonly used to chemically modify the wetting properties of surfaces. In the first part of this chapter, I explore with the aid of Kelvin probe force microscopy and computational modelling the influence of electric fields on the physical properties of the SAMs. In the second part, I demonstrate promising preliminary results of using mechanically induced surface wrinkles to control wettability, and hence the resolution of printing with EHD.

5.1.1. Chemical control in the presence of electric fields

Self-assembled monolayers (SAMs) freely form 2-D structures on metal and oxide surfaces, amongst others.[215,216] These functional molecular layers are used to control the wetting properties of surfaces, which is of importance for a variety of applications, including printing. The terminal group of the SAM (**Figure 5.1a**) is responsible for this surface energy modification. Lowering the surface energy results in reduced wetting, whereas increasing the energy results in enhanced or complete wetting.[217] Long chain alkyl and fluorinated alkyl SAMs are known for giving the best hydrophobicity.[218] Alkyl SAMs are organic dielectric materials.[219–223] This property has been exploited in device manufacturing to modify Schottky barriers[224], to act as organic gates in transistors[225–230] and to modify organic photovoltaic cells.[231] Therefore, SAMs, whilst having excellent chemical and thermal stability, exhibit electrical breakdown behaviour in the presence of significant electric potentials which irreversibly changes their properties.[232] This can lead to poor performance in applications where their structural integrity is important. The pursuit of high resolution printing using electrohydrodynamic jet printing is one such area.

Thus far, the effect of electric fields (of the order of MV/m) generated during EHD on SAMs have not been studied. Previous studies, using innovative metal-SAM-metal configurations, have shown that the monolayer can undergo breakdown when exposed to sufficient electric potential[226,233] and a few theories as to the mechanistic contribution have been suggested. Haag *et al.* studied the electrical breakdown voltages of SAMs used as organic dielectrics in

a metal-dielectric-metal configuration (i.e. in contact).[226] They revealed that the monolayers are quite resilient to the external applied field depending on the substrate upon which they are grown and their chain length. To the best of my knowledge no studies have reported the behaviour of SAMs in the presence of high strength electric fields in a non-contact regime.

5.1.2. Aims of chapter

Whilst reporting breakdown values, existing studies have not demonstrated the overall macroscopic effect of a localized breakdown in the monolayer. Here, I determine the breakdown limit as well as the mechanism by which this breakdown occurs for three commonly used SAMs: 3-(aminopropyl)triethoxysilane (APTES), trimethoxyoctadecylsilane (TMODS) and perfluorooctadecyltriethoxysilane (POTS) by using conductive atomic force microscopy (C-AFM) (**Figure 5.1b**). I then measure the effect of exposing the SAMs to electric fields with Kelvin probe force microscopy (KPM). This is achieved by explicitly determining the work function of SAM coated surfaces before and after exposure to an electric field (Figure 5.1c). This, to the best of my knowledge, is the first time that KPM has been used to determine the influence of a static electric field on the chemico-structural integrity of self-assembled monolayers. KPM has, however, been used successfully elsewhere for the characterization of SAM modified surfaces.[234,235] To understand the macroscopic effect of electric field exposure, I employ contact angle measurements to determine the extent by which the wetting properties change, if at all.[236] This combination of KPM and contact angle measurements has been used before by Evans *et al.* to characterize monolayers formed by molecules modified with a chromophore in differing chain positions. They did not, however, study the influence of an electric field on the monolayer surfaces electrically. Lastly, I investigate the relationship between the SAM dipole moment and the measured work function both before and after field exposure. Computational modelling is also used to understand the field effect on the SAMs.

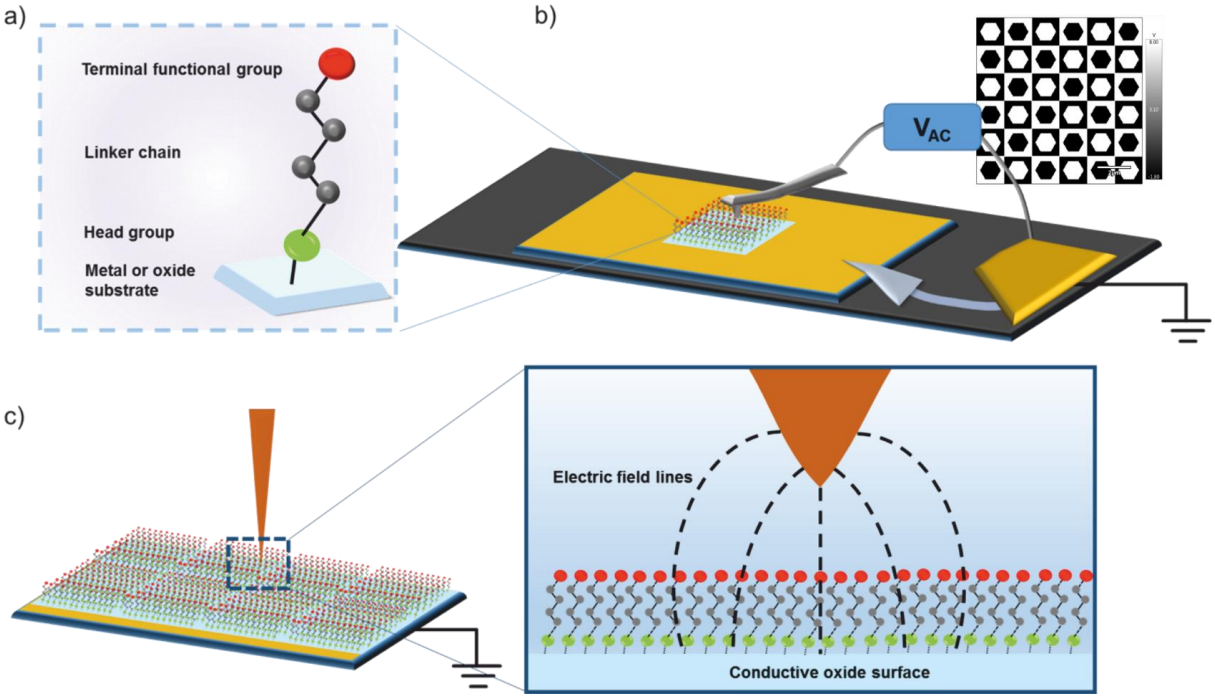

Figure 5.1. Experimental configuration for SAM investigation. (a) Schematic of a general self-assembled molecule showing the three main parts; terminal functional group, linker chain and head group. (b) Schematic of electrical AFM configuration used to determine the breakdown voltage of the self-assembled monolayers. [Inset] Binary image used to pattern the monolayers (c) Tungsten tip used to generate strong electric field over monolayer coated surface from a set distance.

5.2. Experiment setup

5.2.1. Materials

1H,1H,2H,2H-perfluorooctyltriethoxysilane (POTS), (3-aminopropyl)triethoxysilane (APTES), trimethoxyoctadecylsilane (TMODS), toluene, isopropanol, and acetone were purchased from Sigma Aldrich and used as received. Silicon wafers were purchased from Inseto (UK) limited. Indium tin oxide was obtained from the Thin Film Facility at the Department of Physics, Oxford. Tungsten probes used were obtained from Signatone.

5.2.2. Substrate preparation

A thin layer, 50 nm, of indium tin oxide (ITO) was sputtered photolithographically patterned squares, on 80 nm gold, on top of 100 nm thermally grown silicon dioxide on n-doped silicon (**Figure 5.2**). It was then cleaned by sonication in acetone and isopropanol. The substrates were then dried with a nitrogen gas stream. Immediately before monolayer growth, the substrates were treated with oxygen plasma (60 W, 2.5 min) in order to make the surface more reactive and to remove any residual organic contamination. All further characterization was performed in ambient conditions.

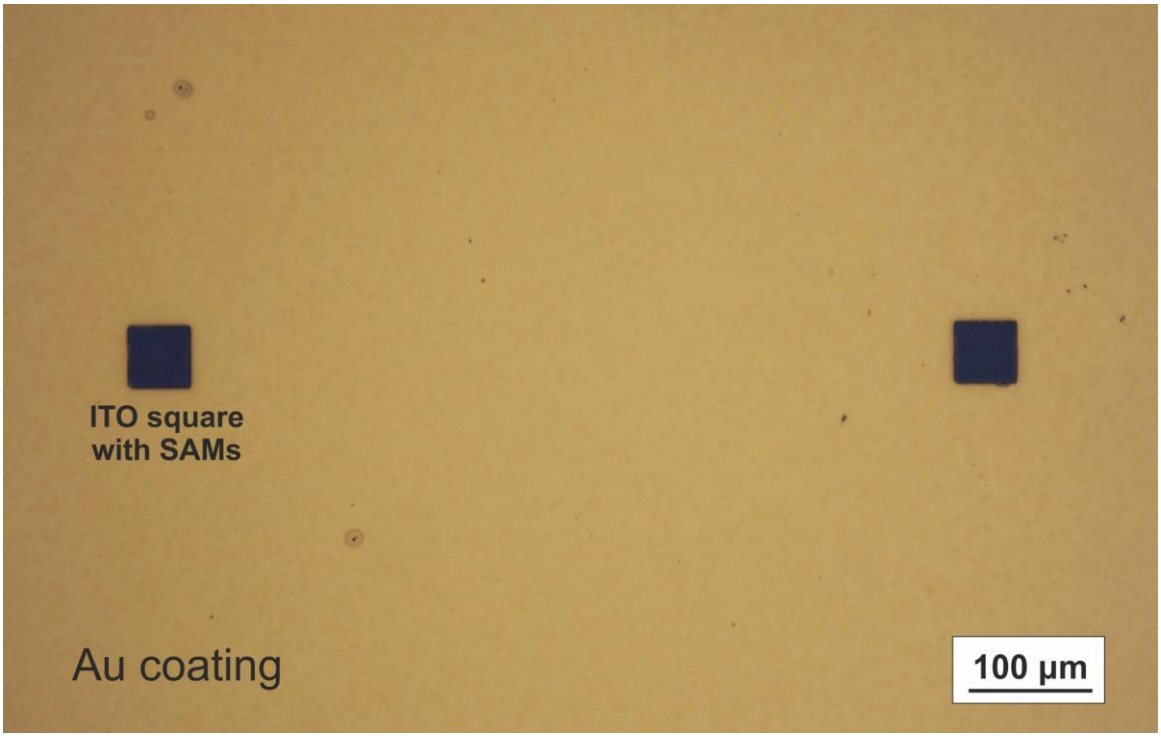

Figure 5.2. Indium tin oxide pads for monolayer growth. SAMs were grown on conductive ITO regions in order to assess their electrical character more accurately. Gold was used as a conductive layer beneath the ITO due to its poor affinity for SAM molecules.

The monolayers were grown from 10 mM solutions in toluene for a period of 24 h. Excess monolayer was removed by sonicating the substrates briefly in fresh toluene and isopropanol. It is worth noting that only the POTS surface came out of solution as being autophobic, i.e. not wet by the solution from which it was formed.[236]

5.2.3. Exposition to electric field

A tungsten needle with tip diameter of 5 μm was connected to a high voltage source whilst the substrate was grounded. The applied bias used was the maximum voltage reached before electric discharged was observed[5]. The needle was lowered to a fixed height whilst the substrate was translated on an X-Y stage (Physik Instrumente UK) at a speed of 1 mm/s.

5.3. Results

5.3.1. Monolayer growth

It is well understood that monolayer quality is affected by several factors including growth time, the solvent used, growth temperature, SAM concentration and substrate reactivity. In this work, all these factors were optimized. Silanzation of oxide surfaces is a well-studied process.[237] The best monolayers are obtained using vapour phase deposition[238], although liquid immersion yields good results too.[239] Kumar *et al.* found that longer chains provide better chemical protection to surfaces compared to shorter chains.[240] Also, hydrophobic tail groups do better in protection than hydrophilic tail groups. This could be attributed to the fact that long chain compounds form densely packed crystalline-like monolayers whereas shorter chains show greater disorder and less dense arrangements.[241] The choice of solvent from which growth will take place is also very important. One may be tempted to rely on the polarity index of a solvent in choosing it as a suitable carrier, but work by Manifar *et al.* [242] demonstrated that a few more factors come into play. They showed that the partial charge distribution, as well as the dipole moments of both solvent and solute must be considered to achieve the most optimal monolayer growth. The water content of the solvent is also a crucial consideration. High water content, especially where alkyloxysilanes are being used, can cause hydrolysis of the monolayers, thus leading to in situ polymerization of the SAMs, and thus aggregation. This was demonstrated by Rozlosnik *et al.* where they used solvents of varying water content levels.[243] Too much water leads to poor monolayer formation, whereas not

[5] Electric discharge is known to cause plasma induced damage to SAMs owing to the high energy density.

enough water results in no or extremely slow growth. Most studies make use of dry toluene, as it possesses sufficient water for hydrolysis to occur, whilst not being so water logged that it leads to SAM aggregates. In this work, dry toluene was used in ambient conditions, over a period of 24 hours to grow monolayers on freshly cleaned wafers.

5.3.2. Quality of monolayer growth

The quality of monolayer growth on the final set of samples was determined in part by the use of X-ray photoelectron spectroscopy (XPS). One silicon wafer modified with each SAM was studied, and three regions were analysed. The summarized results are shown in **Table 5.1**.

Table 5.1. Summary of XPS results. The atomic % of each wafer varies owing to the presence of a different self-assembled monolayer. The highlighted cell in each case denotes the distinguishing element (Fluorine for POTS, higher carbon count for TMODS and nitrogen for APTES). Other elements were detected too, but have been omitted for the sake of brevity. Their concentrations were negligible.

	Blank wafer		**APTES**		**TMODS**		**POTS**	
Name	Peak BE	Atomic %	Peak BE	Atomic %	Peak BE	Atomic %	Peak BE	Atomic %
O1s	533.96	62.59	533.28	37.45	533.83	51.77	533.94	59.65
Si2p	104.82	30.64	104.16	21.56	104.39	27.7	104.85	29.83
F1s	689.92	1.57	689.09	0.99	686.05	2.03	688.84	3.60
C1s	286.41	4.37	286.3	31.93	286.03	17.03	286.33	4.95
N1s	0	0	401.13	6.97	0	0	0	0

Further, ellipsometry was used to determine the average monolayer thickness (**Table 5.2**). A model was used to fit the experimental data in order to extract the dielectric constant. The initial guess values were taken from literature. APTES – 0.55 nm [244]; POTS: 1.02 nm [245] ; TMODS : 1.3 nm [246]. The values obtained match literature very well.

Table 5.2. Ellipsometry data. The monolayer dielectric constant was the factor determined by the ellipsometry model, using estimated thickness values. Once these were found, the thickness was optimized and found to be fairly similar to literature.

Monolayer	Thickness (nm)	Dielectric constant (at 632.8 nm)
APTES	0.52 ± 0.06	13.42
TMODS	1.25 ± 0.28	14.32
POTS	1.09 ± 0.26	14.48

5.3.3. Electrical characterization

Introduced by Weaver and Abraham[247], Kelvin Probe Force microscopy is a force potentiometry technique which can be used to identity and distinguish between materials on a surface based on their specific work function. This makes it a powerful technique in the analysis of very flat surface, such as those covered with monolayers. Jeong *et al.* in their work on using SAM modified surfaces to improve EHD printed field-effect transistors utilized contact mode atomic force microscopy to study the topography of the surface.[68] Whilst successful in demonstrating the presence of monolayer, a greater understanding (perhaps) of the potentiometric properties of materials can be obtained using KPM. Biasing electric parts allows for even greater potentiometric differences to be observed. It also has the advantage that it performs tapping mode measurements of a surface along with collecting the surface potential information.

5.3.4. I-V characteristics of monolayers

Studies have reported that SAMs can be mechanically removed from surfaces.[232,248]. To ensure that this did not occur in these measurements, the electrical character of the SAMS were measured at discrete points with the aid of I-V traces (using conductive AFM). The

breakdown voltage values are summarized in **Table 5.3** and the breakdown voltages reported here are of the same order of magnitude as those found with other methods.[220,222]

Table 5.3. SAM Breakdown voltage. Breakdown voltages observed for various self-assembled monolayers along with the current, and electric field strength.

Monolayer	Breakdown voltage (V)	Current (μA)	Electric field strength (GV/m)
APTES	2.09 ± 0.15	26.99 ± 2.95	3.80 ± 0.27
POTS	2.40 ± 0.12	23.61 ± 3.99	2.35 ± 0.12
TMODS	2.46 ± 0.13	15.54 ± 3.56	1.89 ± 0.10

Work by Simmons, having described the electrical characteristics of a thin (dielectric) film separating two dissimilar electrodes, allows us to describe the observed breakdown behavior. At low currents (less than 1 μA), the junction resistance (in this case, that of the monolayer between the ITO and probing PtSi tip), is ohmic. This means that the polarity of the electrodes is not of importance; a linear response between I and V will be observed.[249] It is known, however, that a field created between the two electrodes equal to the difference in potentials, $(\phi_1 - \phi_2)/e$, where ϕ_1 is the potential of the PtSi tip and ϕ_2 the potential of the ITO substrate, generates an asymmetric potential barrier between the electrodes, thus rendering the directionality of the current important. Simmons' observations conclude that this directionality is only important for intermediate to high voltages (i.e. $V >> \phi_1$). Joule heating effects, then are seen for these larger voltages. For the monolayers discussed here, the breakdown voltage falls within the category of large voltage, thus a thermally induced breakdown is expected where the potential is applied (i.e. electro-oxidation). The localized nature of the breakdown can be used for the patterning of the SAMs, and can be visualized using KPM.

The directionality dependence is also observed in the present results, as breakdown only occurs with a forward bias. A further experiment to confirm whether Joule heating is responsible for monolayer damage was performed. KPM images of patterned ITO islands on SiO_2 were captured soon after SAM growth. These wafers were then heated to 300 °C for 15 mins, and KPM images taken again. This process was repeated four times and the KPM images used to determine the CPD values of the surface as a function of heating (**Figure 5.3**). The work function of all the monolayer coated surfaces increase after the initial 15 minute heating as the monolayers are annealed and experience oxidation. Macroscopically, the contact angle of POTS does not change significantly. This is explained by the fact that long chain SAMs are inherently more stable, especially if they have fluorine groups. TMODS, however, experiences the greatest contact angle change. The 'unprotected' alkyl groups are more prone to oxidation during extreme heating. APTES surface experiences a single large change of the contact angle and then remains stable, as it quickly oxidized owing to its short length.

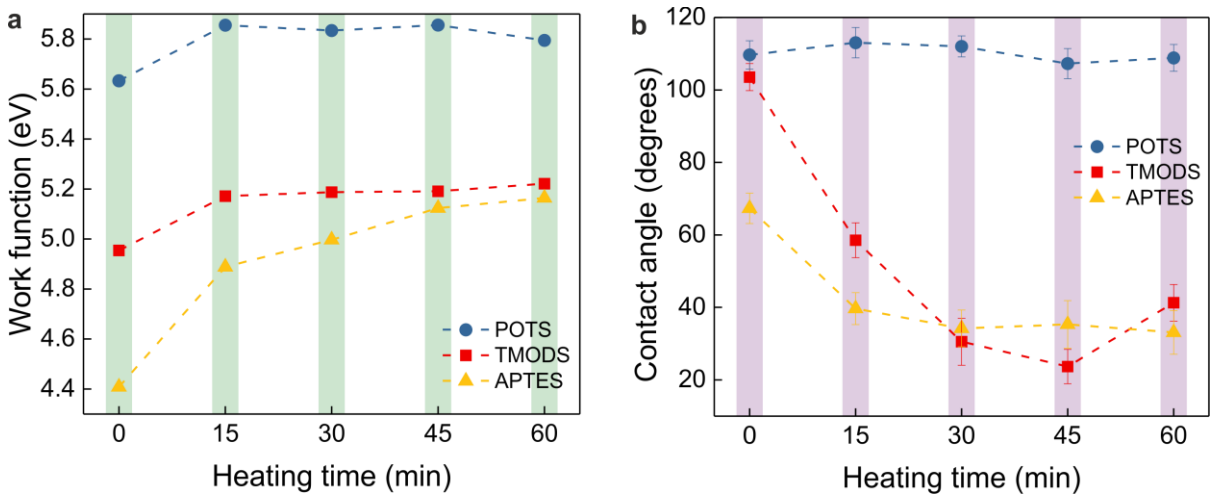

Figure 5.3. Thermal degradation characterization. Plots of the a) work function and b) resulting contact angle of water droplets were determined on samples after heating at 300 °C in intervals of 15 minutes.

5.3.5. Electrical patterning and characterization with KPFM

Having determined the breakdown voltage, I patterned a checkerboard design electrically using C-AFM into each monolayer coated surface. An initial tapping mode scan was performed

to ascertain the smoothness and homogeneity of the substrate. After this was confirmed, a bitmap image was converted into an electrical signal and patterned onto the monolayers (-2V – 8V). The KPM scans in **Figure 5.4.** reveal the exact area of patterning. Where no bias was applied, the contact potential difference (CPD) of the surface matches that of the surrounding unpatterned monolayer. This result demonstrates the superiority of KPM as a metrology tool in instances where SAMs are used. Not only does KPM provide CPD values, but it also allows for high-resolution spatial mapping, in order to better understand large area effects of electric fields on the SAMS. This is advantageous, compared to energy dispersive X-rays or scanning electron microscopy (SEM) imaging which give compositional and spatial information, respectively.

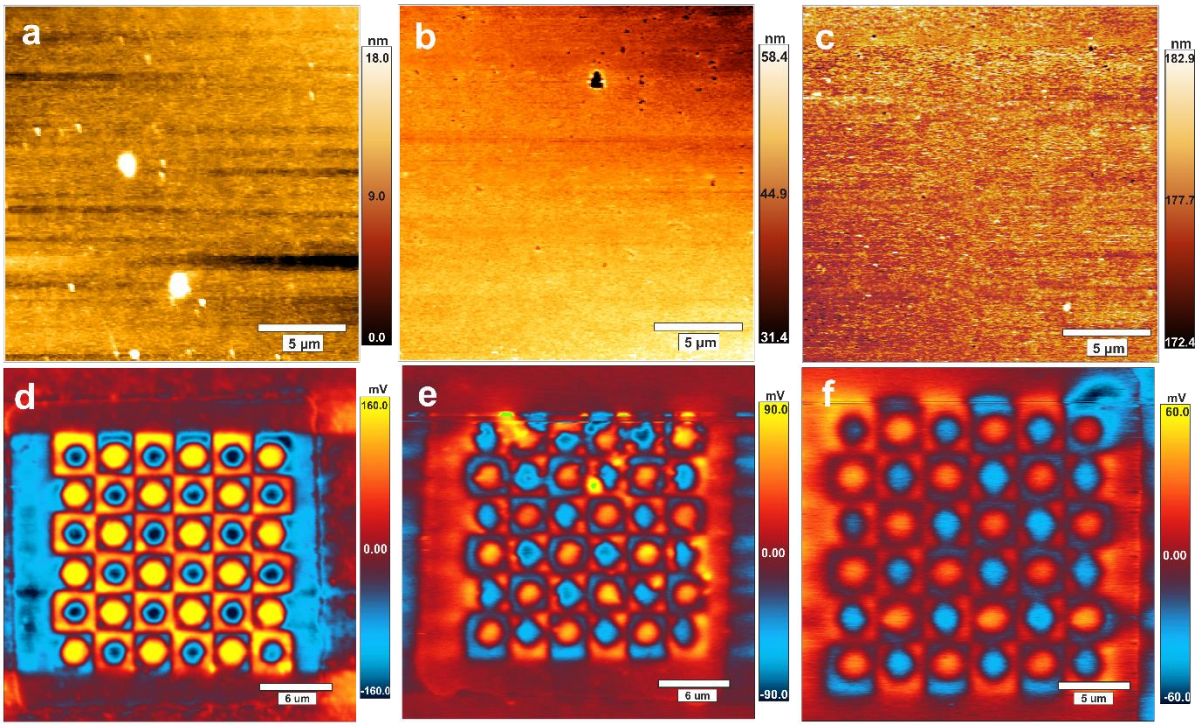

Figure 5.4. SAM coated surface AFM and KPM scans. (a) – (c) are the tapping mode scans obtained before electrical patterning of POTS, TMODS and APTES coated ITO squares respectively. (d) – (f) are the corresponding KPM scans after patterning has taken place. The CPD values have been normalized in this image for better contrast. The blue color is representative of unmodified POTS, and yellow/orange shows where breakdown has occurred. The reverse is true for both TMODS and APTES

5.3.6. Exposure to electric field

Following the preparation of SAMs on lithographically patterned indium tin oxide (ITO) surfaces, KPM was used to measure the CPD of the monolayer coated substrates both before and after the application of an electric field. The work function was then determined from this value using **Equation 5.1**,

$$V_{CPD} = \frac{\varphi_{tip} - \varphi_{sample}}{e}$$

$$\varphi_{sample} = \varphi_{tip} - eV_{CPD} \qquad \text{(Equation 5.1)}$$

Where ϕ_{tip} and ϕ_{sample} are the work functions of the tip and sample respectively, and e is the electronic charge. The V_{CPD} enacts an electrical force on the scan region, which is nullified by an equal and opposite V_{DC}. The magnitude of V_{DC} is equal to the difference between the tip and sample work function. Therefore, if the tip work function is known, the sample work function can be calculated.[250] Highly ordered pyrolytic graphite has a well-defined work function (4.6 eV) and was used to determine the work function of the tips applied in this work.[251] **Table 5.4** gives the magnitude of the calculated work function before and after electric field exposure for each SAM coated surface.

Table 5.4. Work function data for SAMs. (Applied voltage = 5.34 ± 0.59 kV, Electric field strength ~ 13.35 V/μm

	Positive field			Negative field		
Monolayer	ϕ before field (eV)	Φ after field (eV)	Δϕ (eV)	ϕ before field (eV)	Φ after field (eV)	Δϕ (eV)
APTES	4.37 ± 0.09	4.48 ± 0.07	0.11 ± 0.04	4.52 ± 0.06	4.41 ± 0.20	0.10 ± 0.04
POTS	5.31 ± 0.06	5.33 ± 0.07	0.02 ± 0.004	5.36 ± 0.11	5.32 ± 0.07	0.04 ± 0.02
TMODS	5.00 ± 0.01	4.93 ± 0.05	0.07 ± 0.03	5.06 ± 0.05	4.99 ± 0.03	0.07 ± 0.03

For both positively and negatively biased fields, APTES experiences a notable change in the work function. POTS measures a relatively small change under both fields. TMODS also registers a change, however it is the same (magnitude and sign) irrespective of the field orientation.

To explain these observations, I consider the pre-electric field work function values. Work done by Lü *et al.* reports on the variation of contact potential difference (CPD) values found using KPM for thiol SAMs of varying chain lengths and tail groups.[234] The authors found that longer chain methyl terminated molecules tend to exhibit higher CPD values, increasing 14.1 ± 3.1 mV per (-CH_2-) unit,[25] explaining why the TMODS CPD is lower than that of that of APTES even though methyl groups are more electron donating. It has also been demonstrated that fluorinated moieties exhibit lower CPD values than methyl-terminated analogous structures.[252] POTS not only has a terminal CF_3 group, but also several CF_2 units, which further decreases the CPD value owing to the inductive electron-withdrawing nature of the fluorine atoms. This is consistent with results reported previously for fluorinated monolayers.[236] The amino group in APTES is electron-withdrawing by the inductive effect,[253] thus a negative CPD value is expected, contrary to the positive value obtained. Amino-terminated SAMs are known to form ammonium (-NH_3^+) ions on the substrate surface,[254,255] and this charge deficiency may be a likely contributor to a higher CPD (thus lower work function) observed, since it is understood that CPD values are a result of the charge present on a surface and also the molecular dipole.[256,257]

The changes observed after the application of the electric field can be explained by the process of electrostriction, which is the mechanical shortening or lengthening of chain due to an electrostatic force. The dipole moment of the terminal groups is strongly affected by the external electric field. The intrinsic electric field of each monolayer interferes either constructively or destructively with the external electric field, depending on the dipole orientation. Sowlati-Hashjin and Matta have studied the chemical bonds of various homo and hetero diatomic molecules in external fields.[258] They found that diatomic molecules with large

dipole moments experience significant changes in the presence of external fields, irrespective of direction. If aligned with the field, the dipole increases (meaning the molecule extends). If aligned oppositely to the field, the dipole decreases (meaning a molecular compression). The result of these changes is observed in the change of the work function. This is what is observed in the present work. Work by Van Dyck *et al.* demonstrated that saturated chains, when in an electric field, experience a limited amount of charge reorganization due to low polarizability.[259] This is due to the low amount of delocalized electron density. This possibly explains the orientation invariance displayed by the TMODS.

5.3.7. Density functional theory calculations

In order to further understand the influence of the field on the dipole moment of the SAMs on covalently attached to the surface, I performed density functional theory (DFT) calculations. Geometry optimization DFT calculations were carried out using the B3LYP function of the Gaussian09 software packages[260], with 6-31G(d) basis sets. The dipole moment magnitude found for each SAM made chemical sense. The values are summarized in Table 5.5.

Table 5.5. Dipole moment of each SAM determined using computational density functional theory calculations. The level of accuracy afforded by this technique surpasses experimental methods.

Monolayer	$\boldsymbol{\mu}_{\perp}$ (D)	$\boldsymbol{\mu}_{x}$ (D)	$\boldsymbol{\mu}_{y}$ (D)	$\boldsymbol{\mu}$ (D)
APTES	-2.513	-0.0007	1.901	3.151
TMODS	-1.633	1.186	0.020	2.018
POTS	-3.681	-0.107	-0.0003	3.682

POTS with a greater number of electronegative atoms should indeed possess the greatest dipole moment. With the least number of electronegative atoms, TMODS should possess the smallest dipole moment. The change in work function is linked to the dipole moment by the Helmholtz equation (**Equation 5.2**).[261]

$$\Delta\phi = \frac{\mu_{\perp}}{A\varepsilon_{SAM}\varepsilon_0} \quad \text{(Equation. 5.2)}$$

Where $\mu_{\perp}$ is the component of the dipole moment perpendicular to the surface, *A* is the area covered by the monolayer, ε_{SAM} is the permittivity and ε_0 is the permittivity of free space. Looking to the Δφ, determined from the KPM measurements, we see that POTS experiences the least change. Electrostriction can again be used to explain this. When looking at the components of the dipoles, POTS has the largest $\mu_{\perp}$ and smallest in-plane dipole. APTES also has a large $\mu_{\perp}$ but also has a large in-plane component. TMODS is in between these two extremes. It follows that if the planar orientation of the dipole changes, the perpendicular component will change. This has a direct impact on the work function of the monolayer. Since Equation 5.2 relates the *change* in work function to the perpendicular component of the dipole moment, it requires there to be a reference point. In this work, the bare ITO onto which the SAMs were grown was used as the reference. $\Delta\phi$ is thus the given by **Equation 5.3**.

$$\Delta\phi = \phi_{(SAM+ITO)} - \phi_{ITO} \quad \text{(Equation 5.3)}$$

However, since I wish to determine the difference in the monolayer's work function alone, I can modify equation 5.2 to represent this, giving **Equation 5.4**

$$\Delta\phi = \phi_{(SAM\ before)} - \phi_{(SAM\ after)} \quad \text{(Equation 5.4)}$$

Thus removing the need to know the work function of the ITO alone. Plotting the $\Delta\phi$ values obtained using KPM against the magnitude of the perpendicular component of the dipole moment, **Figure 5.5** is obtained.

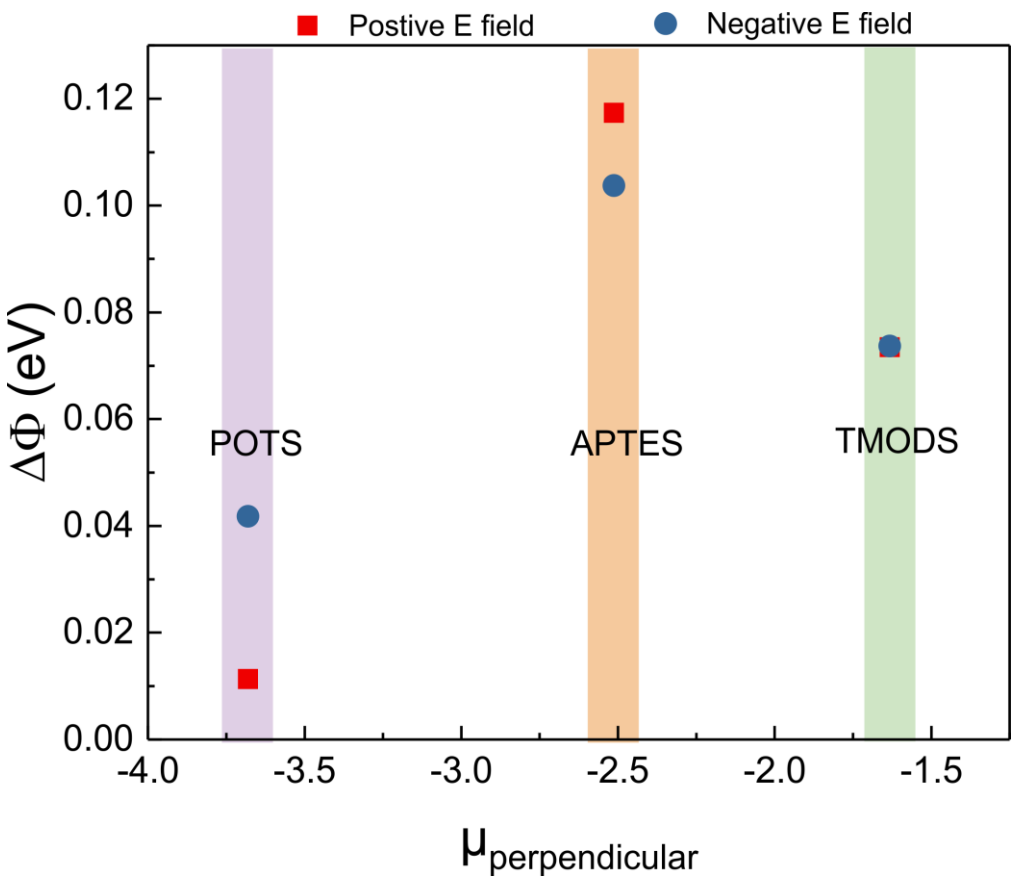

Figure 5.5. Consequence of field exposure. Visualization of the magnitude of the work function difference after exposure to either a negative or positive electric field as plotted against the magnitude of the perpendicular dipole moment.

5.3.7.1 Construction of the model

In order to more accurately study the influence of the field on the molecules, study was directed to a single unit cell of a monolayer on a few atomic layers of (100) silicon dioxide (**Figure 5.6**). Crystal structure coordinates of silica were obtained from the open crystallography database [262–266], structure 1536389 [267], from which a new unit cell was generated from a block of 2x2x2 unit cells, but with an increase in the *a* dimension to accommodate attachment to the (100) surface. The SAM was generated by substituting a single surface silicon atom with the silicon-derived systems. Dangling bonds at the SiO_2 interface were passivated using hydrogen, a standard literature-based treatment.[268] The periodic boundary conditions in the *b* and *c* dimensions allowed for an infinite surface, with a surface packing density of 1 molecule per

4.92x5.41Å^2, or 3.7 nm^{-2}. For TMODS, a starting conformation not crossing boundaries of the unit cell was chosen, with the expectation that some conformational change would occur during equilibration.

The coordinates of all systems were taken to the CPMD program for wavefunction optimization and for Car-Parrinello molecular dynamics (CPMD) calculations.[269] These calculations used the pure DFT BLYP functional, with Goedecker pseudopotentials for all atom types. The wavefunction was optimized prior to equilibration at 300K for 1000 steps of dynamics. Finally a production run of dynamics was performed at 300K for 20000 steps, from which results were measured. The timestep was 4.0 a.u. (0.0968 fs) for both equilibration and production dynamics, and this was used together with a fictitious electron mass of 400 a.u. Again, a positive and negative electric field was defined in order to elucidate the influence this would have on the molecule. The electric field vector was constructed to be perpendicular to the (100) surface of SiO_2, with a field strength of 0.0001 a.u. (1 a.u. = 5.14 x 10^5 V.μm^{-1}); the vectors were (-0.00866025, -0.00500000, 0.00000000) and (0.00866025, 0.00500000, 0.00000000) for fields directed toward and away from the surface respectively.

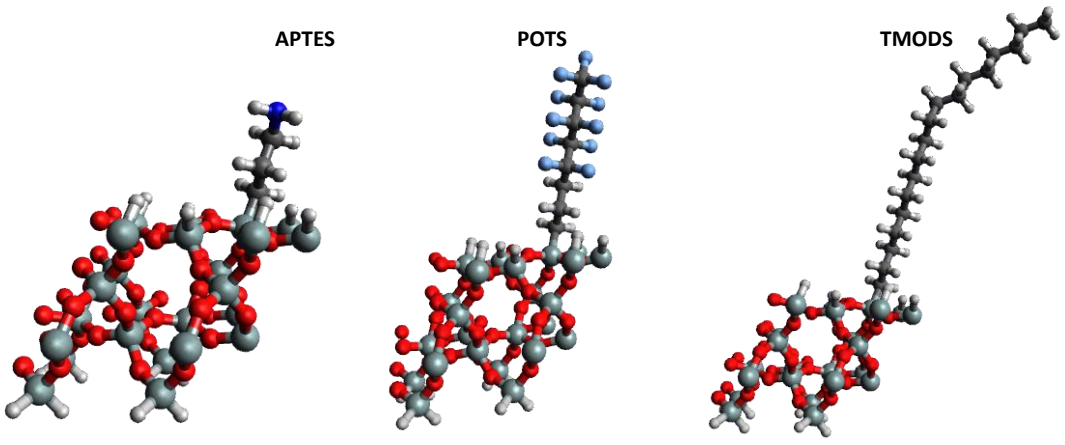

Figure 5.6. Optimized geometries of SAM molecules on (100) SiO_2 (single unit cell).

Figure 5.7 shows the difference in electron density between the positively applied field and the system to which no field is applied for the APTES attached system. The difference is highlighted in white, and shows the effect on silica oxygen atoms, but also the amine nitrogen groups, illustrating the sites most affected by the electric field. This is identical to the density difference when a field is applied in the opposite direction, away from the surface (not shown).

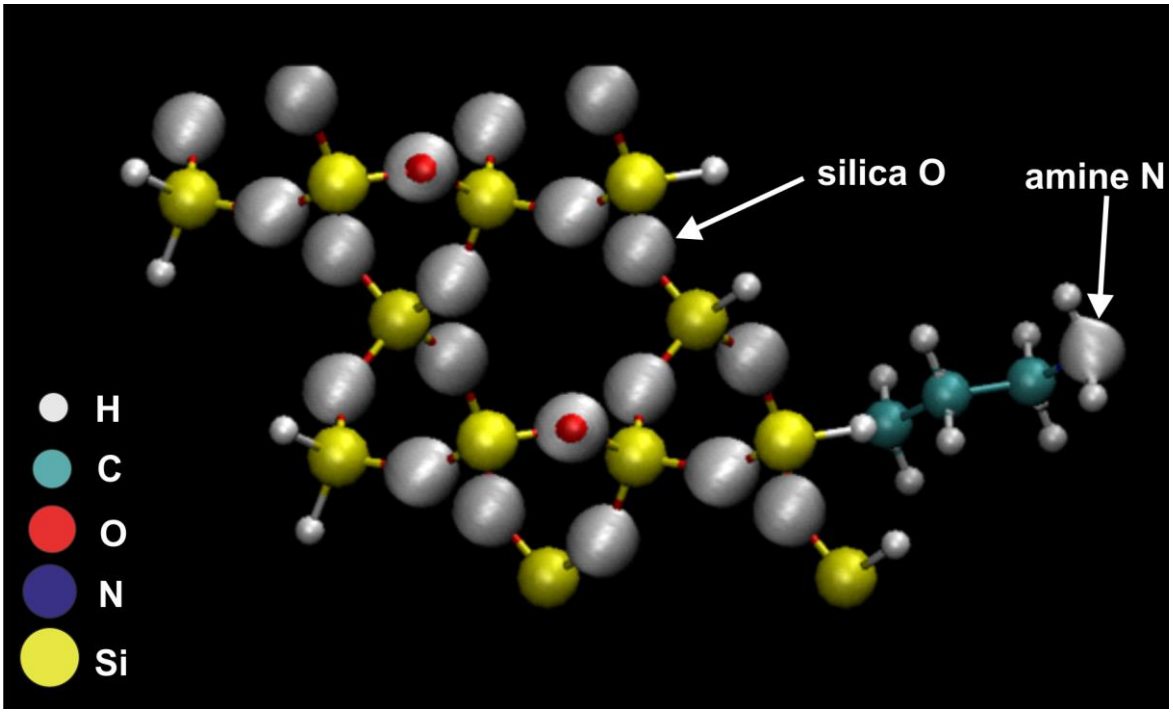

Figure 5.7. APTES difference in electron density for in both positive and negative electric field.

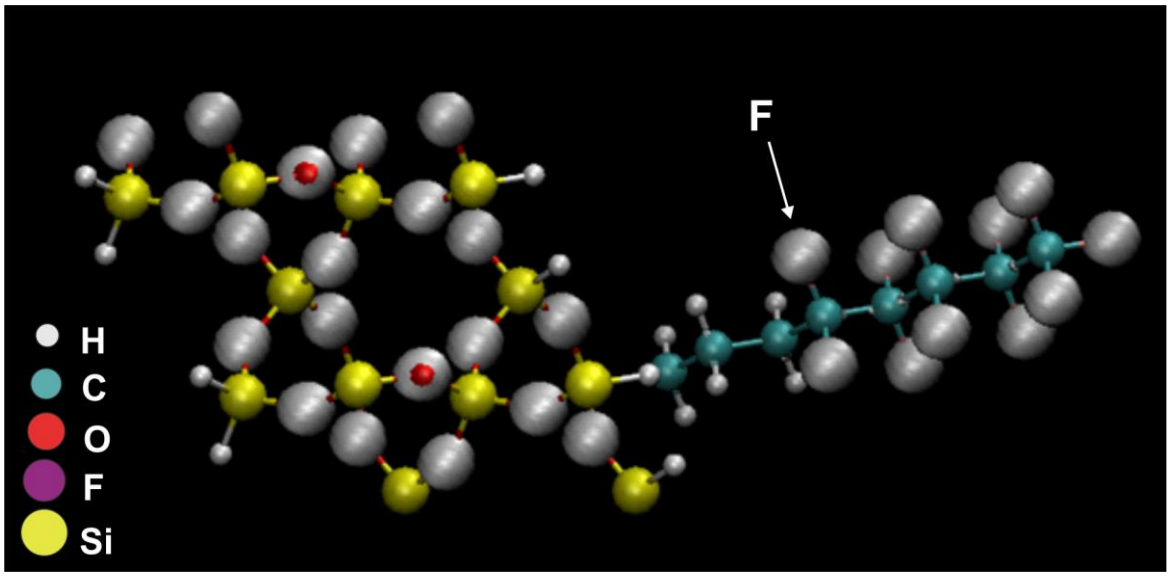

Figure 5.8. POTS visualization for both negative and positive electric fields.

Similar changes are seen for POTS (**Figure 5.8**), centred around the electronegative alkyl fluorine and silica oxygen atoms. Under the same conditions, for the TMODS system there is very little observable difference. At the same isosurface value for the density difference, no difference is observed. However when changing the isosurface value from 0.3 (used in all examples above) to 0.003 (a factor of 100) small differences are observed on the aliphatic chain (**Figure 5.9**).

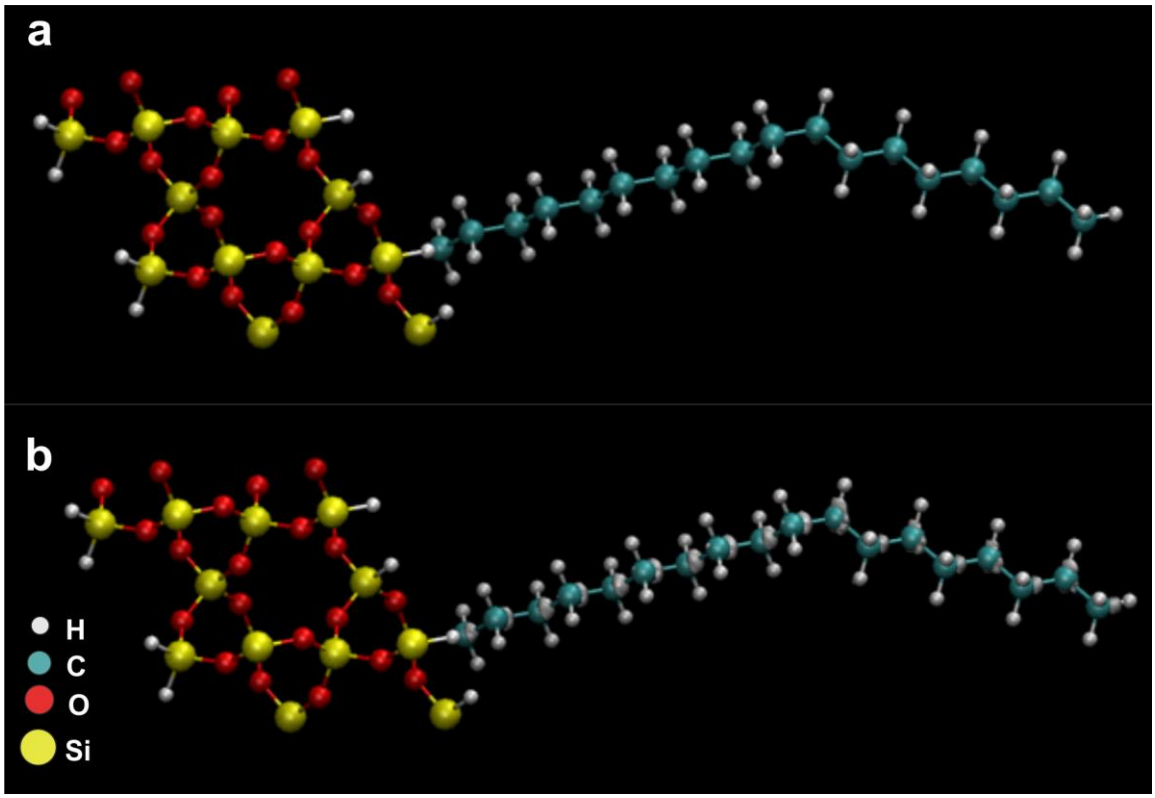

Figure 5.9. TMODS visualization for both positive and negative electric fields, a) with isosurface = 0.3. b) with isosurface = 0.003. Changing the isosurface value allows for clearer visualization of the electron density

In terms of molecular dynamics, the trajectories were analysed using Visual Molecular Dynamics (VMD) [270–277]. To evaluate the angle of attachment relative to the electrostatic field, the centre of mass of all atoms in the attached system with the exclusion of silicon and oxygen was determined. It was assumed that oxygen and silicon would be rigidly bound to the surface of the silica. This centre of mass, together with the Cartesian coordinates of the silicon attachment point was used to construct a vector, and the angle of this vector with respect to the electric field was monitored.

Although the dynamics does not show the final equilibrium, the angular change compared between dynamics in the presence or absence of fields could be compared (**Figure 5.10**). These results should be viewed in light of an estimation of the moment of inertia (using the centre of mass) of these systems about the attached silicon atom, with values of approximately 830, 17800 and 38300 amu.Å^2 for the APTES, POTS and TMODS systems respectively.

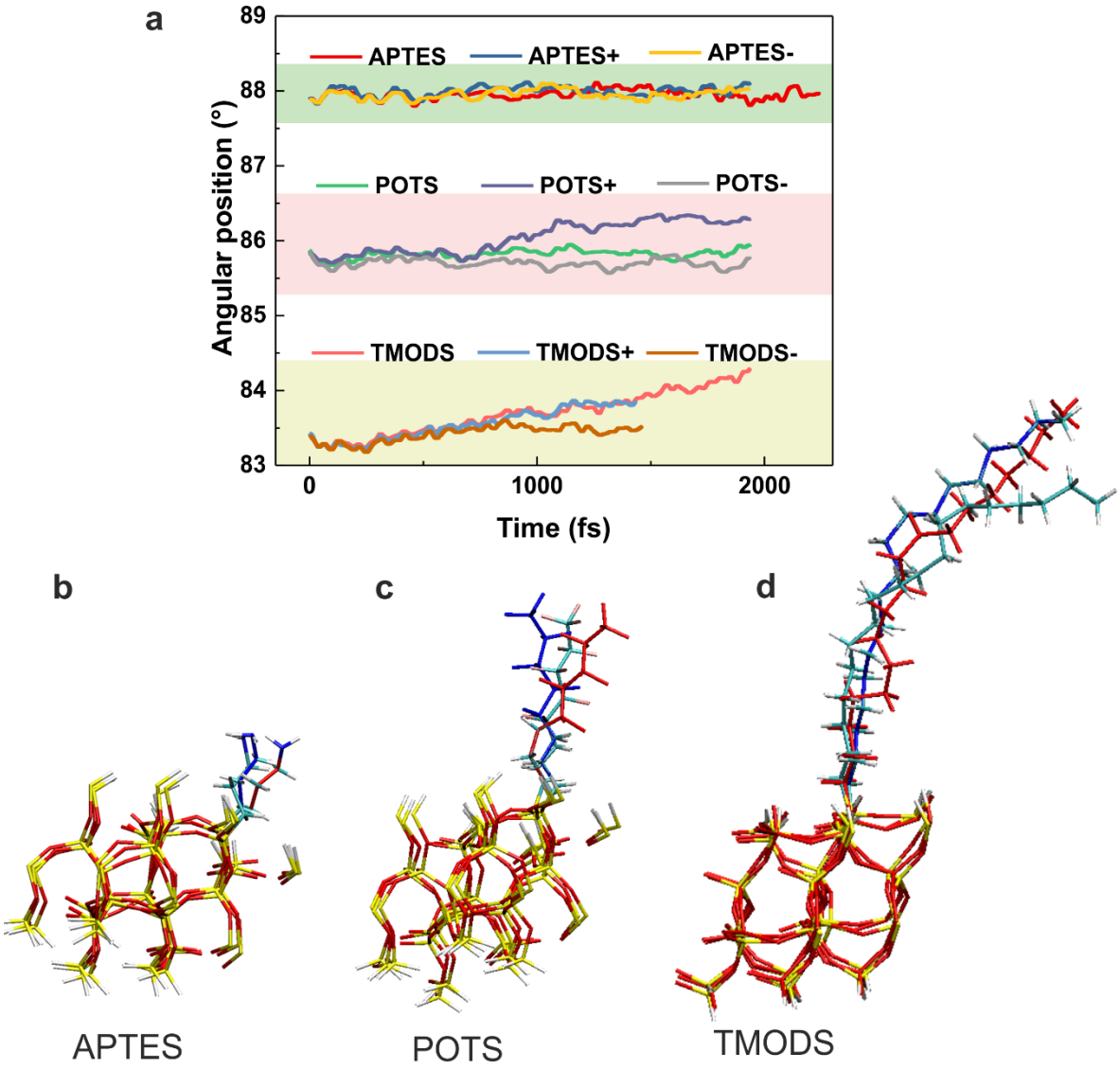

Figure 5.10. Angular position of SAMs in presence of electric field. Each monolayer was studied in its equilibrium state as well as both negative and positive electric fields. a) + next to the SAM name indicates a positive field, - indicates negative, and no symbol indicates no field. Over time, the angular position of the molecules changes, even when no field is applied, but more greatly during field application. APTES does not show a large variation in angular position, whereas both TMODS and POTS do. This is primarily due to their length. The length of TMODS restricted the computation time permissible, hence why the molecule under electric field was only partially studied. This is clearly seen in snapshots of the dynamic model under all three conditions for b) APTES, c) POTS and d) TMODS.

5.3.9. Contact angle measurments

Fluorinated SAMs are known to impart pronounced hydrophobicity (contact angles greater than 95°), as do long chain alkylsilanes such as octadecyltrichlorosilane, amongst others.[242,278] Amino terminated SAMs are less hydrophobic[244], and are more useful in applications where further functionalization of surfaces, especially with biomolecules or nanoparticles of interest, is desired. Most SAMs remain stable on surfaces for several weeks when stored in appropriate conditions (dry, ambient temperature), where they, therefore, can maintain the same contact angle.[279] **Figure 5.11** illustrates the contact angles observed for each surface, as well as the functional groups responsible.

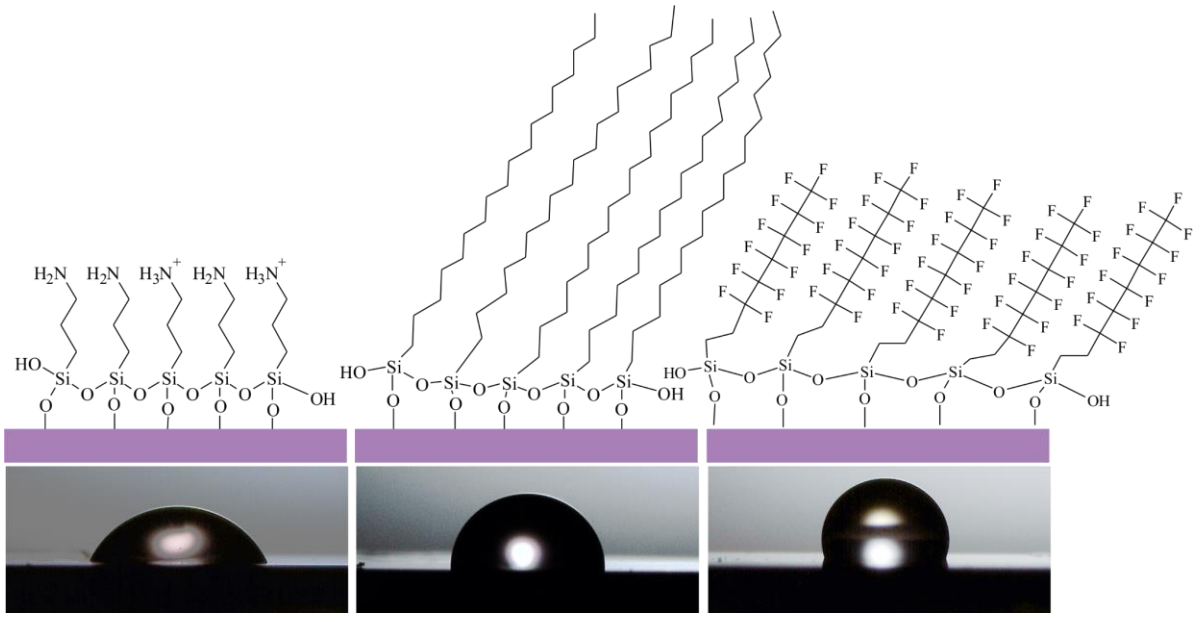

Figure 5.11. Self-assembled monolayers on oxide substrate and associated contact angles. Images of droplets used to determine contact angle on different SAM coated substrates.

The results (**Table 5.6**) demonstrate that there is a minor, but noticeable, difference in all the contact angles for the SAMs studied after exposure to the electric field. This has implications for the resolution which can be achieved. Observing a positive change (increase in CA) means that the resolution expected should be enhanced, whilst the opposite is true for a negative change. This experiment was carried out in triplicate, and each time changes in the

contact angle observed. However, the nature of the change is not always consistent. On average, however, the contact angle for all SAMs investigated increases. This result corroborates the increase in work function observed. As the monolayer is distorted in the field, electron density shifts towards making the surface more polar. This increases the affinity towards polar molecules, such as water, leading to better wetting.

Table 5.6. Contact angle data. Water contact angle was measured before and after exposure to electric field.

Monolayer	CA before field (°)	CA after field (°)	ΔCA (°) (after – before)
APTES	59.1 ± 0.9	63.7 ± 0.7	4.6 ± 1.6
POTS	103.6 ± 0.6	107.9 ± 0.5	4.3 ± 1.1
TMODS	88.5 ± 0.7	91.5 ± 0.5	3.0 ± 1.2

There are two possible reasons for the change observed. Either the chemical surface has changed, or the actual physical surface roughness has changed. The roughness of SAM layers is primarily a result of monolayer growth time and the smoothness of the underlying substrate.[280] Since there was no mechanical modification involved at all, the observed change must be from a physicochemical perspective. Correlating the observed CA changes to the KPM values obtained for the work function, it can be deduced that there has been a chemical change which resulted in a change of the work function. The work function is a good indicator for whether the kind of interfacial tension between the liquid and surface will be high or low.[281] A higher work function will result in a higher interfacial tension, thus promoting higher contact angles. This was observed, for both POTS and TMODS, but not for APTES. This discrepancy is likely due to the short chain length of the APTES molecule, implying that the physical morphology (roughness) may have contributed more to the contact angle than the surface potential.

Liu *et al.* compare four nanolithography techniques which result in patterning of SAMS, namely nanografting, nanoshaving, electron induced diffusion an electron induced evaporation.[248] During the EHD process, owing to the close proximity of the capillary to the surface, electron induced effects are more likely to cause SAM damage rather than mechanical processes. It is plausible that electron induced structural rearrangement can take place as this has been demonstrated in solution using potentials.[282] The results obtained in this study for the damage caused over a distance are more consistent with the theory of electron-induced damage than that of mechanical damage. Firstly, there is no discernible mechanical damage using surface mapping AFM. Secondly, the surface potential is consistent with energies observed for alkyl chain bonds. Thirdly, the contact angle changes highlight the hydrophobic nature of the surface after the terminal group's dipole moments have been realigned. This last point is corroborated by the work done by Fresco and Frechet, demonstrating that some chemical moieties are prone to damage in the presence of electric fields.[283] In instances where there is no contact between the tip and substrate, long range field effects lead to a rearrangement of the dipole of the monolayers.

The roughness and cleanliness of surfaces used for growing monolayers are important. For instance, it is known from literature that native oxide surfaces are very rough in their nature (~3 nm) and so this roughness will contribute extensively to the roughness of the monolayer, and thus affect the contact angle observed, both from a chemical and a morphological perspective.[284] Sputtered thin films (such as indium tin oxide) also have an inherent roughness which translates across. It is therefore crucial to have this information available during monolayer analysis in order to know the possible contribution of surface morphology to the overall resolution achieved in EHD printing. This information is collected in this work, but is not a central focus. By utilizing both solvent and oxygen plasma cleaning of the ITO surface on which monolayer growth is done, I ensured that no contaminants were present which would affect the results obtained.

5.4. Physical methods of surface control (Future work)

So far in this thesis, I have demonstrated the control of surface wetting using chemical means. Physical means of modification can also alter the wetting properties of surfaces, mimicking occurrences in nature. Normally, the fabrication of structures which give rise to these modified wetting properties requires extensive fabrication. For example, Yoshimitsu *et al*. demonstrated the use of micropillars as a means to pin a liquid droplet to a surface, which required extensive lithography.[285] Others have used mechanical surface roughening, laser microtexturing and plasma processing to form structures which affect the wetting of surfaces.[286–288] A facile method would be beneficial to achieve this. Further, the use of SAMs on structural modifications has also been shown to allow the attainment of superhydrophobicity. An alternative strategy should be able to attain this same level of surface wetting. The rest of this chapter is devoted to this. The work shown is still in its preliminary phase, but the results so far demonstrate the concept.

5.4.1. Spontaneous surface wrinkles

When a thin layer of material is deposited onto polydimethylsiloxane, a commonly used elastomer, interfacial tension results in the deposited material buckling. This buckling arises due to the mismatch between the coefficients of thermal expansion. During deposition, the PDMS expands, increasing its surface area. After the process, it contracts, thus buckling the now deposited material on top of it. It has also been demonstrated that this type of buckling instability arises, too, when PDMS is exposed to oxygen plasma treatment for a period of time.[193] This is due to the conversion of the first few nanometres from siloxane to oxide, thus changing the bonding and physical structure. This buckling phenomenon was first reported by Bowden *et al.* where they demonstrated the ability to control the directionality of these spontaneous wrinkles.[289] Recently, Xie *et al*. demonstrated anti-counterfeiting technology which exploits the dynamic and unique nature of these wrinkles. By using an infrared sensitive top layer, they were able to create a “finger print” that only revealed itself in the appropriate irradiation, leading to concealable, unclonable identification.[290] Daramola conducted a

thorough study to understand the mechanism behind the wrinkling for both thin film deposition and plasma treatment methodologies.[291] In my work, I made use of SiO_2 as the sputtered layer. The method used to prepare each sample is summarized in the schematic shown in **Figure 5.12**.

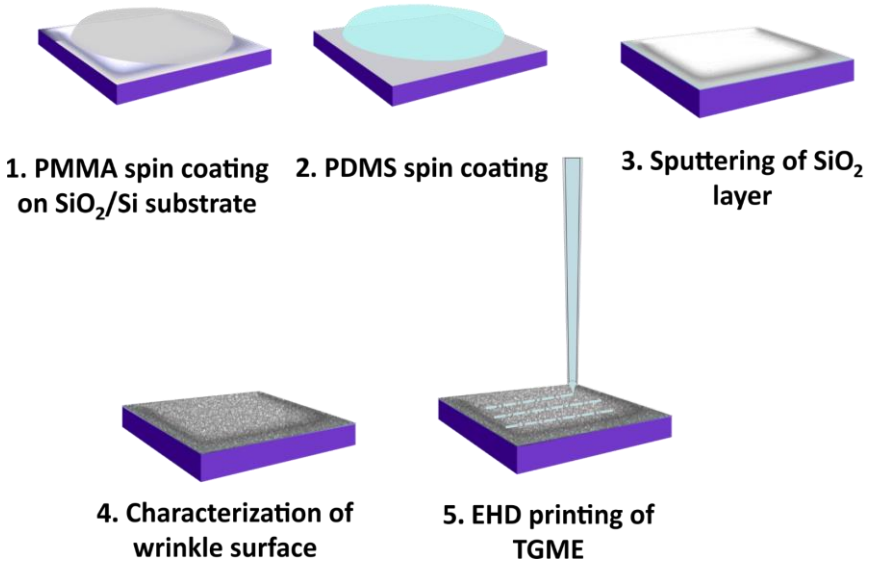

Figure 5.12. Schematic of wrinkle surface preparation and printing. 1) The SiO_2 wafer is primed with a layer of PMMA, to allow for easy detachment of the PDMS. 2) A mixture of 10 wt% PDMS in n-hexane is spin coated onto the primed wafer. 3) A thin layer (20 – 150 nm) of SiO_2 is sputtered on the PDMS to induce the buckling. 4) AFM is used to determine the wrinkle amplitude and wavelength. 5) EHD printing of solvent ink, and subsequent characterization.

Figure 5.13 a-c demonstrates the result of depositing 20 nm, 50 nm and 100 nm of SiO_2 respectively, on a PDMS layer spin coated on a SiO_2/Si wafer. AFM was used to determine both the anisotropic wrinkle amplitude and wavelength. The line profiles in **Figure 5.13 d** show that two wavelengths exist. One exists on the microscale, and is indicative of the large strain effects. Within these micro wrinkles exist the nanoscale wrinkles which gives the fingerprint like texture. In this work however, I determine the larger of these wavelengths. The aspect ratio given by wavelength to amplitude values indicates the roughness of the surface. More samples were prepared with different SiO_2 thicknesses, and I found that a linear relationship

exists between the wrinkle amplitude and the thickness of SiO_2 deposited to create the wrinkles (**Figure 5.13 e**), given by the relation y (amplitude) = 6.34x, where x is the SiO_2 thickness. The magnitude of the amplitude is approximately an order of magnitude larger than the thickness of the sputtered silica. This has been explained before in literature.

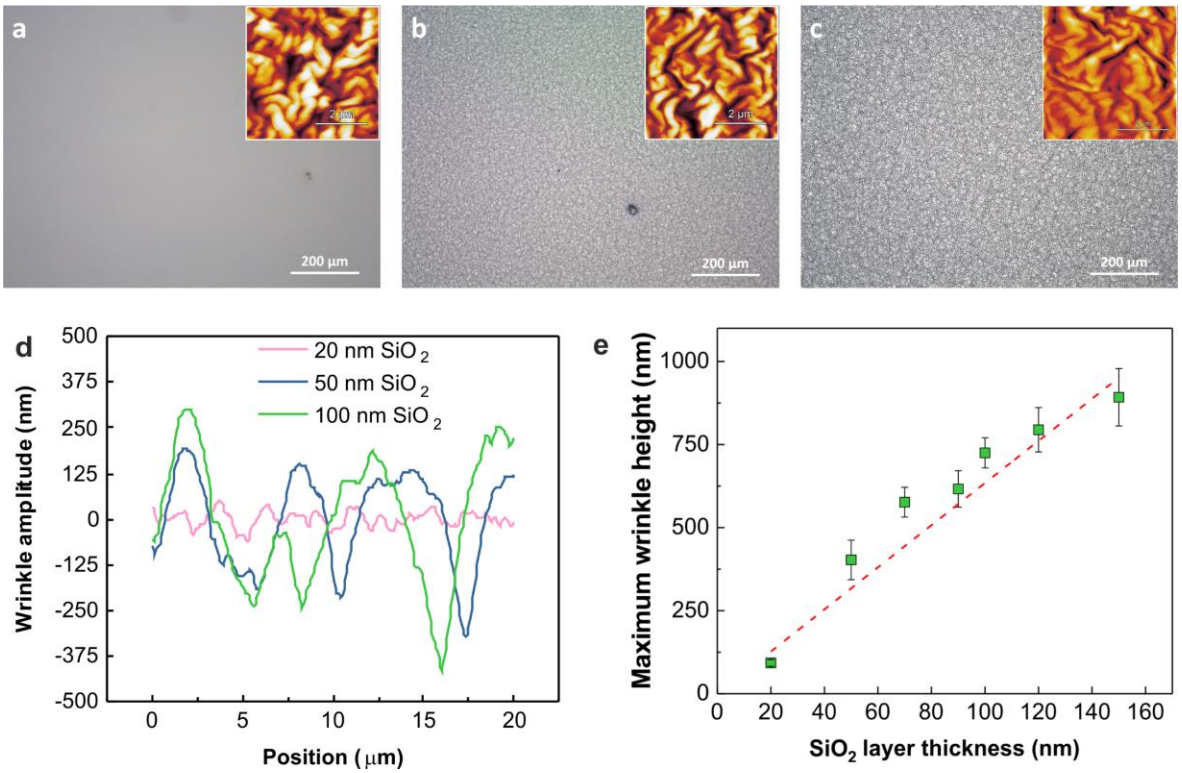

Figure 5.13. AFM characterization of wrinkles**.** Varying SiO_2 thickness on 10% w/w PDMS layer. By increasing the thickness of deposited silicon dioxide on PDMS, I obtain more pronounced wrinkling. (a) 20 nm has very little, (b) 50 nm is more visible, and (c) 100 nm is very pronounced. d) An averaged line profile of each thickness top layer reveals how the thickness changes the amplitude. e) The maximum peak to trough distance found for various thickness of deposited SiO_2. The wrinkle height grows at a rate of 6.34 nm/nm

The wrinkle wavelength also varies linearly with deposited SiO_2 layer thickness. The small strain theory equation (**Equation 5.5**) can be used to estimate the wavelength as a function of thin film thickness[292]

$$\lambda = 2\pi h \left(\frac{\overline{E_f}}{3\overline{E_s}}\right)^{1/3} \qquad \text{(Equation 5.5)}$$

Where h is the thin film thickness (in this case the deposited SiO_2), E_f and E_s are the Young's modulus values for the film and PDMS substrate respectively. However, another assumption made is that the substrate thickness is much greater than the film thickness. In this preliminary work, this is not the case, therefore the equation may not be fully applicable due to strain from the underlying rigid substrate. Using 2D discrete Fourier transform, the wavelength is experimentally determined, and used to determine the aspect ratio (**Table 5.7**). The wavelengths determined follow a weakly linear relationship with the film thickness. The variation could be from the fact that small scans were used in the calculation. If larger scan sizes were used, perhaps a more representative wavelength could be determined.

Table 5.7. Average wavelength of wrinkles as function of sputtered SiO_2 thickness. The aspect ratio gives a measure of roughness, which contributes to better wetting control.

SiO_2 thickness (nm)	**Amplitude (nm)**	**Wavelength, λ (μm)**	**Aspect ratio (Amplitude/wavelength)**
20	92.65	2.20	42
50	402.75	3.98	101
70	576.72	3.70	156
90	616.51	6.79	91
100	725.07	4.45	163
120	794.59	6.68	119
150	892.37	8.91	100

5.4.2. Effect of wrinkles on printed resolution

It is known that increasing the roughness of a surface leads to an increase of the contact angle, when comparing to a smooth surface of the same material. Increased roughness also leads to higher pinning rates. The idea behind using the spontaneous wrinkles came from

these two facts. By increasing the roughness of the PDMS surface, I hoped to achieve both high contact angles (and thus the ability to print with high resolution) as well as increased pinning, thus preventing the possibility of 'wicking'. However, this wicking-like behaviour is observed for a lot of the printing, as was demonstrated in work by Semprebon *et al*.[293] As they observed experimentally with high aspect ratio square pillars, the spontaneous formation of liquid films is not always dependant on energy considerations. In fact, similar work has been done by Chung *et al*. They studied the influence of the anisotropic micro-wrinkles with well-defined aspect ratios on the wetting.[294] They found that wetting was reducing on surfaces with high aspect ratios owing to the increased number of pinning barriers. However, this work was performed on wrinkles which were formed on pre-strained PDMS surfaces, meaning that the wrinkles were isotropic. Having anisotropic wrinkles, such as those which I have demonstrated, could allow for better resolution control of EHD printed structures. **Figure 5.14** is a summary of printing done on surfaces with different wrinkle depths, and at different speeds. **Figure 5.14 a-c** are 20 nm SiO_2, d – f are 50 nm SiO_2, g – i are 100 nm SiO_2 and j – l are bare PDMS. The three printing speeds used are 5, 10 and 15 mm/s, with a 30 μm wide tip, at a height of 200 μm. The apparent trend (excluding the bare PDMS), is that high speed and high wrinkle aspect ratio are the best conditions to achieve high resolution. Comparing Figure **5.14 i** and **l**, (both 15 mm/s printing, but 100 nm and 0 nm SiO_2, respectively), the pinning induced by the wrinkles is able to overcome the hydrophobicity which causes the droplet formation on the PDMS alone. Extensive wicking is observed where an insufficient

roughness exists. For the surfaces on which printing has been demonstrated, the resolution improves with an increase in aspect ratio.

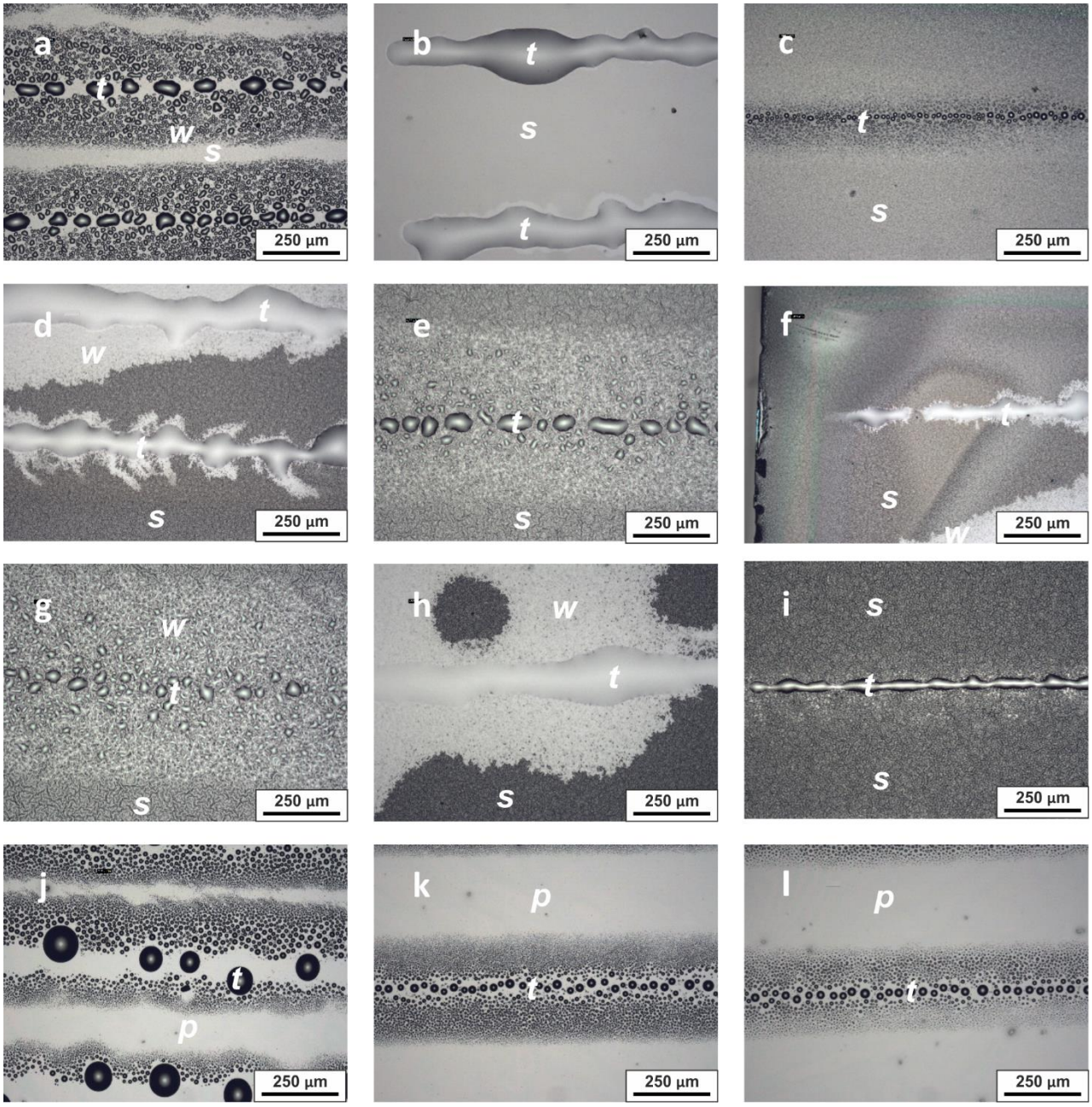

Figure 5.14. Printing on PDMS surfaces. TGME was printed on each PDMS coated wafer. Each row represents 20, 50, 100 and 0 nm of deposited SiO_2 respectively, and each column is for printing speed 5, 10 and 15 mm/s. In general, good resolution is observed for printing at 15 mm/s, with the best resolution being found on i) 100 nm thick SiO_2. This result agrees with literature. On each surface, printed TGME is labelled ***t***, SiO_2/PDMS surface is labelled ***s***, spread TGME (due to wicking) is labelled ***w***, and PDMS with no SiO_2 is labelled ***p***.

This form of modification then, is a promising means to achieving high resolution EHD printing. Further functionalities could be obtained by using other materials for inducing the wrinkle formation, including indium tin oxide, zinc oxide and many others. I have noted (as has the study by Chung), that after specific amounts of material have been deposited (or different strains applied), the material no longer induces wrinkling, but rather forms cracks which no longer mechanically buckle the PDMS due to delamination.

5.5. Discussion

The control of surface wetting is a crucial effort in the pursuit of controlling EHD printing resolution. Kelvin Probe Microscopy results obtained in this study have revealed the extent by which three commonly used SAMs are affected by exposure to electric fields. This influence was observed for both positive and negative field polarity. While the SAMs do not undergo dielectric breakdown with this non-contact field, as they do when probed with contact AFM, they do exhibit a conformational change, whose full extent is dependent on the magnitude of the dipole moment. This hypothesis as further confirmed by the CPMD calculations performed. As the SAMs are exposed to the electric field, their spatial orientation changes. The rearrangement of their electron density alters the dipole moment. This relationship is best understood by using the Helmholtz equation, however in this no trend can be drawn as different SAM molecules were examined. What might be a large change in the surface potential for POTS might be a small change for another monolayer. A future experiment could examine the relationship more closely by applying electric fields of different strengths and measure the change in the surface potential. However, looking at the magnitude of the change in surface potential (for both negative and positive fields), the similarity does make sense. Figure 5.10 predicts that the physical conformation change should be similar for both field directions. This would mean that the equation should yield the same result irrespective. This is what is experimentally observed.

Contact angle measurements demonstrate the macroscopic influence of the dipole rearrangement after electric field exposure of the substrates. In this work, I have measured

that the resultant contact angles for all three SAMs increase, meaning that the surfaces become less wettable. The changes observed can be applied to what can be expected with printing. This result, however, should not be confused with electro-wetting, which is a dynamic process of wetting whilst a field or potential is applied.[295,296] The results suggest then that exposing surfaces to electric fields actually aids the resolution. Whilst this bodes well for EHD printing, the nature of the ink being printed must be taken into consideration. If this result is a general one, it means that printing non-polar inks would result in poor resolution. More work on testing such inks is required before such a conclusion can be reached. Performing these experiments in an inert atmosphere would allow the probing of much stronger fields (in order to prevent electric discharge).

The mechanical buckling of PDMS can be utilized to control surface wetting, with no influence of the electric field on the surface. This is corroborated by the work of Tsougeni *et al*. where they demonstrate superhydrophobicity of similar surfaces.[288] However, the limitation to this approach would be that the ink would need to be of sufficient surface tension to prevent spontaneous wicking in high aspect ratio wrinkles. Further, the use of SiO_2 could hamper the printing process, owing to it being an insulating surface. Using conductive films like gold or other metals could aid in the printing being made easier.

5.6. Conclusions

Two methods were used to induce change on self-assembled monolayer coated substrates, and the effects measured with Kelvin probe force microscopy and contact angle measurements. Electrochemical oxidation is the mechanism responsible for localized monolayer damage when using C-AFM above the SAM breakdown voltage. With this information, the breakdown properties of three common monolayers on an indium tin oxide surface were characterized. Electrostatic fields created over a surface with monolayers have appeared to cause an alignment of the monolayer functional group dipoles, resulting in a change of the surface potential and observed contact angle of a water droplet on the substrate. These results provide insight into the considerations that need to be made when choosing a

monolayer as a wetting control agent. Depending on the desired outcome, the correct monolayer must be chosen which can withstand the fields used. Sufficient time, too, must be allowed for uniform and quality SAM films to be grown to ensure homogeneity of the surface.

In order to ensure that no damage occurs to the monolayer, the field strength needs to be minimized to below the threshold magnitude (breakdown field). This would require that the applied potential be accurately calibrated, as well as the working distance. EHD inherently has fields several orders of magnitude weaker than C-AFM, however the effect can still be observed. It is crucial also to prevent electrical discharge between the tip and the sample, as the localized heat may induce substantial damage. Kelvin probe microscopy is an essential tool for effective inline metrology of self-assembled monolayers. Its ability to provide physical information as well as allow for the determination of chemical changes spatially makes it undoubtedly the most useful tool for assessing molecular film integrity, as compared to other surface analysis techniques.

Finally, much work has been published with regards to the use of PDMS buckled surfaces as wetting agents, however no one has demonstrated their influence on printing resolution. This work offers the first demonstration of the utilization of this physical consequence with EHD for resolution control. By controlling the wrinkle amplitude and printing speed, comparatively higher resolution printing is demonstrated.

5.7. Author Contributions

I performed all experimental aspects of this work, including the monolayer growth, AFM, electric field application, contact angle measurements and analysis. I also conceptualized the majority of the computational experiments presented. CPMD calculations and modelling were done by Prof. Kevin A. Lobb (Rhodes University, South Africa). XPS measurements were made by the Oxford Materials Characterization service. Ellipsometry measurements were performed by Dr Sharizal Alias. Preparation of the PDMS surfaces were performed in the Denys Wilkinson Building cleanroom.

Chapter 6

Printing sensors with better sensitivity using EHD

6.1. Introduction

In the previous chapters, I have demonstrated how it is possible to use EHD printing as a facile technique to achieve high resolution printing. I have demonstrated the capability of designing new sensor scaffolds with the printing of self-assembly monolayer templates. I have also demonstrated how important it is to have an understanding of the surface chemistry and structure of the substrate on which printing is being done. In this chapter, a demonstration of a functional device prepared using EHD is shown. First showing how a traditional preparation method fails to produce a sensor of suitable performance, I introduce the benefit of using EHD printing to enhance the sensitivity of polyaniline (PANI) based ammonia sensors. As has been mentioned in earlier chapters, electrohydrodynamic jet printing has emerged as one of the most promising additive manufacturing techniques.[38,297] The basic principle of EHD (**Figure 6.1a (inset)**) is that a potential is applied between a nozzle and ground plane, whereby an electric field is created. This field causes meniscus deformation when the electrostatic force is greater than the ink's surface tension, resulting in the formation of a Taylor cone.[100] The magnitude of the applied bias determines the jetting mode obtained.[55] Importantly, the size reduction in jet diameter offered by EHD is especially important in pursuits such as nanofabrication, where the size limits of devices and structures are currently restricted with existing extrusion technologies, such as inkjet printing.[14,105] It is this last point that is exploited in this work.

The traditional preparation of chemiresistive polymer sensors[6] has relied on techniques such as drop-casting[298], inkjet printing[299,300], electrochemical deposition[301–303], spin-coating, dip-coating, layer by layer self-assembly, Langmuir-Blodgett film assembly[304], vapour deposition and thermal evaporation. These methods have produced sensors with improved response times, mechanical properties and operating conditions, as compared to metal oxide (MO) based sensors, which operate at high temperatures and exhibit longer response time.[305]

[6] A sensor whose resistance changes as a response to the chemical environment around it.

One of the biggest advantages that MO sensors have over polymer sensors is that they can be miniaturized easily, hence why they currently dominate the sensor market. The additive fabrication methods listed above are not able to easily fabricate miniature sensors, thus new ways of achieving this miniaturization are needed to make conducting polymer sensors commercially viable. Herein, I demonstrate the ability of EHD printing to achieve deposition of material on the microscale to create a functional polymer chemiresistor sensor for the detection of ammonia. Zhan *et al.* demonstrated an initial study with EHD onto rigid substrates, but obtained limited sensing results, and did not compare their results with other preparation methods.[306] They focused on the optimization of the printing process, whereas here, the improvement of sensitivity by virtue of the preparation method is the distinguishing factor.

Ammonia is an industrially crucial chemical compound, used in the production of fertilizers, cleaning agents, and in other chemical processes.[307] Excessive exposure for humans can lead to detrimental health conditions, including severe respiratory problems such as shortness of breath, chronic bronchitis, chest tightness etc.[308] As such, sensors have been employed to monitor ammonia levels in order to comply with the National Institute for Occupational Safety and Health in the United States (NIOSH), which has set the maximum exposure limit of ammonia for humans to 25 ppm.[309] The human nose can detect ammonia at levels as low as 5 ppm, however damage to the eyes, nose and throat start to occur at 50 ppm.[310] Currently, a variety of ammonia sensors exist[311–313], including metal-oxide gas sensors, catalytic sensors, optical gas sensors, and organic sensors. In this chapter, I utilize PANI to create an ammonia sensor, owing to its ability to detect the analyte, which has been demonstrated before.[314–318] By using solutions prepared from the emeraldine base form of PANI, I eliminate much of the potential risk of exposure to toxic precursors such as aniline, normally used in preparing PANI.[319] The mechanism of how PANI reversibly interacts with ammonia is well-known.[320] I exploit this reaction and monitor the change of resistance of the PANI during controlled ammonia exposure, thus characterizing the performance of each sensor. The sensitivity of previously demonstrated PANI chemiresistors has been limited by the fact that

the preparation methods result in large area films. Here, I demonstrate high sensitivity for the detection of ammonia by printing discrete regions of PANI onto interdigitated electrodes (**Figure 6.1**). In the work presented, I showcase chemiresistive sensors in ambient conditions that require no heating, which enables simple, energy efficient ammonia detection. This is a major advantage over MO sensors.

Notably, I demonstrate that using an appropriate doping acid is central to achieving high levels of sensitivity. PANI doped with three different acid compositions is studied. The

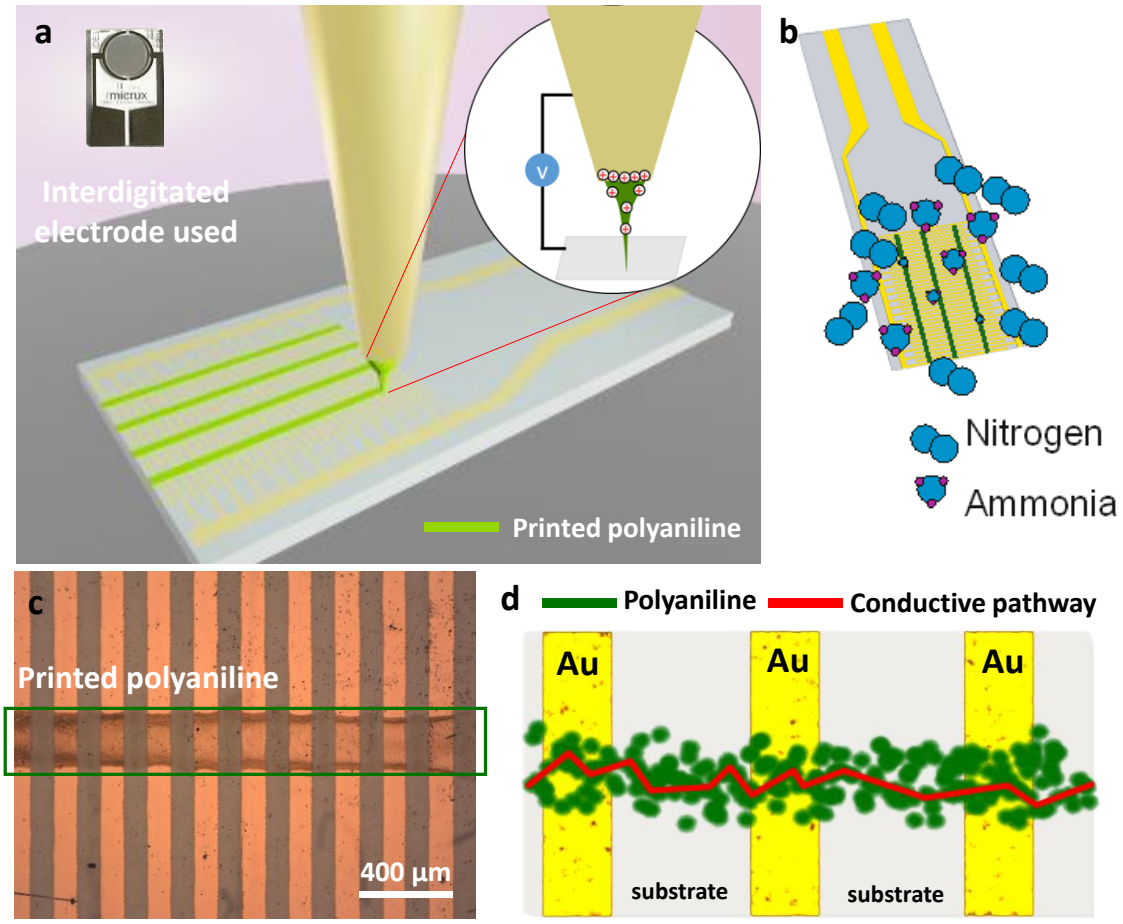

Figure 6.1. Schematic of EHD printing and the detection of ammonia. a**.** A potential is applied to the ink-containing capillary and an electric field induces the printing. Inset: Interdigitated electrodes on glass substrate used in this work. b. An illustration of how the ammonia will interact with the printed polyaniline. c. An optical micrograph of printed PANI on interdigitated electrodes. d. A basic illustration of the PANI between the interdigitated electrodes, with the red line indicating a potential conductive pathway through connected PANI particles.

influence of these dopants on the processability, crystallinity and electrical properties of the PANI are discussed. The focus of the work presented here is on rigid glass substrates, but the ability to print onto flexible electrodes is also demonstrated.

6.2. Method

Preparation of PANI

Emeraldine base PANI (M_w avg = 50,000) (Sigma Aldrich) was weighed out and dissolved in 20 mL of 1-methyl-2-pyrrolidone (Sigma Aldrich). After complete dissolution, 5 mL aliquots of this stock solution were prepared in small glass vials. To convert the PANI from the insulating emeraldine base, to the conducting emeraldine salt, 500 µL of acid (in excess) was added to each vial, with the following concentrations: i) 250 mM HCl, ii) 1:1 mixture of 250 mM CSA and HCl, iii) 250 mM CSA. The addition of HCl caused a mildly exothermic reaction. These newly doped solutions were ultra-sonicated for 15 minutes and then sealed before use. **Caution**:

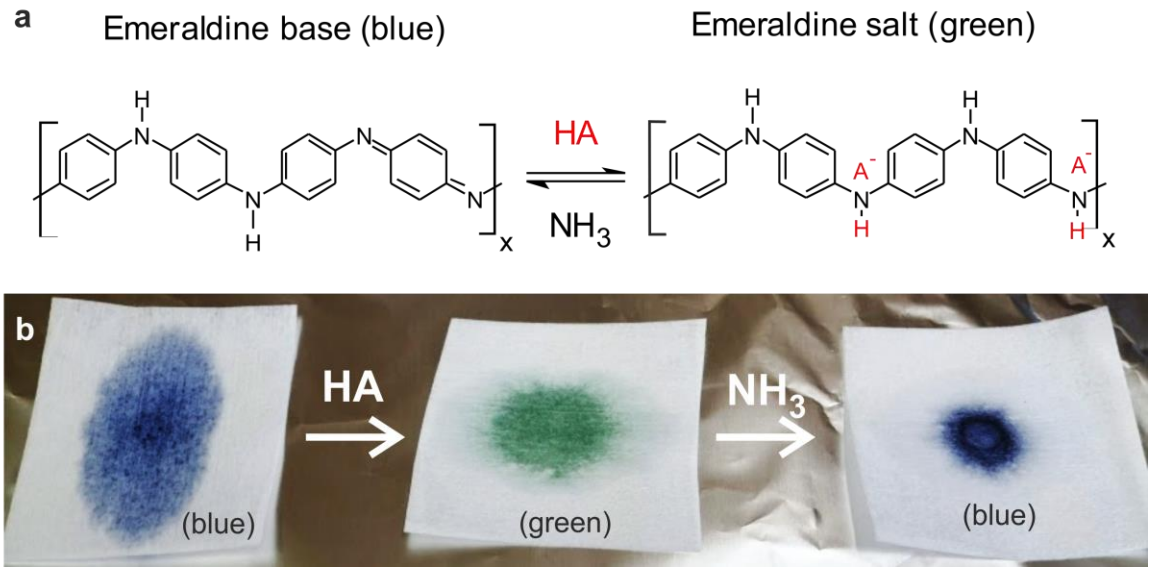

Figure 6.2. Polyaniline protonation and deprotonation. a) Protonation of Polyaniline base to salt. Here HA stands for any acid, with A being the anion. In this work, A = Cl^- and $C_{10}H_{15}O_4S^-$. b) Demonstration of the colour change from blue to green upon the addition of acid. If the emeraldine salt is further exposed to a base, it reverts back to the blue emeraldine base form. This image is illustrative, and should not be seen to be the mechanism by which the sensing in this chapter is measured.

NMP is known to be a developmental toxicant. Extreme caution must be used, and exposure minimized. The pH of each solution was determined using Hydrion pH paper. **Figure 6.2** shows the reaction scheme and the colour changes that occur.

PANI deposition

Dropcast films were prepared by casting 5 µL of PANI solution onto the interdigitated electrodes, and allowed to dry in ambient conditions. No heating was used, as acid could damage the electrodes at elevated temperatures.

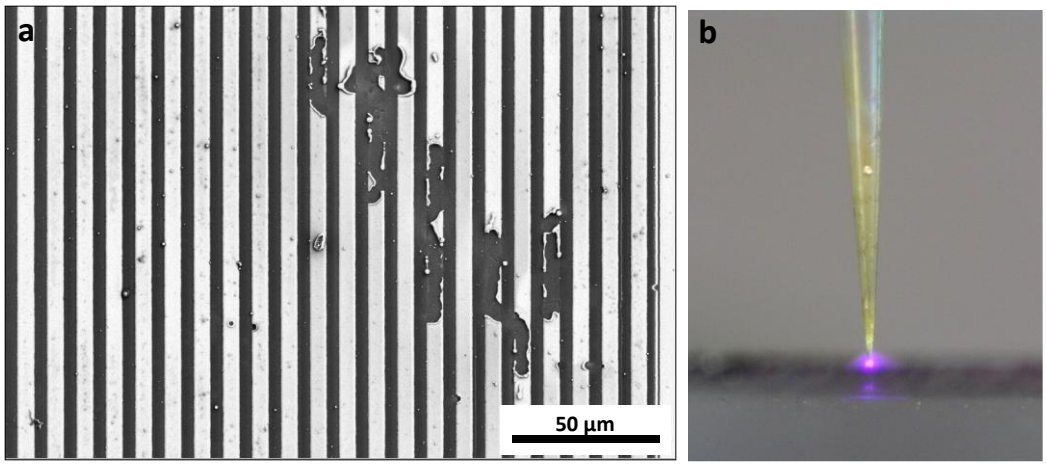

Figure 6.3. Electric discharge induced damage. If too much applied potential is applied, electric discharge can occur which results in metal delamination, as shown in the a) SEM image. The arcing event b) can be seen with the optical microscope in our setup.

Printed lines were deposited using a custom home-built EHD setup, described in chapter 3. Briefly, 50 µL doped PANI was loaded into gold coated glass capillaries (inner diameter 5 – 10 µm). Once the capillary was electrically connected to the printing setup, a sufficient bias was applied to induce printing. If an excessively large bias is applied, electric discharge may occur, which damages the electrodes (**Figure 6.3**). An electric field is created between the tip and the grounded substrate which generates sufficient electrostatic force for the ink surface tension to be overcome. Once this happens, a Taylor cone forms and continuous printing occurs. The substrate is translated in the X and Y direction remotely with motorized stages to

control where PANI is deposited. The range of voltages applied in this work were from 2 – 10 kV DC.

Ammonia sensing.

A custom built gas chamber (Appendix 2) was used for all the sensing experiments. For each sensing measurement, the sample of interest was loaded and connected electrically. The chamber was then purged with 99.9% nitrogen gas for 30 minutes. After this purge, a baseline measurement in the presence of a constant nitrogen stream was taken for 1 hour to ensure sensor stability and a good reference. If the baseline was not stable in this time, the sample was removed and prepared again. For stable samples, exposition to ammonia occurred in 5 minute exposure intervals, and then the nitrogen stream was restored to allow the sample to return to baseline readings. The current was monitored and recorded throughout this process on the BenchVue system.

Structural characterization

The morphology of the differently doped PANI was characterized and identified with different techniques. Firstly, optical images were taken of the IDEs before sensing to gain a sense of the distribution of the material (Nikon Eclipse LV100ND). Secondly, high resolution SEM images were obtained (Zeiss Merlin) for each sample to ascertain the structural information and arrangement on the IDEs. Further, a Malvern Mastersizer (Hydro 200 MU) and Nanosight LM10 were used to determine the size of the PANI particles in each dispersion. Lastly, powder XRD patterns (Bruker D500) were obtained to probe the crystallinity of each PANI sample.

6.3. Results

6.3.1. Glass substrate sensors

In the first instance, a dropcast film of hydrochloric acid (HCl) doped PANI was prepared on a glass substrate with interdigitated electrodes (**Figure 6.4a**). After drying the film in ambient conditions overnight, a sensing protocol was followed (which was subsequently used for all

measurements). First, the electrode was placed in the sensing chamber and flushed it with nitrogen gas for at least 30 minutes. After this initial flush, a 1 V potential was applied to the sample for a further 30 minutes (under nitrogen) to determine sample stability. Stability was assessed by minimal sample current fluctuation. Then a known concentration of NH_3 was introduced over a 5 minute interval. After each NH_3 pulse, the sensor was allowed to recover under a steady nitrogen environment.

The HCl doped film demonstrated poor response, evidenced by the very small change in resistance (~ 0.06%), as well as the lack of baseline recovery (**Figure 6.4a**). It was initially thought that this was due to the dopant acid. As such, a film of PANI doped with camphorsulfonic acid (CSA) was prepared. When tested, however, this film did not stabilise in the chamber, even after an hour of gassing (**Figure 6.4b**). There was a continuous increase of the resistance during the application of the 1 V bias. It was also observed that CSA doped PANI films showed a much higher resistance (by an order of magnitude) than the HCl material. If the bridging polymer shows poor conductance, this is likely to negatively impact the sensing. To counter this, a PANI blend was prepared with a 1:1 ratio of CSA and HCl as codopants. The material resembled the HCl-PANI mixture during characterization, and registered a higher resistance during measurement. As with the other two materials though, a very poor sensing result was obtained (**Figure 6.4c**), meaning that no significant change in resistance above the noise was registered when NH_3 was introduced to the system.

The hypothesis is that the poor performance observed for the film samples is a result of the large interaction volume. When NH_3 is introduced to the chamber, it will interact with the PANI surface and within the pores of the deposited layer. However, when nitrogen is used to flush the system, it is not able to completely or quickly displace the entrenched NH_3. This leads to extremely slow recovery, and undetectable changes in electrical behaviour, thus rendering films as poor sensors. This is also due to the high affinity that PANI has for NH_3.[300]

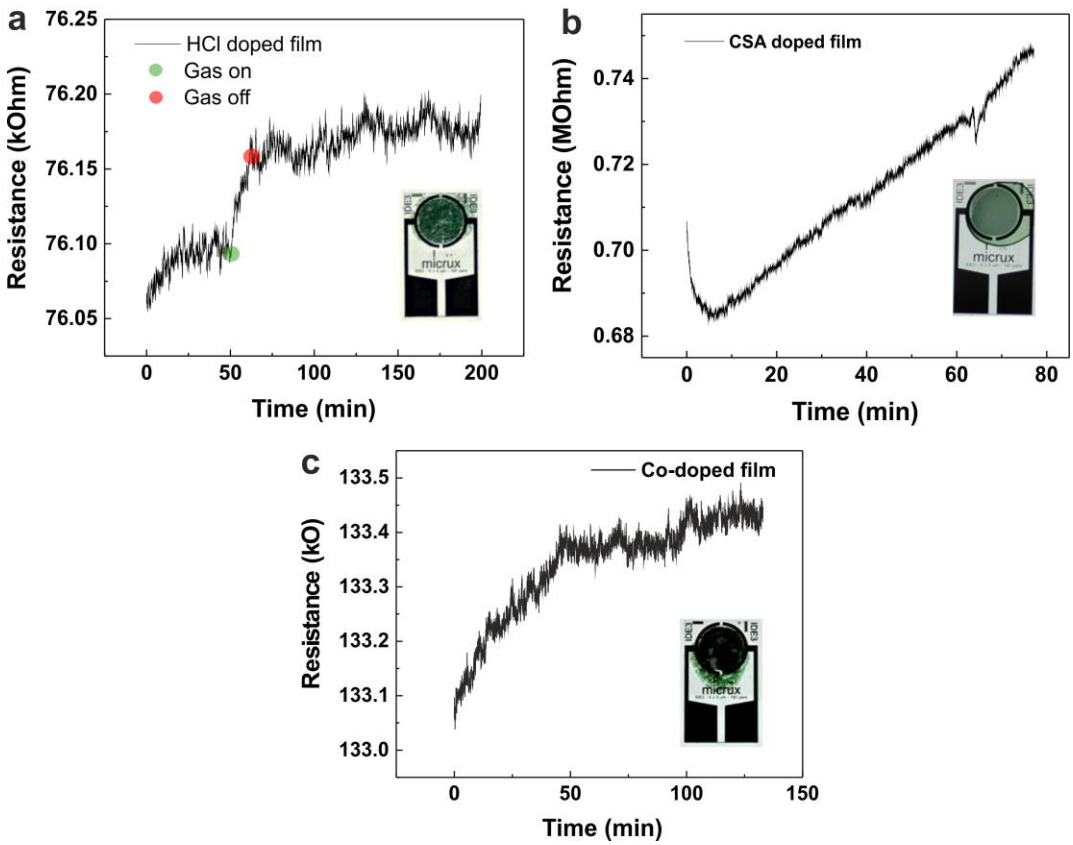

Figure 6.4. Sensing results of dropcast films on glass substrate. a) HCl doped film sensing result shows no recoverability, even with good electrical connections. b) CSA doped and c) codoped PANI have unstable baselines. Even with exposure, no change in observed. Inset images are photographs of each dropcast film on the interdigitated electrodes on glass.

SEM images of each of the films were collected. From this, it was observed that there was a distinct difference in the morphology of the PANI blends (**Figure 6.5a-c**). The HCl doped and codoped blends visually appeared to be similar, with a powder-like appearance, whereas the CSA doped blend had a more crystalline ordered character. To confirm this difference, powder XRD was performed on samples of each PANI blend. The spectra confirmed qualitatively that the CSA blend was indeed more crystalline (evidenced by more sharp peaks) than the other two blends (**Figure 6.5d**). The codoped blend, though appearing amorphous, exhibited a slight degree of crystallinity. Previous studies have demonstrated a change of PANI crystallinity dependant on solvent choice, as well as dopant acid.[321–323] Łużny and Bańka demonstrated that conductivity increases with a the degree of crystallinity.[324] However,

in this work, two different dopant acids have been used, which have different interactions with the PANI. Therefore it is not fully possible to definitively describe a relationship between crystallinity and conductivity.

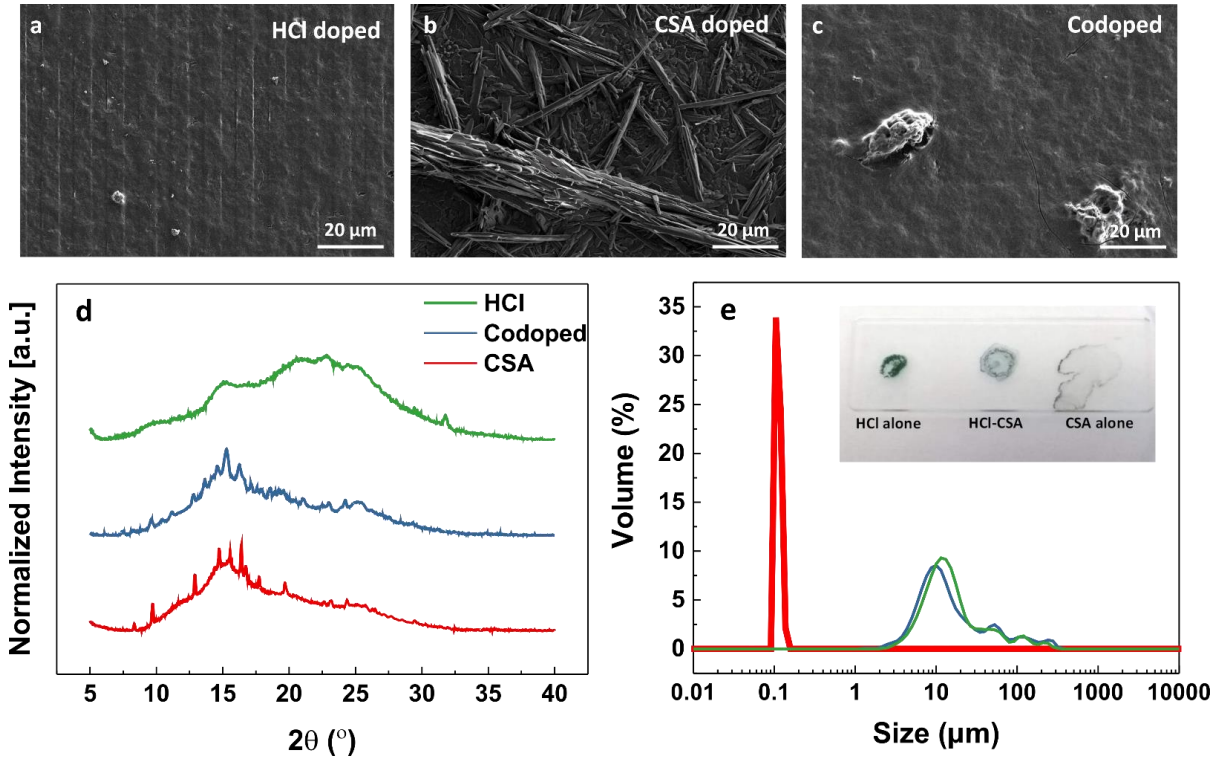

Figure 6.5. Characterization of PANI blends. SEM images of a) HCl doped, b) CSA doped and c) co-doped PANI material. d) Powder XRD spectra of differently doped PANI samples. The presence of CSA causes an increase in the crystallinity, as evidenced by the sharp crystalline peaks. e) Particle size distribution for differently doped PANI mixtures used in this study. CSA doped PANI (red) has an average particle size of 130 nm, whereas HCl doped (green) and co-doped (blue) mixtures have an average size of almost 10 µm. Inset image: Drying behaviour of PANI suspensions on glass substrate. A 10 µL drop of each suspension was deposited on a glass slide and allowed to evaporate in ambient conditions. The difference in drying behaviour is due to the particle induced surface tension.

The three PANI blends were further characterized with particle size analysis in order to understand what influence the acid anion has on particle size distribution (**Figure 6.5e**). The results reveal that the HCl-doped, and codoped PANI solutions have average particle size distributions of almost 10 µm. For the CSA doped PANI, the average size was found to be 100 nm. This significant difference in size (by two orders of magnitude) could be a reason for the

observed crystallinity, with smaller particles being better able to crystallize compared to large bulky agglomerates.

Having observed the limitations of sensing with dropcast thin films, EHD jet printing was used to pattern the PANI blends on the IDEs. Printing can offer a solution, specifically to the problem of recoverability and sensitivity, as it can print smaller volumes reliably. As the CSA doped blend was measured to have the smallest particle size (**Figure 6.5e**), it was printed first. Smaller particles were less likely to cause nozzle clogging (5 µm tip). CSA doped PANI is also known to be more processable.[325] Once prepared, this printed sensor was found to exhibit reasonable sensor behaviour (**Figure 6.6a**), characterized by proportional response to different NH_3 concentrations, as well as recovery of the original baseline (**Figure 6.6c**). The lowest detectable concentration was 200 ppb, which is considerably lower than the 25 ppm exposure limit set by the NIOSH, and lower or similar to previously reported sensors.[317] However, it was found that the recovery time between NH_3 pulses was up to 40 times longer than the exposure itself. This is a known limitation to conductive polymer sensors, which has prevented their widespread adoption commercially.

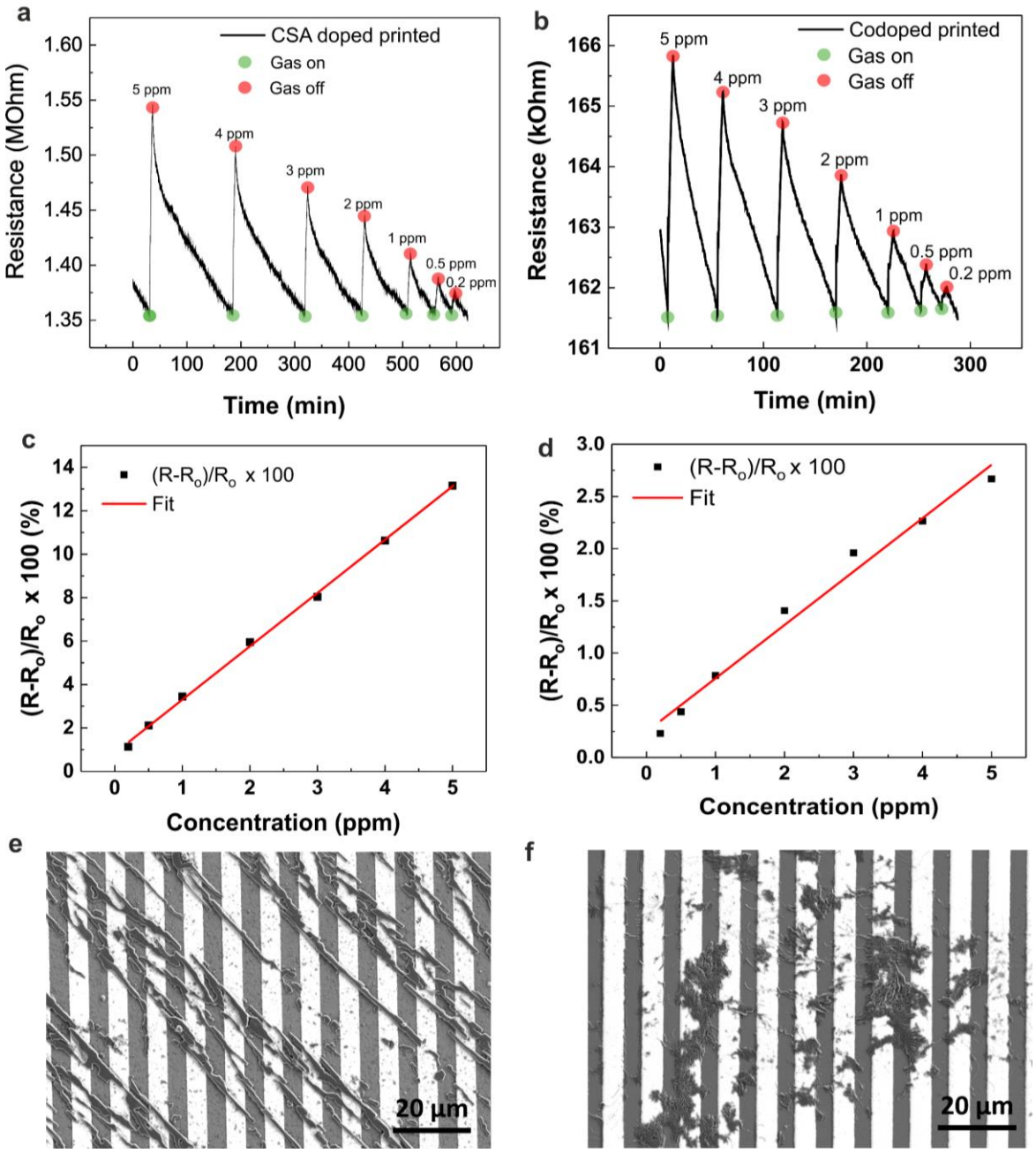

Figure 6.6. Sensing and calibration graphs for printed sensors on glass substrates. a) CSA doped PANI sensing and the corresponding c) calibration graph. e) SEM image of printed CSA doped PANI reveals the high level of connectivity between electrodes. b) Codoped PANI sensing and d) calibration graph. f) SEM shows the sparse distribution leading to poorer physical connections. Both calibrations follow a linear trend, with slight deviation, leading to the limit of detection value calculated to be different to the lowest measured NH_3 concentrations. The response of the CSA doped PANI is at least an order of magnitude greater for corresponding concentrations on the codoped PANI sensor. The sensing graphs illustrate how rapid the detection of NH_3 is with polyaniline, even for low concentrations.

To corroborate the influence of particle size, the HCl doped and codoped PANI blends were also printed. As anticipated, poor printing was obtained for the HCl blend owing to nozzle clogging. SEM revealed that tiny amounts of PANI material was deposited on the print path. Similarly, the codoped material printing was poor, however, sufficient material was deposited for sensing purposes **(Figure 6.6f**). The HCl doped PANI solution is extremely colloidal, thus two aspects dominate. Firstly, aggregation of the polymer in solution causes there to be clogging in the printing nozzle, preventing homogenous deposition. Secondly, if the material does print, after drying, the large inter-particle spacing due to poor dispersion disrupts the pathways through which current can flow. Thus, poor printing results in poor sensitivity as demonstrated in **Figure 6.7b**. Interestingly, the sensing observed with the codoped material demonstrated much better recovery times compared to the CSA doped blend for the same set of concentrations, even though the response was an order of magnitude smaller (**Figure 6.6 b,d**). The limit of detection of the functional sensors was determined to be 0.86 ppm for the codoped PANI and 0.22 ppm for the CSA doped PANI (**Table 6.1**). The discrepancy between the experimentally observed sensing of 0.2 ppm for the codoped sensor and the theoretical limit of detection (LOD) arises from the slight nonlinearity observed with the calibration plot (**Figure 6.6 c,d**). This deviation from linear behaviour changes the slope quite significantly, thus raising the value of the LOD. It is suspected the nonlinearity is due to saturation of the sensor as the concentration is raised.

Table 6.1. Limit of detection values of EHD printed sensors. The standard exposure limit is 25 ppm. The best performing sensor is the CSA doped PANI sensor on glass. The limit of detection was determined using the equation Limit of detection= (3.3 x SD)/s, where the SD and *s* are the standard deviation (at low concentrations) and the gradient of the linear regression fit, respectively.

	Substrate	HCl	Codoped	CSA
Limit of detection (ppm)	Glass IDE	n/a	0.86	0.22
	Flexible IDE	0.74	n/a	n/a

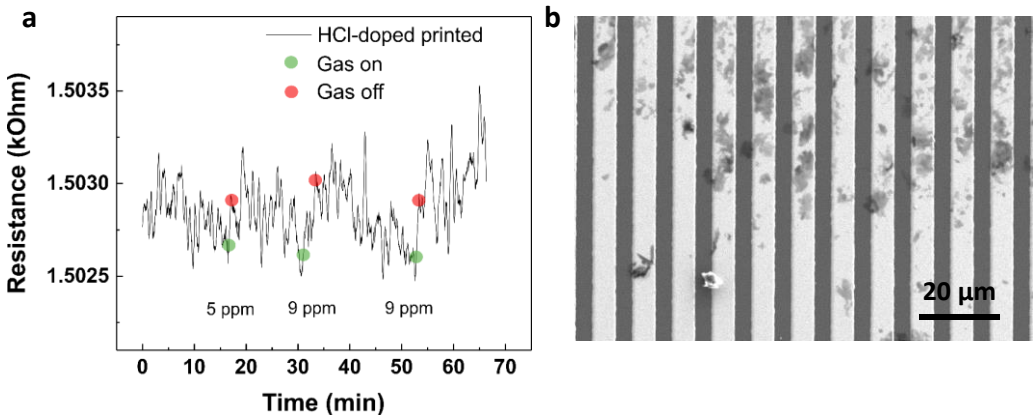

Figure 6.7. Printed HCl doped PANI sensor on glass substrate. a) Poor sensing results are obtained for this sensor, owing to the poor printing shown in b) the SE micrograph. No response was registered for any of the concentrations used.

6.3.2. Flexible substrate sensors

Having demonstrated successful sensing with printed PANI on rigid substrates, and owing to the benefits of using a versatile printing technique, flexible interdigitated electrodes were used to prepare more sensors for testing. The major difference between the rigid and flexible substrates (apart from material), is the electrode separation width. The rigid substrates have 5 µm electrodes, with the same sized gap, whereas the flexible substrates had 100 µm electrodes, with a 100 µm gap. Patterning flexible substrates with a high density of metal electrodes would lead to reduced flexibility and high propensity for strain-induced cracks or delamination, hence why larger spacing is used.

Following a similar protocol as was observed for the rigid substrates, sensing measurements were taken with dropcast films and obtained the results shown in **Figure 6.8**. I note here that all measurements were performed on sensors which had been pre-checked for conductivity before being introduced to the chamber. Any defective samples (either from poor drying, or electrode scratching) were disregarded.

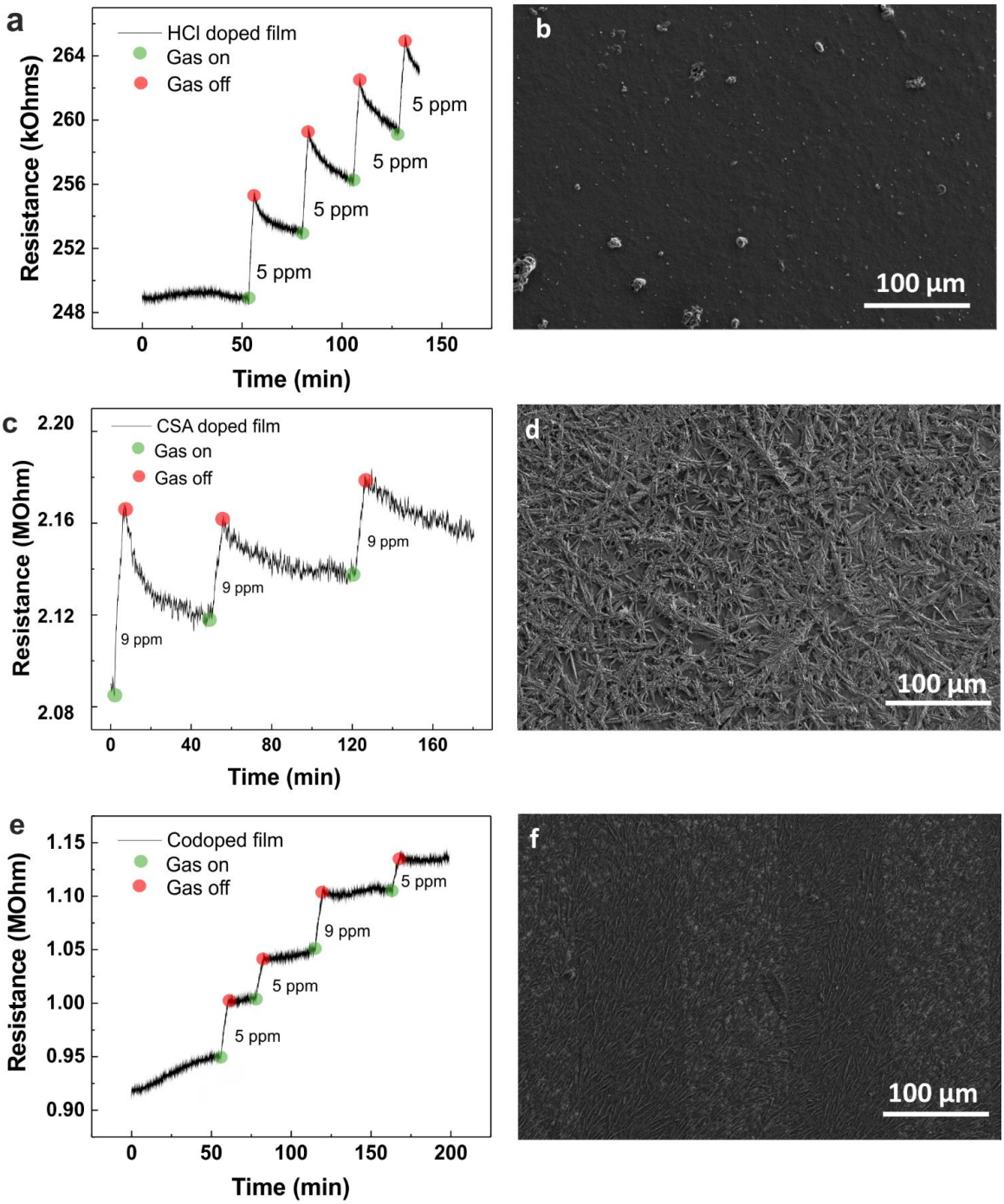

Figure 6.8. Dropcast sensing results on flexible substrates. a) HCl doped PANI. c) CSA doped PANI. e) Codoped PANI. No complete recovery was observed for any of the films in the measured time. The corresponding SEM images (b,d,f) reveal the dense arrangement and morphology of the PANI on the electrodes. If these were left for long enough, potential recovery could have occurred, however, this would render them very poor sensors.

The results show the resistances of the dropcast films as they are exposed to ammonia. For all three PANI blends, incomplete recovery of the original baseline is recorded within the measured time. It was not possible to prepare calibration plots for these films owing to the non-recovery of the sensor. As was seen for the glass substrates, the HCl doped PANI has the lowest resistance, followed by the codoped PANI and finally the CSA PANI. It is curious, nonetheless, that ammonia sensing is observed on the flexible substrates. An explanation for this is given below.

The wettability of the two substrate materials varies sufficiently that there will be a pronounced effect on droplet spreading. Further, the closeness of the electrodes (5 μm spacing) on the glass substrate compared to the size of the droplet deposited results in there being less material spreading out, owing to the droplet being pinned in place, thus preventing wicking.[285] This compounds the volume effect (i.e. thickness of PANI layer), resulting in poor sensing. On the flexible substrate, however, the larger spacing of the electrodes (100 μm) allows greater wetting, which increases the surface area, thus decreasing the interaction thickness. Secondly, the surface tension of the different solutions varies, leading to very different spreading patterns (**inset Figure 6.5e**). This is best explained by recalling the particle sizes in solution. The HCl doped PANI, with the largest particles, has a relatively large surface tension owing to the greater level of interactions between molecules (driven by H-aggregates, that is, π-π stacking). With the CSA doped material, owing to the large CSA anion, this aggregation is prevented or at least slowed down, thus reducing the magnitude of intermolecular forces, giving a lower surface tension.[326] UV-Vis measurements of the solutions reveal that the presence of HCl results in a significant peak broadening and peak red-shift of the major peaks (**Figure 6.9** and **Table 6.2**), further confirming the presence of aggregation, thus larger particles. Surprisingly, the addition of surfactant, did not change the spectral response of any of the suspensions significantly, as is observed for other conjugated π-ring systems.[327] This could be due to the acidity of the solutions themselves. A report by Manigandan *et al.* showed how the pH of a PANI solution affected the structure.[304] They

postulated that lower pH resulted in enhanced protonation, leading to charged PANI repulsion, thus allowing monodisperse particles to form. In this work, the CSA used had a pH of about 1 and the HCl between 2 and 3.

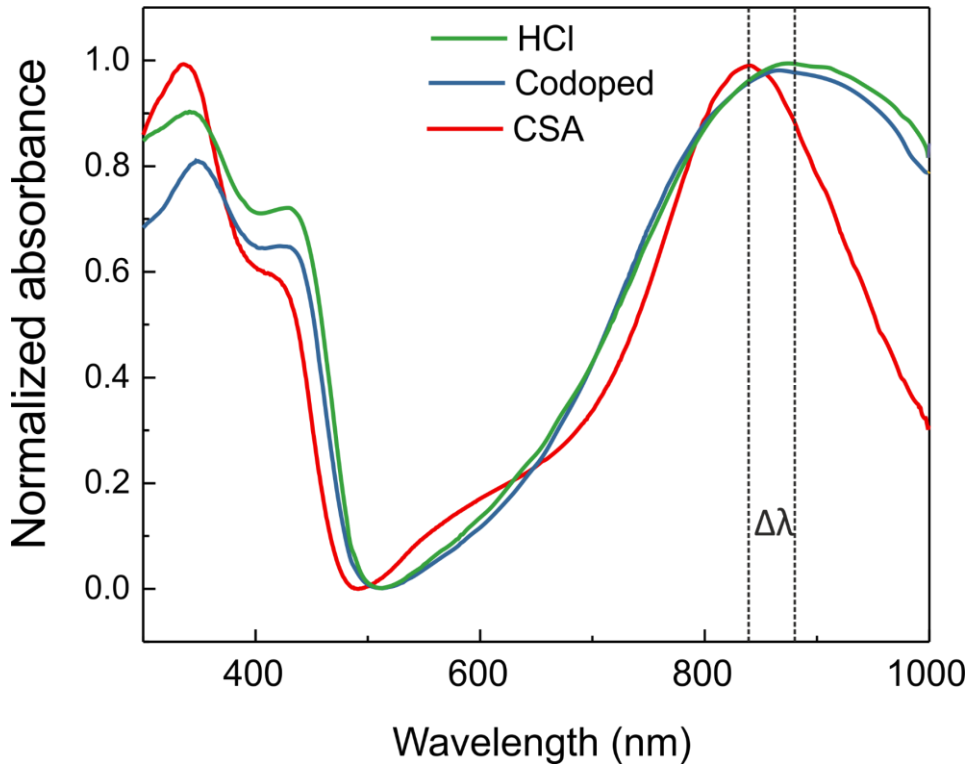

Figure 6.9. Normalized UV/Vis spectra of PANI suspensions in NMP. Both the HCl and codoped PANI suspensions exhibit a redshift and a peak broadening in the NIR region, which is indicative of a large degree of aggregation. The more pronounced shoulder peak too at ca. 420 nm is evidence of larger particles. The Δλ in the figure shows the red shift of the HCl doped and codoped blends (33 nm shift).

Table 6.2. Summary of peak UV/Vis peak positions in different acid environments, before and after addition of non-ionic surfactant (Span® 80).

	Peak position (nm)					
Ink	HCl doped	HCl doped + surfactant	CSA doped	CSA doped + surfactant	Codoped	Codoped + surfactant
Peak 1	341	337	336	337	347	345
Peak 2	416	416	410	410	416	416
Peak 3	871	871	838	834	872	872

Another issue which may dominate, is the contact resistance of the PANI with the electrodes. Hao *et al.* demonstrated that PANI on bare gold electrodes has a much higher contact resistance than that of 4-aminothiol coated gold.[328] The thin films have a much higher contact resistance than the printed lines, leading to poorer measurements being registered.

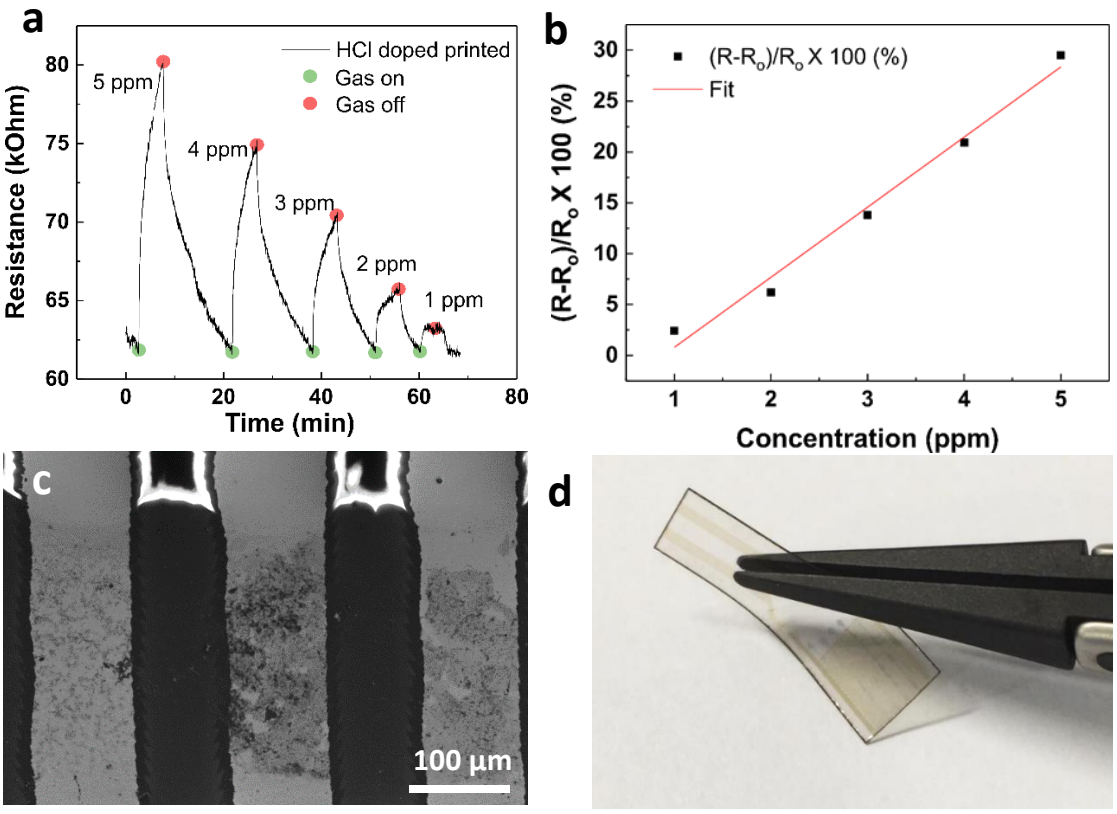

Figure 6.10. Printed HCl doped PANI on flexible substrate. a) Sensing result for printed HCl doped PANI on flexible substrate, up to 1 ppm detection. b) Calibration graph used to determine the limit of detection (0.74 ppm) for the sensor. c) SEM image of PANI on flexible substrate. There is greater accumulation of PANI on the polymer substrate rather than the electrodes. d) Photograph of flexible substrate with patterned interdigitated electrodes. The patterned PANI is bare visible owing to the

For this same reason, the sensing result of the printed PANI varies from that observed for the glass substrates. Here, the HCl doped PANI exhibits good sensing **(Figure 6.10**), judging by the fast recovery time and low levels of gas that can be detected (less than 1 ppm). Both the CSA and the codoped printed PANI on the flexible substrate gave no discernible signal

during the sensing experiment, even though SEM (**Figure 6.11**) and optical imaging confirmed that printing had occurred. Since lower solution volumes are used for printing (several picoliters), compared to the microliters used with dropcast deposition, the formation of continuous paths through which charge could flow for printed PANI on flexible substrates is less ubiquitous. In other words, there is a greater chance of there being no connections resulting in poor sensors.

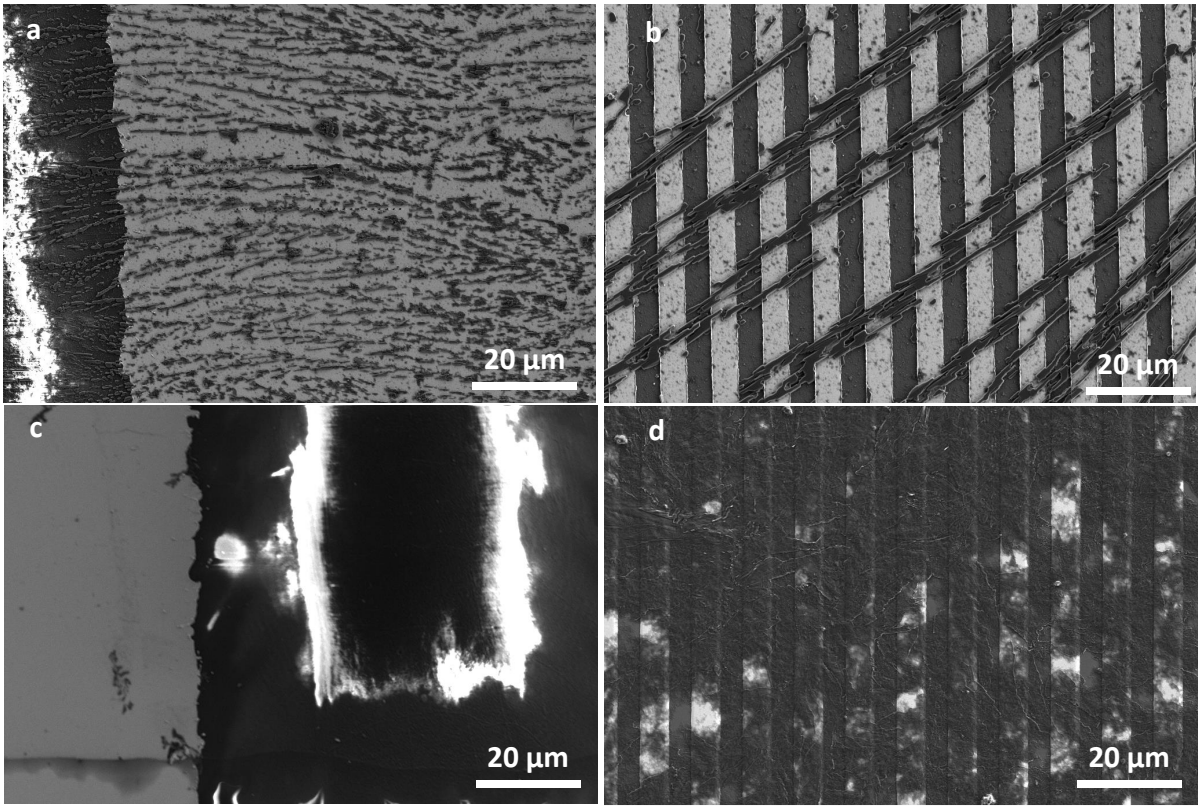

Figure 6.11. High resolution SEM images of printed CSA and codoped PANI. The connectivity of the CSA doped on a) the flexible substrate is insufficient to bridge the inter-electrode distance. There is clear electrode bridging on b) glass substrate, giving rise to detectable sensing with the same material. Similarly, with codoped PANI for the c) flexible substrate, insufficient conducting pathways exist for effect sensing, whereas on the d) glass substrate, there are.

6.4. Discussion

The printing of functional materials using EHD to make sensors has several key advantages, as I have demonstrated. Not only does it allow the sensing material to be deposited on small regions, but it also contributes to the enhancement of the sensor sensitivity. This reduction in active size has been demonstrated successfully in sensors made using electro-spun nanofibers.[317,329–331] Further, by being able to minimize the area that a functional material occupies on an electrode, it is possible to incorporate different materials to form a sensor which is sensitive to different gasses. Jiang *et al.* demonstrated a PEDOT:PSS nanowire sensor array which they fabricated using soft lithography.[332] Whilst the range of volatile organic compounds (VOCs) this sensor array was large, including various alkanes, ketones, amine, alcohols and aromatics, the fabrication process was less facile than just printing the sensor material. The sensitivity they obtained too, was less than 1.6% for all VOCs. A study by Virji *et al*. corroborates the findings of this work, that smaller regions of polyaniline perform better in terms of time response and sensitivity compared to thin films.[333] They, however, studied the difference between nanofibers and thin films.

The choice of dopant has also been revealed to be of significance in this work. Whilst having to obtain good sensing, it is also important to consider how the material will be processed, and what its chemical composition will contribute to this. Having found that the HCl doped PANI is prone to aggregation which leads to nozzle clogging, means to mitigate the effect of this on the sensing are needed. For instance, it may be best to blend HCl doped PANI with small amounts of additives such as polyvinylpyrrolidone or polyvinyl alcohol to prevent clogging and to encourage more uniform printing. However, this may come at the cost of reducing the sensitivity as the additive may block the PANI from interacting directly with the gas. More work is required to find the optimal blend, and one which is tailored for purpose.

6.5. Conclusions

In this chapter, I have successfully demonstrated the EHD printing of polyaniline chemiresistors which are able to detect ammonia. Crucially, I have demonstrated that this is a facile process which can be easily adopted in many manufacturing settings. I have demonstrated how the higher surface-to-volume ratio afforded by this additive preparation method yields improved sensing compared to drop-cast films. By tuning the acid dopant, I observed a change in particle size, crystallinity, electrical character and thus, sensing behaviour of the PANI. Both CSA doped and HCl/CSA codoped PANI exhibit sensing of up to 200 ppb on glass substrates. The solubility afforded by the CSA doping facilitates easier PANI processing, but has the drawback of rendering the polymer less conductive. However, adding a mixture of both CSA and HCl, allows for the good properties of both acids to be observed – apart from small particle size. Printing onto polymer substrates is hampered by the substrate wettability and patterned electrode geometry. However, I still demonstrate sensing of less than 1 ppm with HCl doped PANI. EHD printing promises to make the preparation of polymer sensors more successful in future.

6.6. Author Contribution

All sensing and scanning electron microscopy was performed by Dr Krishnan Murugappan. I prepared all the polyaniline blends used, prepared the sensors tested, performed UV/Vis measurements, and interpreted the results. XRD and particle size analysis were done by the Oxford Materials Characterization Service.

Chapter 7

Overall Conclusions

7.1. Key contributions

Throughout this thesis, I have introduced and demonstrated the unique ability of electrohydrodynamic jet printing as a facile additive manufacturing technique. I summarize the key contributions as follows:

1) The demonstration of high resolution template printing, using self-assembled monolayers, with a critical resolution of 300 nm obtained.
2) A fundamental study into the effects of the electric field on three common self-assembled monolayers used for surface wetting control, using both experimental and computational methods. I have shown that external electric fields realign SAM molecules, and the degree of realignment depends strongly on the dipole moment of the molecules. This was measured experimentally with Kelvin probe force microscopy and verified using Car-Parrinello Molecular Dynamics (CPMD).
3) The demonstration of how mismatched materials which give rise to anisotropic surface wrinkles can be used to control the printing resolution of EHD, when coupled with the correct system parameters. Specifically here, I have shown how the deposition of silicon dioxide onto polydimethylsiloxane substrates creates the aforementioned wrinkles. By tuning the wrinkle parameters appropriately (amplitude and wavelength), a non-wetting surface can be created.
4) The demonstration of superior ammonia sensing by the EHD printing of modified polyaniline onto both rigid (up to 200 ppb) and flexible substrates (~1 ppm). The role of the dopant acid was highlighted for its influence on ink processability and sensitivity towards the analyte

Below, I expand further on these contributions.

7.2. Overview

Micro and nanofabrication play an ever more critical role of our everyday lives. From our communication tools, to chemical sensors used to detect even very faint traces of gases, small scale functional devices permeate all aspects of life. However, their fabrication remains confined to laboratories with expensive and complex equipment.

This work was inspired by the drive towards making the fabrication process a more facile and accessible endeavour, through the use of an additive manufacturing technique. The aim was to attempt to create a reliable sub-micron printing tool, which would be able to prepare a variety of electronic, photonic, and other functional devices in a cost-effective manner. I have managed to demonstrate such a tool in the form of electrohydrodynamic (EHD) jet printing. Whilst reliable sub-micron printing has been a challenge, I have demonstrated the application of this tool to create new structures, improve existing methods and also given a new understanding to a fundamental issue which had been previously neglected.

In attempting to understand the EHD printing process, it was important to place this technology in context. Chapter 1 sought to explain existing fabrication techniques, with an emphasis on other additive manufacturing processes. The costs and advantages of each technique were assessed. I also outlined some challenges that still face the additive manufacturing realm. I concurred with previous reports that additive manufacturing does not seek to replace traditional manufacturing, but rather to provide additional means to achieve the rapid prototyping of functional devices, especially in the growing field of flexible and wearable technologies. Finally, I illustrated how EHD jet printing is poised to address many of the issues raised regarding additive manufacturing, including the hybridization with other forms of manufacturing.

In the second chapter, I outlined the parameters which are essential to the successful operation of EHD printing. I highlighted the complexity of getting the system up and running, but also provided the theory to ensure that anyone who uses EHD is able to fully grasp the

influence of the various parameters and factors. In all, I discussed the ink properties which affect printing the most, namely viscosity, conductivity, surface tension and phase. The system parameters deliberated were the nozzle diameter and geometry, flow rate, applied potential, stand-off height, operating environment, and finally the substrate properties themselves. In essence, this chapter provided a brief tutorial to the process of EHD printing.

The initial experiments with the custom EHD printer were done in order to calibrate the system, by adjusting the various parameters. They allowed for good operational knowledge of the printer. I then stated the three broad areas that this thesis would attempt to address in the subsequent chapters. These were:

- Can high speed, high resolution printing of functional inks be achieved?
- How does the electric field generated during EHD printing interact with agents used to control the wetting of surfaces on which printing is being done?
- Can EHD printing result in the improved performance of existing technologies, specifically looking at gas sensors?

Having demonstrated an operational system, I then proceeded to demonstrate EHD as a useful technique for patterning self-assembled monolayers. Compared to other techniques which are able to perform similar functions, EHD offers the advantage of being maskless, stampless and completely able to form arbitrary structures. When the correct process parameters (speed, applied potential and standoff height) are used, it is possible to obtain ~300 nm printing. The printed self-assembled monolayer [3-(aminopropyl)triethoxysilane], because of its amino-terminal group was used as a template for the assembly of 20 nm citrate capped nanoparticles. This highlights the possibility of using EHD printing as a competitive tool for patterning optoelectronic or plasmonic devices based on nanoparticles. There is great scope for process integration too.

No work had been reported on the influence of electric fields on the self-assembled monolayers used to control the surface wetting properties of substrates on which EHD is

performed. In this work, I demonstrated both experimentally and computationally the difference between surfaces before and after exposure to electric fields. This has ramifications for printing. Kelvin Force Probe Microscopy, in conjunction with contact angle measurements, was used as a means to determine the macroscopic effect of passing electric fields over self-assembled monolayers. Having observed a significant difference on the work function of the surfaces when both positive and negative fields were applied, I looked to understand this by utilizing Car-Parrinello Molecular Dynamics (CPMD) calculations. These allowed me to explore the role of the electric field on the overall dipole moment of the molecular monolayer. I found, interestingly, that the field did indeed result in a change of the conformation of the monolayer, and the degree of this change was linked to the magnitude of the dipole moment of the molecules. This is the first study to demonstrate the link between dipole displacement and a change of wetting behaviour of the surface.

I have shown how the utilization of the difference in mechanical properties of materials can result in useful outcomes. The mechanical wrinkles which form on soft elastomeric PDMS due to a thin film of different Young's modulus can be used as anisotropic physical pinning features to control the resolution of printed inks using EHD. More work is required to understand if this work to could be extended to inks of low surface tensions.

Finally, I demonstrated how EHD is able to prepare polyaniline chemiresistors. Conventional preparation methods of conductive polymer sensors suffer when it comes to the miniaturization of these devices. This is firstly due to inadequate means of depositing the material in an appropriate arrangement, and secondly from high contact resistance which arises due to low surface to volume ratios. With EHD, I have shown that it is possible to achieve a higher surface to volume ratio which leads to a reasonable level of sensitivity. Further, I experimented with the dopant acid of the polyaniline to understand its influence on the processability and electrical properties of the polymer. These have a direct impact on the sensing results. Thin films and printed lines were prepared on glass substrates with interdigitated electrodes. I found that the films did not yield any sensing, whereas the printed

lines were more responsive, with the camphorsulfonic acid (CSA) and hydrochloric acid/camphorsulfonic acid (HCl/CSA) doped lines sensing up to 200 ppb. Attempting to perform sensing on flexible substrates yielded results only for the HCl doped printed line, of up to 1 ppm. The difference in sensing results was pinned down to the different wetting properties of the substrates, as well as the influence of inter-electrode spacing. I found that the choice of dopant acid played a crucial role in the sensing ability and printing of polyaniline.

7.3. Future Work

The work demonstrated in this thesis has been an effort to further the understanding and scope of electrohydrodynamic jet printing. With the advances I have made, I realise that a lot more could be done. This section proposes future work which could follow on from the work presented in each chapter. I have already mentioned some of this in chapter 5, thus I will focus here on chapters 4 and 6.

In Chapter 4, the additive deposition of self-assembled monolayers using EHD printing opens up many avenues for the further modification of surfaces. Other than printing amino-terminated SAMs, other SAMs can be deposited for use as layers for immobilizing DNA, proteins, or other biological assays in order to create bioelectronics sensors. Work of this nature has been demonstrated using other means[334], however, EHD offers a much simplified route.

Another application which could be pursued with the method presented in chapter 4 is the plasmonic enhancement of LEDs. UV light emitted from an LED can experience enhancement by being decorated with gold nanoparticles and coupled with the plasmonic effect. This has been achieved using thin layers of metal, however this can be much more costly to achieve.[335,336] The light emitted excites the electron cloud of the nanoparticles and causes there to be a modification of the overall observed intensity, and increased quantum efficiency of the devices.

In chapter 6, EHD printing was used to demonstrate a sensor with improved performance owing to the printed sensing material having a higher surface to volume ratio. A limitation in

this work was that it was tested only in laboratory conditions. It would be ideal to test the sensitivity of the sensor for ammonia in the presence of other gases, in the open atmosphere. Further, optimizing the concentration of the printed sensing material to achieve maximum sensing is an important pursuit. This, coupled with the determination of the best solvent system, would allow for affordable sensors on flexible substrates to become more common place. Lastly, ammonia is not the only harmful gas which needs detection. Owing to the discrete patterning allowed by EHD printing, it could be possible to print multiple materials on the same sensor in order to detect and quantify different gasses such as NO_2, CO, SO_2, HCN, H_2S et cetera. This would create a versatile electronic nose, which would help in the prevention of harm to persons in hazardous environments.

References

[1] S. Okazaki, *Microelectron. Eng.* **2015**, *133*, 23.

[2] E. D. Williams, R. U. Ayres, M. Heller, *Environ. Sci. Technol.* **2002**, *36*, 5504.

[3] C. A. MacK, *IEEE Trans. Semicond. Manuf.* **2011**, *24*, 202.

[4] D. S. Engstrom, B. Porter, M. Pacios, H. Bhaskaran, *J. Mater. Res.* **2014**, *29*, 1792.

[5] P. Rodgers, *Nat. Nanotechnol.* **2009**.

[6] J. A. Liddle, G. M. Gallatin, *ACS Nano* **2016**, *10*, 2995.

[7] B. Y. Ahn, E. B. Duoss, M. J. Motala, X. Guo, S.-I. Park, Y. Xiong, J. Yoon, R. G. Nuzzo, J. A. Rogers, J. A. Lewis, *Science (80-.).* **2009**, *323*, 1590.

[8] J. Gardan, *Int. J. Prod. Res.* **2015**, *7543*, 1.

[9] O. Ivanova, C. Williams, T. Campbell, *Rapid Prototyp. J.* **2013**, *19*, 353.

[10] Y. Han, C. Wei, J. Dong, *Manuf. Lett.* **2014**, *2*, 96.

[11] T. Han, S. Kundu, A. Nag, Y. Xu, *Sensors* **2019**, *19*, 1706.

[12] A. Chiappone, E. Fantino, I. Roppolo, M. Lorusso, D. Manfredi, P. Fino, C. F. Pirri, F. Calignano, *ACS Appl. Mater. Interfaces* **2016**, *8*, 5627.

[13] D. Dean, W. Jonathan, A. Siblani, M. O. Wang, K. Kim, A. G. Mikos, J. P. Fisher, *Virtual Phys. Prototyp.* **2012**, *7*, 13.

[14] M. S. Onses, E. Sutanto, P. M. Ferreira, A. G. Alleyne, J. A. Rogers, *Small* **2015**, 4237.

[15] E. Menard, M. A. Meitl, Y. Sun, J. Park, D. J. Shir, Y. Nam, S. Jeon, J. A. Rogers, *Chem. Rev.* **2007**, *107*, 1117.

[16] S. A. M. Tofail, E. P. Koumoulos, A. Bandyopadhyay, S. Bose, L. O'Donoghue, C. Charitidis, *Mater. Today* **2018**, DOI 10.1016/j.mattod.2017.07.001.

[17] H. W. Tan, T. Tran, C. K. Chua, *Virtual Phys. Prototyp.* **2016**, *11*, 271.

[18] L. Zhou, L. Yang, M. Yu, Y. Jiang, C.-F. Liu, W.-Y. Lai, W. Huang, *ACS Appl. Mater.*

Interfaces **2017**, *9*, 40533.

[19] C. Girotto, B. P. Rand, J. Genoe, P. Heremans, *Sol. Energy Mater. Sol. Cells* **2009**, DOI 10.1016/j.solmat.2008.11.052.

[20] A. P. Quist, E. Pavlovic, S. Oscarsson, *Anal. Bioanal. Chem.* **2005**, *381*, 591.

[21] R. Zaouk, B. Y. Park, M. J. Madou, in *Methods Mol. Biol.*, **2006**, pp. 5–15.

[22] A. Kumar, H. A. Biebuyck, G. M. Whitesides, *Langmuir* **1994**, *10*, 1498.

[23] S. G. Rao, *Colloids Surfaces A Physicochem. Eng. Asp.* **2013**, *436*, 1076.

[24] K. Du, J. Ding, Y. Liu, I. Wathuthanthri, C. H. Choi, *Micromachines* **2017**, DOI 10.3390/mi8040131.

[25] R. D. Piner, J. Zhu, F. Xu, S. Hong, *Science (80-.).* **1999**, *283*, 661.

[26] C. A. Mirkin, *ACS Nano* **2007**, *1*, 79.

[27] K. Salaita, Y. Wang, C. A. Mirkin, *Nat. Nanotechnol.* **2007**, *2*, 145.

[28] K. Salaita, Y. Wang, J. Fragala, R. A. Vega, C. Liu, C. A. Mirkin, *Angew. Chemie* **2006**, *45*, 7220.

[29] Y. Zhang, C. Liu, D. Whalley, in *Int. Conf. Electron. Packag. Technol. High Density Packag.*, **2009**, pp. 497–503.

[30] V. Leblanc, J. Chen, P. Mardilovich, V. Bulovic, M. Schmidt, in *TRANSDUCERS 2007 - 2007 Int. Solid-State Sensors, Actuators Microsystems Conf.*, **2007**, pp. 121–124.

[31] J. Chen, V. Leblanc, S. H. Kang, P. J. Benning, D. Schut, M. A. Baldo, M. A. Schmidt, V. Bulović, *Adv. Funct. Mater.* **2007**, *17*, 2722.

[32] S. R. Forrest, *Nature* **2004**, *428*, 911.

[33] A. Melocchi, F. Parietti, A. Maroni, A. Foppoli, A. Gazzaniga, L. Zema, *Int. J. Pharm.* **2016**, *509*, 255.

[34] O. A. Mohamed, S. H. Masood, J. L. Bhowmik, *Adv. Manuf.* **2015**, *3*, 42.

[35] H. Bikas, P. Stavropoulos, G. Chryssolouris, *Int. J. Adv. Manuf. Technol.* **2016**, *83*, 389.

[36] W. J. Scheideler, J. Smith, I. Deckman, S. Chung, A. C. Arias, V. Subramanian, *J. Mater. Chem. C* **2016**, *4*, 3248.

[37] K. Barton, S. Mishra, A. Alleyne, P. Ferreira, J. Rogers, *Control Eng. Pract.* **2011**, *19*, 1266.

[38] J.-U. Park, M. Hardy, S. J. Kang, K. Barton, K. Adair, D. K. Mukhopadhyay, C. Y. Lee, M. S. Strano, A. G. Alleyne, J. G. Georgiadis, P. M. Ferreira, J. A. Rogers, *Nat. Mater.* **2007**, *6*, 782.

[39] J. Schneider, P. Rohner, D. Thureja, M. Schmid, P. Galliker, D. Poulikakos, *Adv. Funct. Mater.* **2015**, 833.

[40] S. Mishra, K. L. Barton, A. G. Alleyne, P. M. Ferreira, J. A. Rogers, *J. Micromechanics Microengineering* **2010**, *20*, 95026.

[41] P. Calvert, *Chem. Mater.* **2001**, *13*, 3299.

[42] J. Jiang, B. Bao, M. Li, J. Sun, C. Zhang, Y. Li, F. Li, X. Yao, Y. Song, *Adv. Mater.* **2016**, *28*, 1523.

[43] F. Torrisi, T. Hasan, W. Wu, Z. Sun, A. Lombardo, T. S. Kulmala, G. W. Hsieh, S. Jung, F. Bonaccorso, P. J. Paul, D. Chu, A. C. Ferrari, *ACS Nano* **2012**, *6*, 2992.

[44] S. Jeong, H. C. Song, W. W. Lee, Y. Choi, B.-H. Ryu, *J. Appl. Phys.* **2010**, *108*, 102805.

[45] X. Nie, H. Wang, J. Zou, *Appl. Surf. Sci.* **2012**, *261*, 554.

[46] M. Vaseem, K. M. Lee, A. R. Hong, Y. B. Hahn, *ACS Appl. Mater. Interfaces* **2012**, *4*, 3300.

[47] S. E. Burns, P. Cain, J. Mills, J. Wang, H. Sirringhaus, *MRS Bull.* **2003**, *28*, 829.

[48] E. Parry, S. Bolis, S. J. Elston, A. A. Castrej, S. M. Morris, *Adv. Eng. Mater.* **2018**, *20*, 1700774.

[49] J. Stringer, B. Derby, *J. Eur. Ceram. Soc.* **2009**, *29*, 913.

[50] C.-T. Chen, in *Featur. Liq. Cryst. Disp. Mater. Process.* (Ed.: N. Kamanina), InTech, **2011**.

[51] J. Sun, B. Bao, M. He, H. Zhou, Y. Song, *ACS Appl. Mater. Interfaces* **2015**, *7*, 28086.

[52] D. Soltman, V. Subramanian, *Langmuir* **2008**, *24*, 2224.

[53] K. Fukuda, T. Sekine, D. Kumaki, S. Tokito, *ACS Appl. Mater. Interfaces* **2013**, *5*, 3916.

[54] H. Ko, *2010 5th Int. Microsystems Packag. Assem. Circuits Technol. Conf.* **2010**, *2*, 1.

[55] A. Jaworek, A. Krupa, *J. Aerosol Sci.* **1999**, *30*, 873.

[56] P. V. Raje, N. C. Murmu, *Int. J. Emerg. Technol. Adv. Eng.* **2014**, *4*.

[57] D. P. H. Smith, *IEEE Trans. Ind. Appl.* **1986**, *IA-22*, 527.

[58] A. Gupta, A. M. Seifalian, Z. Ahmad, M. J. Edirisinghe, M. C. Winslet, *J. Bioact. Compat. Polym.* **2007**, *22*, 265.

[59] M. Enayati, M. W. Chang, F. Bragman, M. Edirisinghe, E. Stride, *Colloids Surfaces A Physicochem. Eng. Asp.* **2011**, *382*, 154.

[60] D. Wang, X. Zhao, Y. Lin, T. Ren, J. Liang, C. Liu, L. Wang, *Front. Mech. Eng.* **2017**, *12*, 477.

[61] B. H. Kim, M. S. Onses, J. Bin Lim, S. Nam, N. Oh, H. Kim, K. J. Yu, J. W. Lee, J. Kim, S. Kang, C. H. Lee, J. Lee, J. H. Shin, N. H. Kim, C. Leal, M. Shim, J. A. Rogers, **2015**, DOI 10.1021/nl503779e.

[62] J. Xie, J. Jiang, P. Davoodi, M. P. Srinivasan, C.-H. Wang, *Chem. Eng. Sci.* **2015**, *125*, 32.

[63] P. Galliker, J. Schneider, H. Eghlidi, S. Kress, V. Sandoghdar, D. Poulikakos, *Nat. Commun.* **2012**, *3*, 890.

[64] J. Zeleny, *Phys. Rev.* **1917**, *10*, 1.

[65] Lord Rayleigh, *Proc. London Math. Soc.* **1878**, 4.

[66] L. Tse, K. Barton, *Appl. Phys. Lett.* **2014**, *104*, 143510.

[67] J. Kwon, S. Hong, Y. D. Suh, J. Yeo, H.-M. So, W. S. Chang, S. H. Ko, *ECS J. Solid State Sci. Technol.* **2015**, *4*, 3052.

[68] Y. J. Jeong, H. Lee, B. S. Lee, S. Park, H. T. Yudistira, C. L. Choong, J. J. Park, C. E. Park, D. Byun, *ACS Appl. Mater. Interfaces* **2014**, *6*, 10736.

[69] M. Yu, K. H. Ahn, S. J. Lee, *Mater. Des.* **2016**, *89*, 109.

[70] C. Xiaopeng, C. Jiusheng, Y. I. N. Xiezhen, *Chinese Sicence Bull.* **2003**, *48*, 1055.

[71] J.-U. Park, J. H. Lee, U. Paik, Y. Lu, J. A. Rogers, *Nano Lett.* **2008**, *8*, 4210.

[72] W. Zou, H. Yu, P. Zhou, L. Liu, *Mater. Des.* **2019**, *166*, 107609.

[73] Y. Jang, J. Kim, D. Byun, *J. Phys. D. Appl. Phys.* **2013**, *46*, 155103.

[74] Z. L. Wang, Z. C. Kang, *Functional and Smart Materials Structural Evolution and Structure Analysis*, Plenum Publishing Corp., New York, **1998**.

[75] Y. J. Jeong, X. Lee, J. Bae, J. Jang, S. W. Joo, S. Lim, S. H. Kim, C. E. Park, *J. Mater. Chem. C* **2016**, *4*, 4912.

[76] Y. Han, C. Wei, J. Dong, *J. Manuf. Process.* **2015**, *20*, 485.

[77] C. Wei, J. Dong, *J. Micromechanics Microengineering* **2013**, *23*, 25017.

[78] J.-G. Lee, H.-J. Cho, N. Huh, C. Ko, W.-C. Lee, Y.-H. Jang, B. S. Lee, I. S. Kang, J.-W. Choi, *Biosens. Bioelectron.* **2006**, *21*, 2240.

[79] M. J. Poellmann, K. L. Barton, S. Mishra, A. J. W. Johnson, *Macromol. Biosci.* **2011**, *11*, 1164.

[80] B. H. Kim, M. S. Onses, J. Bin Lim, S. Nam, N. Oh, H. Kim, K. J. Yu, J. W. Lee, J.-H. Kim, S.-K. Kang, C. H. Lee, J. Lee, J. H. Shin, N. H. Kim, C. Leal, M. Shim, J. A. Rogers, *Nano Lett.* **2015**, *15*, 969.

[81] E. Sutanto, Y. Tan, M. S. Onses, B. T. Cunningham, A. Alleyne, *Manuf. Lett.* **2014**, *2*, 4.

[82] D. Wang, W. Zha, L. Feng, Q. Ma, X. Liu, N. Yang, *J. Micromechanics Microengineering* **2016**, *26*, 45010.

[83] C. Nothnagle, J. R. Baptist, J. Sanford, W. H. Lee, D. O. Popa, M. B. J. Wijesundara, *Proc. SPIE* **2015**, *9494*, 949403.

[84] M. M. Rehman, G. U. Siddiqui, Y. H. Doh, K. H. Choi, *Semicond. Sci. Technol.* **2017**, DOI 10.1088/1361-6641/aa77db.

[85] K. Itoh, M. Ishida, Y. Kakinuma, H. Anzai, K. Sakirai, *Smart Mater. Struct.* **2019**, DOI 10.1088/1361-665X/aafeb8.

[86] E. Sokolovskaya, J. Yoon, A. C. Misra, S. Bräse, J. Lahann, *Macromol. Rapid Commun.* **2013**, DOI 10.1002/marc.201300427.

[87] D. Wang, X. Zhao, Y. Lin, J. Liang, T. Ren, Z. Liu, J. Li, *Nanoscale* **2018**, DOI 10.1039/c8nr01001c.

[88] H. Ding, C. Zhu, L. Tian, C. Liu, G. Fu, L. Shang, Z. Gu, *ACS Appl. Mater. Interfaces* **2017**, DOI 10.1021/acsami.6b11409.

[89] X. Du, C. J. Durgan, D. J. Matthews, J. R. Motley, X. Tan, K. Pholsena, L. Árnadóttir, J. R. Castle, P. G. Jacobs, R. S. Cargill, W. K. Ward, J. F. Conley, G. S. Herman, *ECS J. Solid State Sci. Technol.* **2015**, DOI 10.1149/2.0101504jss.

[90] A. Kumar, *Manuf. Lett.* **2018**, *15*, 122.

[91] B. D. Gates, *Science (80-.).* **2009**, *323*, 1566.

[92] A. Sugimoto, H. Ochi, S. Fujimura, A. Yoshida, T. Miyadera, M. Tsuchida, *IEEE J. Sel. Top. Quantum Electron.* **2004**, *10*, 107.

[93] A. California, A. S. Silva, J. Goncalves, A. Branco, C. Pinheiro, C. Costa, *Sol. Energy Mater. Sol. Cells* **2016**, *153*, 61.

[94] J. A. Rogers, T. Someya, Y. Huang, *Science (80-.).* **2010**, *327*, 1603.

[95] C. Ru, J. Luo, S. Xie, Y. Sun, **2014**, DOI 10.1088/0960-1317/24/5/053001.

[96] G. Kim, Electrohydrodynamic Inkjet Printing of OLED Pixel Patterns with High Resolutions, Ulsan National Institute of Science and Technology, **2013**.

[97] P. Richner, S. J. P. Kress, D. Norris, D. Poulikakos, *Nanoscale* **2016**, *8*, 6028.

[98] H. Semat, R. Katz, in *Physics (College. Park. Md).*, Robert Katz Publications, Lincoln, **1958**, pp. 524–538.

[99] A. Khan, K. Rahman, D. S. Kim, K. H. Choi, *J. Mater. Process. Technol.* **2012**, *212*,

700.

[100] G. Taylor, *Proceeds R. Soc. London A* **1969**, *313*, 453.

[101] J. J. Feng, *Phys. Fluids* **2002**, *14*, 3912.

[102] A. V Subbotin, A. N. Semenov, *Proc. R. Soc. A* **2015**, 290.

[103] I. Hayati, A. I. Bailey, T. F. Tadros, *Nature* **1986**, *319*, 41.

[104] K. Rahman, A. Khan, N. M. Muhammad, J. Jo, K.-H. Choi, *J. Micromechanics Microengineering* **2012**, *22*, 65012.

[105] Y. Han, J. Dong, *Procedia Manuf.* **2017**, *10*, 845.

[106] J. He, F. Xu, Y. Cao, Y. Liu, D. Li, Z. Jin, *Appl. Phys. Lett.* **2014**, *105*, 253109.

[107] J. Kietzmann, L. Pitt, P. Berthon, *Bus. Horiz.* **2015**, *58*, 209.

[108] M. M. Hohman, M. Shin, G. Rutledge, M. P. Brenner, *Phys. Fluids* **2001**, *13*, 2201.

[109] E. Castillo-Orozco, A. Kar, R. Kumar, *Sci. Rep.* **2017**, *7*, 1.

[110] P. Sammons, S. Bollineni, R. Sibal, K. Barton, *Solid Free. Fabr. Symp.* **2017**, 1784.

[111] R. Sridhar, R. Lakshminarayanan, K. Madhaiyan, V. Amutha Barathi, K. H. C. Lim, S. Ramakrishna, *Chem. Soc. Rev.* **2015**, *44*, 790.

[112] A. Lee, H. Jin, H. W. Dang, K. H. Choi, K. H. Ahn, *Langmuir* **2013**, *29*, 13630.

[113] A. Barrero, A. M. Ganan-Calvo, J. Davilla, A. Palacios, E. Gomez - Gonzalez, *J. Electrostat.* **1999**, *47*, 13.

[114] A. Barrero, I. G. Loscertales, *Annu. Rev. Fluid Mech.* **2007**, *39*, 89.

[115] H. K. Choi, J. U. Park, O. O. Park, P. M. Ferreira, J. G. Georgiadis, J. A. Rogers, *Appl. Phys. Lett.* **2008**, *92*, 3.

[116] L. Hirt, A. Reiser, R. Spolenak, T. Zambelli, *Adv. Mater.* **2017**, *29*, DOI 10.1002/adma.201604211.

[117] B. Zhang, J. He, X. Li, F. Xu, D. Li, *Nanoscale* **2016**, *8*, 15376.

[118] B. R. Ringeisen, C. M. Othon, J. A. Barron, D. Young, B. J. Spargo, *Biotechnol. J.* **2006**, *1*, 930.

[119] Y. Wu, Y. Han, Y. S. Wong, J. Y. H. Fuh, *J. Tissue Eng. Regen. Med.* **2018**, *12*, 1798.

[120] M. Mao, J. He, X. Li, B. Zhang, Q. Lei, Y. Liu, D. Li, *Micromachines* **2017**, *8*, 1.

[121] I. M. Hutchings, G. D. Martin, S. D. Hoath, in *Fundam. Inkjet Print.* (Ed.: S.D. Hoath), WILEY-VCH Verlag, Weinheim, **2016**, pp. 1–12.

[122] M. R. Morad, A. Rajabi, M. Razavi, S. R. P. Sereshkeh, *Sci. Rep.* **2016**, *6*, 38509.

[123] B. He, S. Yang, Z. Qin, B. Wen, C. Zhang, *Sci. Rep.* **2017**, *7*, 1.

[124] S. Lim, S. H. Park, T. K. An, H. S. Lee, S. H. Kim, *RSC Adv.* **2016**, *6*, 2004.

[125] C. H. Chen, D. A. Seville, I. A. Aksay, *Appl. Phys. Lett.* **2006**, *89*, 124103.

[126] S. Palmer, *Phys. Educ.* **1976**, 119.

[127] J. S. Rowlinson, B. Widom, *Molecular Theory of Capillarity*, Clarendon Press, Oxford, **1982**.

[128] M. M. Laurila, B. Khorramdel, A. Dastpak, M. Mäntysalo, *J. Micromechanics Microengineering* **2017**, *27*, DOI 10.1088/1361-6439/aa7a71.

[129] D. S. Pillai, P. Narayanan, S. Pushpavanam, T. Sundararajan, A. Jasmin Sudha, P. Chellapandi, *Phys. Fluids* **2012**, *24*, DOI 10.1063/1.4772974.

[130] T. Kien Nguyen, V. D. Nguyen, B. Seong, N. Hoang, J. Park, D. Byun, *J. Aerosol Sci.* **2014**, *71*, 29.

[131] D. A. Saville, *Annu. Rev. Fluid Mech.* **1997**, *29*, 27.

[132] L. Xie, M. Mäntysalo, A. L. Cabezas, Y. Feng, F. Jonsson, L. R. Zheng, *Mater. Lett.* **2012**, *88*, 68.

[133] J. Perelaer, C. E. Hendriks, A. W. M. De Laat, U. S. Schubert, *Nanotechnology* **2009**, *20*, 18.

[134] J. Perelaer, B.-J. de Gans, U. S. Schubert, *Adv. Mater.* **2006**, *18*, 2101.

[135] X. Li, Y. J. Jeong, J. Jang, S. Lim, S. H. Kim, *Phys. Chem. Chem. Phys.* **2018**, *20*,

1210.

[136] L. Dong, D. Johnson, *Langmuir* **2003**, *19*, 10205.

[137] S. Korkut, D. A. Saville, I. A. Aksay, *Langmuir* **2008**, *24*, 12196.

[138] H. Lee, K. Chou, K. Huang, **2005**, DOI 10.1088/0957-4484/16/10/074.

[139] B. Zhang, B. Seong, J. Lee, V. Nguyen, D. Cho, D. Byun, *ACS Appl. Mater. Interfaces* **2017**, *9*, 29965.

[140] J. Park, J. Moon, **2006**, 3506.

[141] Q. Lei, J. He, B. Zhang, J. Chang, D. Li, *J. Mater. Chem. C* **2018**, *6*, 213.

[142] S. B. Walker, J. A. Lewis, *J. Am. Chem. Soc.* **2012**, *134*, 1419.

[143] Y. H. Lin, *Polymer Viscoelasticity: Basics, Molecular Theories, Experiments and Simulations 2nd Edition*, World Scientific, Singapore, **2010**.

[144] Y. Tsori, F. Tournilhac, L. Leibler, F. Ho, *Nature* **2004**, *430*, 544.

[145] C. Wei, J. Dong, *J. Manuf. Sci. Eng.* **2014**, *136*, 61010.

[146] S. An, M. W. Lee, N. Y. Kim, C. Lee, S. S. Al-Deyab, S. C. James, S. S. Yoon, *Appl. Phys. Lett.* **2014**, *105*, 214102.

[147] H. B. Zhang, M. J. Edirisinghe, S. N. Jayasinghe, *J. Fluid Mech.* **2006**, *558*, 103.

[148] S. N. Jayasinghe, M. J. Edirisinghe, *J. Aerosol Sci.* **2002**, *33*, 1379.

[149] W. J. Scheideler, C. Chen, *Appl. Phys. Lett.* **2014**, *104*, 24103.

[150] X. Jin, Y. Lo Hsieh, *Polymer (Guildf).* **2005**, *46*, 5149.

[151] Y. Cao, J. Qiu, P. Smith, *Synt. Met.* **1995**, *69*, 187.

[152] H. Zhao, Z. Liang, F. Li, *J. Mol. Liq.* **2009**, *149*, 55.

[153] L. Dai, in *Intell. Macromol. Smart Devices*, Springer-Verlag, London, **2004**, pp. 41–80.

[154] X. X. He, J. Zheng, G. F. Yu, M. H. You, M. Yu, X. Ning, Y. Z. Long, *J. Phys. Chem. C* **2017**, *121*, 8663.

[155] M. Vosgueritchian, D. J. Lipomi, Z. Bao, *Adv. Funct. Mater.* **2012**, *22*, 421.

[156] I. Hayati, a Bailey, T. . Tadros, *J. Colloid Interface Sci.* **1987**, *117*, 222.

[157] R. L. Truby, J. A. Lewis, *Nature* **2016**, *540*, 371.

[158] Y. Jang, H. Tambunan, H. Tak, V. D. Nguyen, *Appl. Phys. Lett.* **2015**, *123901*, 123901.

[159] T. H. Phung, S. Kim, K. Kwon, *J. Micromechanics Microengineering* **2017**, *27*, 95003.

[160] K.-H. Choi, K. Ali, K. Rahman, *Chinese J. Phys.* **2014**, *52*, 799.

[161] M. J. Edirisinghe, S. N. Jayasinghe, *Int. J. Appl. Ceram. Technol.* **2004**, *1*, 140.

[162] I. Hayati, A. Bailey, T. F. Tadros, *J. Colloid Interface Sci.* **1987**, *117*, 222.

[163] S. Zhang, N. Sun, X. He, X. Lu, X. Zhang, *J. Phys. Chem. Ref. Data* **2006**, *35*, 1475.

[164] K. D. Sweely, E. T. Fox, E. K. Brown, L. M. Haverhals, H. C. De Long, P. C. Trulove, *ECS Trans.* **2014**, *64*, 575.

[165] D. H. A. T. Gunasekera, S. Kuek, D. Hasanaj, Y. He, C. Tuck, A. Croft, R. D. Wildman, *Faraday Discuss.* **2016**, DOI 10.1039/C5FD00219B.

[166] E. Sutanto, K. Shigeta, Y. K. Kim, P. G. Graf, D. J. Hoelzle, K. L. Barton, a G. Alleyne, P. M. Ferreira, J. a Rogers, *J. Micromechanics Microengineering* **2012**, *22*, 45008.

[167] H. K. Bisoyi, S. Kumar, *Chem. Soc. Rev.* **2011**, *40*, 306.

[168] S. Yilmaz, *J. Mod. Phys.* **2011**, *2*, 248.

[169] S.-U. Byun, H.-G. Park, K.-I. Lee, B.-J. Lim, H.-J. Lee, D.-S. Seo, *Electrochem. Solid-State Lett.* **2012**, *15*, J28.

[170] U. Stachewicz, J. F. Dijksman, D. Burdinski, C. U. Yurteri, J. C. M. Marijnissen, *Langmuir* **2009**, *25*, 11975.

[171] H. Nie, Z. Dong, D. Y. Arifin, Y. Hu, C. H. Wang, *J. Biomed. Mater. Res. - Part A* **2010**, *95*, 709.

[172] S. Zhao, P. Agarwal, W. Rao, H. Huang, R. Zhang, Z. Liu, J. Yu, N. Weisleder, W.

Zhang, X. He, *Integr. Biol. (United Kingdom)* **2014**, *6*, 874.

[173] P. J. T. Reardon, M. Parhizkar, J. Browning, V. Vassileva, B. Pedley, M. Edirisinghe, J. C. Knowles, *Int. J. Nanomedicine* **2017**, *12*, 12.

[174] A. Mickova, M. Buzgo, O. Benada, M. Rampichova, Z. Fisar, E. Filova, M. Tesarova, D. Lukas, E. Amler, *Biomacromolecules* **2012**, *13*, 952.

[175] B. S. Lee, S. Y. Jeon, H. Park, G. Lee, H. S. Yang, W. R. Yu, *Sci. Rep.* **2014**, *4*, DOI 10.1038/srep06758.

[176] Z. Ahmad, H. B. Zhang, U. Farook, M. Edirisinghe, E. Stride, P. Colombo, *J. R. Soc. Interface* **2008**, *5*, 1255.

[177] A. M. Gañán-Calvo, J. M. López-Herrera, M. A. Herrada, A. Ramos, J. M. Montanero, *J. Aerosol Sci.* **2018**, 1.

[178] L. Zhang, J. Huang, T. Si, R. X. Xu, *Expert Rev. Med. Devices* **2012**, *9*, 595.

[179] J. S. Lee, S. Y. Kim, Y. J. Kim, J. Park, Y. Kim, J. Hwang, Y. J. Kim, *Appl. Phys. Lett.* **2008**, *93*, DOI 10.1063/1.3049609.

[180] J. Kim, H. Oh, S. S. Kim, *J. Aerosol Sci.* **2008**, *39*, 819.

[181] J. Chang, J. He, Q. Lei, D. Li, *ACS Appl. Mater. Interfaces* **2018**, *10*, 19116.

[182] T. H. Phung, S. Kim, K. S. Kwon, *J. Micromechanics Microengineering* **2017**, *27*, DOI 10.1088/1361-6439/aa7c6b.

[183] T. Phung, L. Nguyen, K.-S. Kwon, *Appl. Sci.* **2018**, *8*, 351.

[184] T. H. Phung, S. Oh, K.-S. Kwon, *J. Vis. Exp.* **2018**, 1.

[185] C. Wei, H. Qin, N. a Ramírez-Iglesias, C.-P. Chiu, Y. Lee, J. Dong, *J. Micromechanics Microengineering* **2014**, *24*, 45010.

[186] C. Wei, H. Qin, C. P. Chiu, Y. S. Lee, J. Dong, *J. Manuf. Syst.* **2015**, *37*, 505.

[187] B. Bao, J. Sun, M. Gao, X. Zhang, L. Jiang, Y. Song, *Nanoscale* **2016**, *8*, 9556.

[188] S. Ajuria-Garza, *J. Chem. Educ.* **1972**, *49*, 706.

[189] M. Ma, R. M. Hill, *Current* **2006**, *11*, 193.

[190] J. Wang, M. Do-Quang, J. J. Cannon, F. Yue, Y. Suzuki, G. Amberg, J. Shiomi, *Sci. Rep.* **2014**, *5*, 1.

[191] N. Gao, Y. Yan, *Nanoscale* **2012**, *4*, 2202.

[192] C. Sun, X. W. Zhao, Y. H. Han, Z. Z. Gu, *Thin Solid Films* **2008**, *516*, 4059.

[193] P. C. Lin, S. Yang, *Soft Matter* **2009**, *5*, 1011.

[194] X. Zhang, F. Shi, J. Niu, Y. Jiang, Z. Wang, *J. Mater. Chem.* **2008**, *18*, 621.

[195] N. Bin Bu, Y. A. Huang, Z. P. Yin, *Adv. Mater. Res.* **2013**, *684*, 352.

[196] K. Barton, S. Mishra, K. Alex Shorter, A. Alleyne, P. Ferreira, J. Rogers, *Mechatronics* **2010**, *20*, 611.

[197] K. Shigeta, Y. He, E. Sutanto, S. Kang, A. P. Le, R. G. Nuzzo, A. G. Alleyne, P. M. Ferreira, Y. Lu, J. a. Rogers, *Anal. Chem.* **2012**, *84*, 10012.

[198] C. Wu, H. Tetik, J. Cheng, W. Ding, H. Guo, X. Tao, N. Zhou, Y. Zi, Z. Wu, H. Wu, D. Lin, Z. L. Wang, *Adv. Funct. Mater.* **2019**, 1901102.

[199] T. Holz, “Surface tension values of some common test liquids for surface energy analysis,” can be found under http://www.surface-tension.de/, **2017**.

[200] R. K. Smith, P. A. Lewis, P. S. Weiss, *Prog. Surf. Sci.* **2004**, *75*, 1.

[201] G. Schmid, U. Simon, *Chem. Commun.* **2005**, 697.

[202] B. F. Porter, Rapid , Electrostatic Self-Assembly of Nanoparticles with Kelvin Probe Characterisation, University of Oxford, **2015**.

[203] I. Smallwood, *Handbook of Organic Solvent Properties*, Arnold, London, **1996**.

[204] A. A. Mewe, E. S. Kooij, B. Poelsema, *Langmuir* **2006**, 5584.

[205] T. H. Hwang, Y. J. Kim, H. Chung, W. H. Ryu, *Microelectron. Eng.* **2016**, *161*, 43.

[206] M. Altissimo, *Biomicrofluidics* **2010**, *4*, DOI 10.1063/1.3437589.

[207] J. Geerlings, E. Sarajlic, E. J. W. Berenschot, R. G. P. Sanders, M. H. Siekman, L. Abelmann, N. R. Tas, *Appl. Phys. Lett.* **2015**, *107*, 1.

[208] K. Kaisei, N. Satoh, K. Kobayashi, K. Matsushige, H. Yamada, *Nanotechnology* **2011**, *22*, 175301.

[209] J. Kane, M. Inan, R. F. Saraf, *ACS Nano* **2010**, *4*, 317.

[210] H. Moreira, J. Grisolia, N. M. Sangeetha, N. Decorde, C. Farcau, B. Viallet, K. Chen, G. Viau, L. Ressier, *Nanotechnology* **2013**, 95701.

[211] E. Ertorer, J. C. Avery, L. C. Pavelka, S. Mittler, *Chem. Vap. Depos.* **2013**, *19*, 338.

[212] X. Rao, C. Guyon, S. Ognier, B. Da Silva, C. Chu, M. Tatoulian, A. A. Hassan, *Appl. Surf. Sci.* **2018**, *439*, 272.

[213] M. Pelton, J. Aizpurua, G. Bryant, *Laser Photon. Rev.* **2008**, *159*, 136.

[214] W. Ahn, Y. Hong, S. V Boriskina, *ACS Nano* **2013**, 4470.

[215] S. Onclin, B. J. Ravoo, D. N. Reinhoudt, *Angew. Chemie - Int. Ed.* **2005**, *44*, 6282.

[216] G. Heimel, L. Romaner, E. Zojer, J. L. Bredas, *Acc. Chem. Res.* **2008**, *41*, 721.

[217] P. G. De Gennes, *Rev. Mod. Phys.* **1985**, *57*, 827.

[218] W. A. Zisman, in *Contact Angle, Wettability, Adhes.* (Ed.: F.M. Fowkes), American Chemical Society, Washington, DC, **1964**, pp. 1–51.

[219] M. A. Rampi, O. J. A. Schueller, G. M. Whitesides, M. A. Rampi, *Appl. Phys. Lett.* **1998**, *72*, 1781.

[220] R. Haag, M. A. Rampi, R. E. Holmlin, G. M. Whitesides, *J. Am. Chem. Soc.* **1999**, *121*, 7895.

[221] D. J. Wold, R. Haag, M. A. Rampi, C. D. Frisbie, *J. Phys. Chem. B* **2002**, *106*, 2813.

[222] R. E. Holmlin, R. Haag, M. L. Chabinyc, R. F. Ismagilov, A. E. Cohen, A. Terfort, M. A. Rampi, G. M. Whitesides, *J. Am. Chem. Soc.* **2001**, *123*, 5075.

[223] H. Rahman, J. Ryall, J. J. Davis, P. R. Bueno, *Langmuir* **2012**, *28*, 9689.

[224] I. Campbell, S. Rubin, T. Zawodzinski, J. Kress, R. Martin, D. Smith, N. Barashkov, J. Ferraris, *Phys. Rev. B* **1996**, *54*, 14321.

[225] M. Novak, C. M. Jager, A. Rumpel, H. Kropp, W. Peukert, T. Clark, M. Halik, *Org.*

Electron. physics, Mater. Appl. **2010**, *11*, 1476.

[226] R. Haag, M. A. Rampi, R. E. Holmlin, G. M. Whitesides, *J. Am. Chem. Soc.* **1999**, 7895.

[227] S. Casalini, C. A. Bortolotti, F. Leonardi, F. Biscarini, *Chem. Soc. Rev.* **2017**, *46*, 40.

[228] I. H. Campbell, J. D. Kress, R. L. Martin, D. L. Smith, N. N. Barashkov, J. P. Ferraris, *Appl. Phys. Lett.* **1997**, *71*, 3528.

[229] A. Jedaa, M. Burkhardt, U. Zschieschang, H. Klauk, D. Habich, G. Schmid, M. Halik, *Org. Electron. physics, Mater. Appl.* **2009**, *10*, 1442.

[230] A. Jedaa, M. Salinas, C. M. Jäger, T. Clark, A. Ebel, A. Hirsch, M. Halik, *Appl. Phys. Lett.* **2012**, *100*, DOI 10.1063/1.3682301.

[231] H. Bedis, *J. Surf. Eng. Mater. Adv. Technol.* **2011**, *1*, 42.

[232] J. C. Love, L. A. Estroff, J. K. Kriebel, R. G. Nuzzo, G. M. Whitesides, *Self-Assembled Monolayers of Thiolates on Metals as a Form of Nanotechnology*, **2005**.

[233] Y. Zhang, X. Qiu, P. Gordiichuk, S. Soni, T. L. Krijger, A. Herrmann, R. C. Chiechi, *J. Phys. Chem. C* **2017**, *121*, 14920.

[234] J. Lü, E. Delamarche, L. Eng, R. Bennewitz, E. Meyer, H. J. Güntherodt, *Langmuir* **1999**, *15*, 8184.

[235] K. Hayashi, N. Saito, H. Sugimura, O. Takai, N. Nakagiri, *Langmuir* **2002**, *18*, 7469.

[236] S. D. Evans, E. Urankar, A. Ulman, N. Ferris, *J. Am. Chem. Soc.* **1991**, *113*, 4121.

[237] S. P. Pujari, L. Scheres, A. T. M. Marcelis, H. Zuilhof, *Angew. Chemie* **2014**, *53*, 6322.

[238] D. K. Aswal, S. Lenfant, D. Guerin, J. V. Yakhmi, D. Vuillaume, *Anal. Chim. Acta* **2006**, *568*, 84.

[239] Y. Yang, A. M. Bittner, S. Baldelli, K. Kern, *Thin Solid Films* **2008**, *516*, 3948.

[240] A. Kumar, H. A. Biebuyck, G. M. Whitesides, *Langmuir* **1994**, *10*, 1498.

[241] M. D. Porter, T. B. Bright, D. L. Allara, C. E. D. Chidsey, *J. Am. Chem. Soc.* **1987**, *109*, 3559.

[242] T. Manifar, A. Rezaee, M. Sheikhzadeh, S. Mittler, *Appl. Surf. Sci.* **2008**, *254*, 4611.

[243] N. Rozlosnik, M. C. Gerstenberg, N. B. Larsen, *Langmuir* **2003**, *214*, 1182.

[244] X. Zeng, G. Xu, Y. Gao, Y. An, **2010**, 450.

[245] J. F. Martínez Hardigree, T. J. Dawidczyk, R. M. Ireland, G. L. Johns, B. J. Jung, M. Nyman, R. Österbacka, N. Marković, H. E. Katz, *ACS Appl. Mater. Interfaces* **2013**, *5*, 7025.

[246] B. F. Porter, M. Pacios, H. Bhaskaran, *ArXiv e-prints* **2017**, 1.

[247] J. M. R. Weaver, D. W. Abraham, *J. Vac. Sci. Technol. B Microelectron. Nanom. Struct.* **1991**, *9*, 1559.

[248] G. Y. Liu, S. Xu, Y. Qian, *Acc. Chem. Res.* **2000**, *33*, 457.

[249] D. J. Wold, C. D. Frisbie, *J. Am. Chem. Soc.* **2000**, *122*, 2970.

[250] W. Melitz, J. Shen, A. C. Kummel, S. Lee, *Surf. Sci. Rep.* **2011**, *66*, 1.

[251] S. Suzuki, C. Bower, Y. Watanabe, O. Zhou, *Appl. Phys. Lett.* **2000**, *76*, 4007.

[252] O. Zenasni, A. C. Jamison, T. R. Lee, *Soft Matter* **2013**, *9*, 6356.

[253] G. M. Ku, E. Lee, B. Kang, J. H. Lee, K. Cho, W. H. Lee, *RSC Adv.* **2017**, *7*, 27100.

[254] A. Gankin, R. Sfez, E. Mervinetsky, J. Buchwald, A. Dianat, L. Medrano Sandonas, R. Gutierrez, G. Cuniberti, S. Yitzchaik, *ACS Appl. Mater. Interfaces* **2017**, *9*, 44873.

[255] A. K. Chauhan, D. K. Aswal, S. P. Koiry, S. K. Gupta, J. V. Yakhmi, C. Sürgers, D. Guerin, S. Lenfant, D. Vuillaume, *Appl. Phys. A Mater. Sci. Process.* **2008**, *90*, 581.

[256] N. E. Cant, K. Critchley, H. Zhang, S. D. Evans, *Thin Solid Films* **2003**, *426*, 31.

[257] R. C. Thomas, P. Tangyunyong, J. E. Houston, T. A. Michalske, R. M. Crooks, *J. Phys. Chem.* **1994**, *98*, 4493.

[258] S. Sowlati-Hashjin, C. F. Matta, *J. Chem. Phys.* **2013**, *139*, DOI 10.1063/1.4820487.

[259] C. Van Dyck, T. J. Marks, M. A. Ratner, *ACS Nano* **2017**, 5970.

[260] M. Hada, M. Ehara, K. Toyota, R. Fukuda, J. Hasegawa, M. Ishida, T. Nakajima, Y.

Honda, O. Kitao, H. Nakai, T. Vreven, J. A. Montgomery Jr., J. E. Peralta, F. Ogliaro, M. Bearpark, J. J. Heyd, E. Brothers, K. N. Kudin, V. N. Staroverov, T. Keith, R. Kobayashi, J. Normand, K. Raghavachari, A. Rendell, J. C. Burant, S. S. Iyengar, J. Tomasi, M. Cossi, N. Rega, J. M. Millam, M. Klene, J. E. Knox, J. B. Cross, V. Bakken, C. Adamo, J. Jaramillo, R. Gomperts, R. E. Stratmann, O. Yazyev, A. J. Austin, R. Cammi, C. Pomelli, J. W. Ochterski, R. L. Martin, K. Morokuma, V. G. Zakrzewski, G. A. Voth, P. Salvador, J. J. Dannenberg, S. Dapprich, A. D. Daniels, O. Farkas, J. B. Foresman, J. V. Ortiz, J. Cioslowski, D. J. Fox, **2013**.

[261] A. Szwajca, J. Wei, M. I. Schukfeh, M. Tornow, *Surf. Sci.* **2015**, *633*, 53.

[262] S. Gražulis, A. Daškevič, A. Merkys, D. Chateigner, L. Lutterotti, M. Quirós, N. R. Serebryanaya, P. Moeck, R. T. Downs, A. Le Bail, *Nucleic Acids Res.* **2012**, *40*, D420.

[263] S. Gražulis, A. Merkys, A. Vaitkus, M. Okulič-Kazarinas, *J. Appl. Crystallogr.* **2015**, *48*, 85.

[264] A. Merkys, A. Vaitkus, J. Butkus, M. Okulič-Kazarinas, V. Kairys, S. Gražulis, *J. Appl. Crystallogr.* **2016**, *49*, DOI 10.1107/S1600576715022396.

[265] R. T. Downs, M. Hall-Wallace, *Am. Mineral.* **2003**, *88*, 247.

[266] S. Gražulis, D. Chateigner, R. T. Downs, A. F. T. Yokochi, M. Quirós, L. Lutterotti, E. Manakova, J. Butkus, P. Moeck, A. Le Bail, *J. Appl. Crystallogr.* **2009**, *42*, 726.

[267] V. I. Pakhomov, A. V. Goryunov, P. V. Pakhomov, N. T. Chibiskova, *Zhurnal Neorg. Khimii* **1993**, *38*, 44.

[268] G.-M. Kim, Y. J. Oh, K. J. Chang, *J. Appl. Phys.* **2017**, *223705*, DOI 10.1063/1.4844415.

[269] *CPMD, Copyright IBM Corp 1990-2015, Copyright MPI Für Festkörperforschung Stuttgart 1997 - 2001*

[270] W. Humphrey, A. Dalke, K. Schulten, *J. Mol. Graph.* **1996**, *14*, 33.

[271] J. Stone, J. Gullingsrud, P. Grayson, K. Schulten, in *2001 ACM Symp. Interact. 3D Graph.* (Eds.: J.F. Hughes, C.H. Séquin), ACM SIGGRAPH, New York, **2001**, pp. 191–194.

[272] J. Eargle, D. Wright, Z. Luthey-Schulten, *Bioinformatics* **2006**, *22*, 504.

[273] J. Stone, An Efficient Library for Parallel Ray Tracing and Animation, Computer Science Department, University of Missouri-Rolla, **1998**.

[274] D. Frishman, P. Argos, *Proteins Struct. Funct. Genet.* **1995**, *23*, 566.

[275] A. Varshney, F. P. Brooks, W. V Wright, *IEEE Comput. Graph. Appl.* **1994**, *14*, 19.

[276] M. Sanner, A. Olsen, J.-C. Spehner, in *Proc. 11th ACM Symp. Comput. Geom.*, ACM, New York, **1995**, pp. C6–C7.

[277] R. Sharma, M. Zeller, V. I. Pavlovic, T. S. Huang, Z. Lo, S. Chu, Y. Zhao, J. C. Phillips, K. Schulten, **2000**, *20*, 29.

[278] S. Lin, K. Yang, L. Chen, *J. Phys. Chem. C* **2015**, *119*, 3050.

[279] S. R. Wasserman, G. M. Whitesides, I. M. Tidswell, B. M. Ocko, P. S. Pershan, J. D. Axel, *J . Am. Chem. SOC* **1989**, *111*, 5852.

[280] R. Chintala, P. Eyben, S. Armini, A. M. Caro, J. Loyo, Y. Sun, W. Vandervorst, *Eur. Polym. J.* **2013**, *49*, 1952.

[281] J. G. Speight, in *Environ. Org. Chem. Eng.*, Elsevier, **2017**, pp. 203–261.

[282] K. Seo, E. Borguet, *J. Phys. Chem. C* **2007**, *111*, 6335.

[283] Z. M. Fresco, J. M. J. Fréchet, *J. Am. Chem. Soc.* **2005**, *127*, 8302.

[284] U. Srinivasan, M. R. Houston, R. T. Howe, R. Maboudian, *J. Microelectromechanical Syst.* **1998**, *7*, 252.

[285] Z. Yoshimitsu, A. Nakajima, T. Watanabe, *Langmuir* **2002**, 5818.

[286] C. Lavieja, L. Oriol, J.-I. Peña, *Materials (Basel).* **2018**, DOI 10.3390/ma11122547.

[287] J. M. Vazquez-Martinez, J. S. Gomez, P. F. M. Ares, S. R. Fernandez-Vidal, M. B. Ponce, *Coatings* **2018**, *8*, 145.

[288] K. Tsougeni, A. Tserepi, G. Boulousis, V. Constantoudis, E. Gogolides, *Plasma Process. Polym.* **2007**, *4*, 398.

[289] N. Bowden, S. Brittain, A. G. Evans, J. W. Hutchinson, G. M. Whitesides, *Nature*

1998, *393*, 146.

[290] M. Xie, G. Lin, D. Ge, L. Yang, L. Zhang, J. Yin, X. Jiang, *ACS Mater. Lett.* **2019**, *1*, 77.

[291] E. Daramola, Fabrication of Micro/Nano-Structured Wrinkles Through Surface Modifcation of Poly(dimethylsiloxane), Florida State University, **2015**.

[292] D.-Y. Khang, J. A. Rogers, H. H. Lee, *Adv. Funct. Mater.* **2009**, *19*, 1526.

[293] C. Semprebon, P. Forsberg, C. Priest, M. Brinkmann, *Soft Matter* **2014**, *10*, 5739.

[294] J. Y. Chung, J. P. Youngblood, C. M. Stafford, *Soft Matter* **2007**, *3*, 1163.

[295] K. H. Kang, *Langmuir* **2002**, *18*, 10318.

[296] F. Mugele, J.-C. Baret, *J. Phys. Condens. Matter* **2005**, *17*, 705.

[297] B. F. Porter, N. Mkhize, H. Bhaskaran, *Microsystems Nanoeng.* **2017**, *3*, 17054.

[298] D. Nicolas-Debarnot, F. Poncin-Epaillard, *Anal. Chim. Acta* **2003**, *475*, 1.

[299] R. M. Morais, M. D. S. Klem, G. L. Nogueira, T. C. Gomes, N. Alves, *IEEE Sens. J.* **2018**, *18*, 2647.

[300] K. Crowley, A. Morrin, A. Hernandez, E. O. Malley, P. G. Whitten, G. G. Wallace, M. R. Smyth, A. J. Killard, *Talanta* **2008**, *77*, 710.

[301] D. K. Bandgar, S. T. Navale, S. R. Nalage, R. S. Mane, F. J. Stadler, D. K. Aswal, S. K. Gupta, V. B. Patil, *J. Mater. Chem. C* **2015**, *3*, 9461.

[302] P. P. Sengupta, S. Barik, B. Adhikari, *Mater. Manuf. Process.* **2006**, *21*, 263.

[303] K. Murugappan, M. R. Castell, *Electrochem. commun.* **2018**, *87*, 40.

[304] S. Manigandan, S. Majumder, S. Ganguly, K. Kargupta, *Mater. Lett.* **2008**, *62*, 2758.

[305] H. Bai, G. Shi, *Sensors* **2007**, *7*, 267.

[306] Z. Zhan, G. Zheng, W. Tao, Y. Cai, D. Sun, D. Wu, *J. Nanoeng. Nanosyst.* **2012**, *226*, 9.

[307] M. Van Damme, L. Clarisse, S. Whitburn, J. Hadji-Lazaro, D. Hurtmans, C. Clerbaux,

P. Coheur, *Nature* **2018**, *564*, 99.

[308] T. Berner, V. Cogliano, J. Fritz, M. Gehlhaus, S. Jones, J. Stanek, J. Strong, *Toxicological Review of Ammonia Noncancer Inhalation [CASRN 7664-41-7]*, Washington D.C., **2016**.

[309] "Ammonia," can be found under https://www.cdc.gov/niosh/pel88/7664-41.html, **2011**.

[310] National Research Council (U.S.). Subcommittee on Acute Exposure Guideline Levels., National Research Council (U.S.). Committee on Toxicology., National Research Council (U.S.). Board on Environmental Studies and Toxicology., *Acute Exposure Guideline Levels for Selected Airborne Chemicals. Volume 6*, National Academies Press, **2008**.

[311] B. Timmer, W. Olthuis, A. Van Den Berg, *Sensors Actuators, B Chem.* **2005**, *107*, 666.

[312] K. Crowley, M. R. Smyth, A. J. Killard, A. Morrin, *Chem. Pap.* **2013**, *67*, 771.

[313] I. Fratoddi, I. Venditti, C. Cametti, M. V. Russo, *Sensors Actuators, B Chem.* **2015**, DOI 10.1016/j.snb.2015.05.107.

[314] M. Bouvet, M. Mateos, R. Meunier-Prest, J.-M. Suisse, *Proceedings* **2017**, *1*, 3.

[315] B. Z. Lubentsov, O. N. Timofeeva, M. L. Khidekel', *Synth. Met.* **1991**, *45*, 235.

[316] M. Eising, C. E. Cava, R. V. Salvatierra, A. J. G. Zarbin, L. S. Roman, *Sensors Actuators, B Chem.* **2017**, *245*, 25.

[317] Y. Zhang, J. J. Kim, D. Chen, H. L. Tuller, G. C. Rutledge, *Adv. Funct. Mater.* **2014**, *24*, 4005.

[318] H. Kebiche, D. Debarnot, A. Merzouki, F. Poncin-Epaillard, N. Haddaoui, *Anal. Chim. Acta* **2012**, *737*, 64.

[319] Z. A. Boeva, V. G. Sergeyev, *Polym. Sci. Ser. C* **2014**, *56*, 145.

[320] S. Mikhaylov, N. A. Ogurtsov, N. Redon, P. Coddeville, J.-L. Wojkiewicz, A. A. Pudd, *RSC Adv.* **2016**, *6*, 82625.

[321] K. H. Lee, B. J. Park, D. H. Song, I. J. Chin, H. J. Choi, *Polymer (Guildf).* **2009**, *50*,

4372.

[322] Y. Xia, J. M. Wiesinger, A. G. MacDiarmid, A. J. Epstein, *Chem. Mater.* **1995**, *7*, 443.

[323] W. łużny, E. J. Samuelsen, D. Djurado, Y. F. Nicolau, *Synth. Met.* **1997**, *90*, 19.

[324] W. ŁUzny, E. Bańka, *Macromolecules* **2000**, *33*, 425.

[325] S. Bhadra, D. Khastgir, N. K. Singha, J. Hee, **2009**, *34*, 783.

[326] M. H. U. Bhuiyan, R. Saidur, M. A. Amalina, R. M. Mostafizur, A. Islam, *Procedia Eng.* **2015**, *105*, 431.

[327] C. Mkhize, J. Britton, T. Nyokong, *Polyhedron* **2014**, *81*, 607.

[328] Q. Hao, V. Kulikov, V. M. Mirsky, *Sensors Actuators B. Chem.* **2003**, *94*, 352.

[329] J. Huang, S. Virji, B. H. Weiller, R. B. Kaner, *J. Am. Chem. Soc.* **2003**, *125*, 314.

[330] N. J. Pinto, I. Ramos, R. Rojas, P. Wang, A. T. Johnson, *Sensors Actuators B. Chem.* **2008**, *129*, 621.

[331] R. S. Andre, D. Kwak, Q. Dong, W. Zhong, D. S. Correa, L. H. C. Mattoso, Y. Lei, *Sensors* **2018**, *18*, 1.

[332] Y. Jiang, N. Tang, C. Zhou, Z. Han, H. Qu, X. Duan, *Nanoscale* **2018**, *10*, 20578.

[333] S. Virji, J. Huang, R. B. Kaner, B. H. Weiller, *Nano Lett.* **2004**, *4*, 491.

[334] M. Sajfutdinow, K. Uhlig, A. Prager, C. Schneider, B. Abel, D. M. Smith, *Nanoscale* **2017**, DOI 10.1039/C7NR03696E.

[335] J. Lin, A. Mohammadizia, A. Neogi, H. Morkoc, M. Ohtsu, *Appl. Phys. Lett.* **2010**, *97*, DOI 10.1063/1.3515419.

[336] C. Y. Cho, Y. Zhang, E. Cicek, B. Rahnema, Y. Bai, R. McClintock, M. Razeghi, *Appl. Phys. Lett.* **2013**, *102*, DOI 10.1063/1.4809521.

[337] M. Altissimo, *Biomicrofluidics* **2010**, *4*, 2.

Published work

Work presented in this thesis

1. Benjamin Francis Porter, **Nhlakanipho Mkhize** and Harish Bhaskaran, “Nanoparticle assembly enabled by EHD-printed monolayers”, Nature Microsystems and Nanoengineering 3, 17054 (2017), DOI: 10.1038/micronano.2017.54

2. **Nhlakanipho Mkhize**, Kevin A. Lobb, Harish Bhaskaran, “Electric field induced modification of self-assembled monolayers”, (in preparation)

3. **Nhlakanipho Mkhize**, Krishnan Murugappan, Martin Castell, Harish Bhaskaran, “Printed chemiresistive sensor with increased performance”, (submitted)

4. **Nhlakanipho Mkhize**, Utku Ali, Harish Bhaskaran, “Surface wetting control with anisotropic wrinkles for high resolution printing”, (in preparation)

Contributions to work not related to this thesis

5. Ren-jie Chang, Yuewen Sheng, Gyeong Hee Ryu, **Nhlakanipho Mkhize**, Tongxin Chen, Yang Lu, Jun Chen, Ja Kyung Lee, Harish Bhaskaran, Jamie Warner ‘Post growth Substitutional Tin Doping of 2D WS2 Crystals Using Chemical Vapor Deposition’ ACS Appl Mater. Interfaces, 2019 DOI: 10.1021/acsami.9b06588

6. Ren-Jie Chang, Yuewen Sheng, Tongxin Chen, **Nhlakanipho Mkhize**, Yang Lu, Harish Bhaskaran, Jamie Warner, ‘Morphology Control of Two-Dimensional Tin Disulfide on Transition Metal Dichalcogenides Using Chemical Vapor Deposition’ ACS Appl Nano Mater, 2019. DOI:10.1021/acsanm.9b00676

Conference attendance

1. **Nhlakanipho Mkhize**, Krishnan Murugappan, Martin Castell, Harish Bhaskaran Electrohydrodynamic jet printed polyaniline for highly sensitive chemiresistors (Poster) 5th Innovations in Large-Area Electronics Conference, 22 – 23 January 2019, Cambridge, www-large-area-electronics.eng.cam.ac.uk/innoLAE2019

2. **Nhlakanipho Mkhize**, Harish Bhaskaran.

Investigation into physical properties of polyaniline ink to enhance printability with Electrohydrodynamic Jet Printing (Poster), 29th MME Europe Workshop, Smolenice, Slovakia, 26 – 29 August 2018, www.mme2018.org/

3. **Nhlakanipho Mkhize**, Harish Bhaskaran
   Electric field induced breakdown: Monolayer behaviour under duress (Poster), MRS Spring Meeting 2018, Phoenix Convention Centre, Phoenix, Arizona, United States, 2 – 6 April 2018, www.mrs.org/spring2018

4. **Nhlakanipho Mkhize**, Harish Bhaskaran:
   Optical activity of gold nanoparticle metamaterials prepared using additive manufacturing MME 2017, 28th Micromechanics and Microsystems Europe Workshop, August 23-25 2017, Uppsala, Sweden, www.mme2017.org/

5. **Nhlakanipho Mkhize**, Harish Bhaskaran:
   Enhanced printing resolution on flexible substrates via self-assembled monolayer surface modification, MNE2017 Conference, Braga, Portugal, 18-22 September 2017, www.mne2017.org/

6. **Nhlakanipho C. Mkhize**, Benjamin F. Porter, Madhav Kumar, Ritesh Agarwal and Harish Bhaskaran, "Micro-contact printing in phase change material nanowire device fabrication" (Poster), 13th International Workshop on Nanomechanical Sensing, Delft, The Netherlands, 22 – 24 June, 2016, www.nmc-2016.org/

Appendix 1

In line with the list of equipment found in Chapter 3, Table A1.1 lists all the chemicals used in this work, along with their abbreviations (where necessary) and supplier names.

Table A1.1 summarises the list of chemicals and substrates used for the printing experiments, along with their suppliers. This information will not be repeated in subsequent chapters.

Chemical	Abbreviation	Supplier
1H, 1H, 2H, 2H-Perfluorooctyltriethoxysilane	POTS	Sigma
		Alfa Aesar
(3-Aminopropyl)triethoxysilane 99%	APTES	Sigma
Trimethoxyoctadecylsilane	TMODS	Sigma
1H,1H,2H,2H-Perfluorodecanethiol	PFDET	Sigma
Acetone	-	Sigma
2-Propanol	IPA	Sigma
Ethanol	EtOH	Sigma
Hexane	-	Sigma
1-Methyl-2-pyrrolidone	NMP	Sigma
Polydimethylsiloxane	PDMS	Dow Corning
Hydrochloric acid 37%	HCl	Sigma
(1R)-(−)-10-Camphorsulfonic acid	CSA	Sigma
polyaniline	PANI	Sigma
Poly(3,4-ethylenedioxythiophene)-poly(styrenesulfonate)	PEDOT:PSS	Sigma
Glycerol	-	Sigma
Ethylene glycol	EG	Sigma
Triethylene glycol monomethyl ether	TGME	Sigma

20 nm gold nanoparticle suspension in citrate buffer	AuNP	Sigma
Tetradecane	-	Sigma
Toluene	-	Sigma
Sulphuric acid	H_2SO_4	Sigma
Hydrogen Peroxide	H_2O_2	Sigma
Deionized Water	DI water	Chemiphase
Ammonia	NH_3	BOC gas
Substrates		
Silicon wafer with thermal oxide (various oxide thicknesses)	SiO_2/Si	Inseto
Interdigitated electrodes patterned onto flexible and glass substrates	IDE	DropSens
Indium tin oxide coated polyethylene terephthalate	ITO/PET	Sigma

Appendix 2

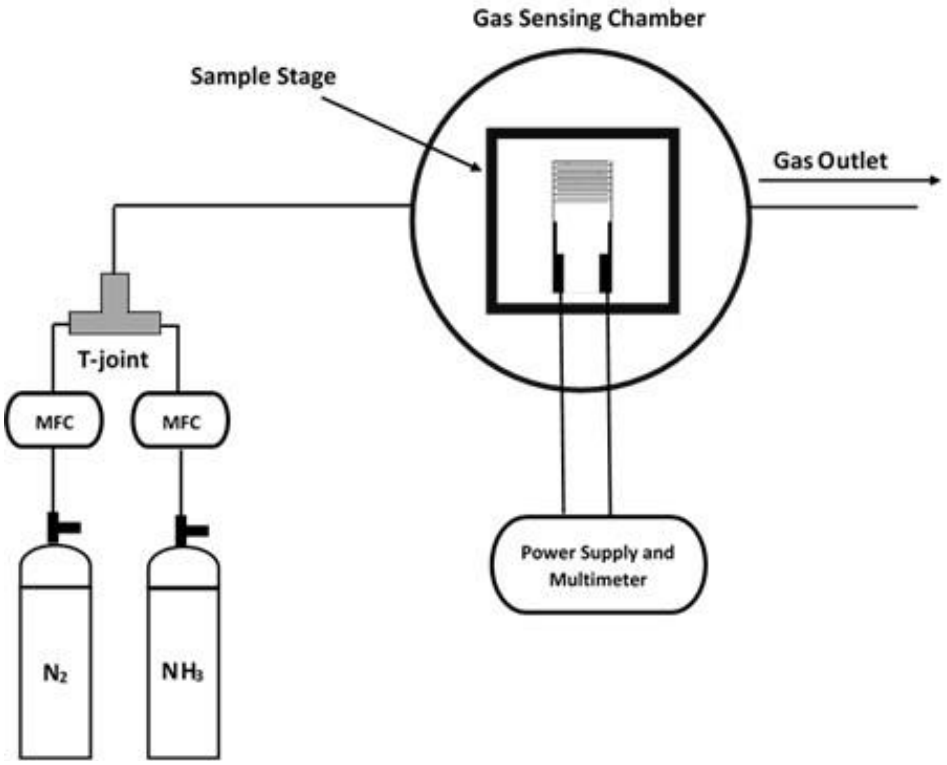

Figure A2.1. Schematic of gas sensing chamber used in Chapter 6 sensing experiments. This setup was designed by Dr Krishnan Murugappan.

Gas Sensing Experiments

A custom made gas sensing chamber (Allectra, UK) was used for the sensing experiments. The gas mixing setup was achieved with an aid of a perfluoroalkoxy tubings (PFA 0.25 inch outer diameter and 0.062 inch inner diameter). Figure A2.1 shows a schematic of the gas mixing setup used. The ammonia gas cylinder is connected to a regulator which is then connected to a digital mass flow controller (MFC, Alicat, USA) to control the flow of the gas into one side of a Swagelok T-joint and the other side is connected to another digital flowmeter that controls the flow of a nitrogen gas cylinder. The T-joint allows mixing of the two gases before it enters the inlet of the gas sensing chamber. After placing the interdigitated electrodes (IDEs) on the sample stage in the sensing chamber they are electrically connected to a power supply/multimeter. The sensing chamber is first purged with nitrogen gas for 45 minutes to remove any impurities present in the chamber or in the sensing layer on the IDEs. Then a

voltage of 1V is applied to the two electrodes and the current is monitored as a function of time on a computer equipped with BenchVue software. Once a stable baseline is reached different concentrations of ammonia gas is allowed into the system. The ppb concentration of ammonia gas that was introduced into the sensing chamber was calculated by the relative flowrates of the two mass flow controllers. The exposure time for each concentration was fixed for 5 minutes for all sensors.